

Adsorption calorimetry on two-dimensional model catalysts

vorgelegt von

Dipl.-Chem.

Petr Dementyev

geb. in Petropawlowka, Republik Burjatien

von der Fakultät II - Mathematik und Naturwissenschaften

der Technischen Universität Berlin

zur Erlangung des akademischen Grades

Doktor der Naturwissenschaften

- Dr. rer. nat. -

genehmigte Dissertation

Promotionsausschuss:

Vorsitzender: Prof. Dr. rer. nat. Arne Thomas

Gutachter: Prof. Dr. rer. nat. Hans-Joachim Freund

Gutachter: Prof. Dr. rer. nat. Reinhard Schomäcker

Tag der wissenschaftlichen Aussprache: 30. Juni 2016

Berlin 2016

Abstract

The strength of interactions between molecules and surfaces represents an important physicochemical characteristic determining many natural phenomena and technological processes, in particular performance of the heterogeneously catalyzed synthesis. Recent instrumental advances have made it possible to directly measure the adsorption energy of gaseous molecules on various substrates, including planar model catalysts. Adsorption calorimetry is particularly convenient for studying electronic and geometric effects of the surface reactivity. It also allows the establishment of reliable benchmarks for enthalpies of formation of adsorbed species which are highly demanded in theoretical computational approaches but hardly available at present. In this study, we address two largely independent problems: (i) interaction of chiral molecules with chirally-modified metal surfaces and (ii) reactivity of different surfaces of a metal oxide in respect to water.

Modification of metal catalysts by adsorption of chiral compounds is one of the most promising ways to implement enantioselective heterogeneous catalysis. Interaction of propylene oxide (PO) with Pt(111) pre-covered by 1-(1-naphthyl)ethylamine (NEA) and 2-methylbutanoic acid (MBA) was studied in order to probe stereoselectivity in adsorption on chirally-modified surfaces. Detailed coverage dependences of adsorption energy for both R- and S-enantiomers of PO were obtained as a function of the modifiers surface coverage. From calorimetry measurements, adsorption behavior on the two types of chiral surfaces can be clearly distinguished, indicating different modification mechanisms. For all investigated substrates, enantiospecificity during adsorption was proved to be very small in terms of energetics, as well as surface capacity to accommodate chiral adsorbates.

Metal oxide catalysts are complex compounds which are active in a wide range of reactions. Studying surface chemistry of the iron oxide Fe_3O_4 , we aimed to reveal the influence of the oxide surface structure on its reactivity. Adsorption of water on thin films with two different surface terminations was investigated in a broad range of coverage and temperature conditions. As opposed to bare Pt, calorimetry measurements indicate a high affinity of magnetite towards an interaction with water. Adsorption energy was correlated to particular surface species which were identified with the help of vibrational spectroscopy and quantum chemistry. On $\text{Fe}_3\text{O}_4(111)$, water forms dimer-like complexes with the specific adsorption energy of $\sim 200 \text{ kJ mol}^{-1}$. The reaction occurs less readily as surface concentration of the species increases. Adsorption of water was quantitatively shown to be more energetically favorable on $\text{Fe}_3\text{O}_4(111)$ than on $\text{Fe}_3\text{O}_4(100)$.

Zusammenfassung

Die Stärke der Wechselwirkungen zwischen Flüssigkeitsmolekülen und Festkörperoberflächen ist eine wichtige physikalisch-chemische Eigenschaft, die viele Naturphänomene und technologische Verfahren, wie zum Beispiel heterogen-katalytische Reaktionen, bestimmt. Die jüngsten Weiterentwicklungen ermöglichen es, die Adsorptionenergie von Molekülen auf verschiedenen Substraten direkt zu messen. Die Adsorptionskalorimetrie auf ebenen Modellkatalysatoren eignet sich besonders, um elektronische und geometrische Effekte der Oberflächenreaktivität zu untersuchen und die Korrelation von Struktur und chemischer Aktivität zu bestimmen. In der vorliegenden Arbeit befassen wir uns mit zwei unabhängigen Problemen: (i) die Wechselwirkung von chiralen Molekülen mit chiral-modifizierten Metalloberflächen und (ii) die Reaktivität von verschiedenen Oberflächenterminierungen eines Metalloxids in Bezug auf Wasser.

Die Modifizierung von Metallkatalysatoren durch Adsorption von chiralen Verbindungen ist einer der vielversprechendsten Wege, enantioselektive heterogene Katalyse umzusetzen. Um die Stereoselektivität bei der Adsorption an chiral-modifizierten Oberflächen zu charakterisieren, wurde die Wechselwirkung von Propylenoxid mit 1-(1-Naphthyl)ethylamin und 2-Methylbutansäure auf Pt(111) untersucht. Die ermittelten detaillierten Bedeckungsabhängigkeiten der Adsorptionsenergie für beide Propylenoxid-Enantiomere zeigen, dass sich das Adsorptionsverhalten von Propylenoxid für beide Arten von chiralen Oberflächen unterscheidet. Bei allen untersuchten Substraten wurde eine sehr geringe Enantioselektivität bei der Adsorption im Hinblick auf die Energetik und die Menge adsorbierter Moleküle nachgewiesen.

Metalloxidkatalysatoren sind komplexe Verbindungen, die in einer Vielzahl von Reaktionen aktiv sind. Durch die Untersuchung der Oberflächenchemie vom Eisenoxid Fe_3O_4 sollte der Einfluss der Oxid-Oberflächenstruktur auf die Reaktivität aufgezeigt werden. Dafür wurde in einem breiten Bereich von Bedeckungen und Temperaturen die Adsorption von Wasser auf dünnen Eisenoxidfilmen mit zwei unterschiedlichen Oberflächenterminierungen untersucht. Die kalorimetrischen Daten zeigen, dass Magnetit eine hohe Affinität zu Wasser hat, wobei die Oberflächenspezies mit Hilfe von Infrarotspektroskopie und Quantenchemie identifiziert wurden. Dimer-ähnliche Komplexe mit einer spezifischen Adsorptionsenergie von $\sim 200 \text{ kJ mol}^{-1}$ werden auf $\text{Fe}_3\text{O}_4(111)$ gebildet. Mit zunehmender Bedeckung tritt die Reaktion weniger bereitwillig auf. Es wurde gezeigt, dass die Adsorption von Wasser auf $\text{Fe}_3\text{O}_4(111)$ energetisch günstiger als auf $\text{Fe}_3\text{O}_4(100)$ ist.

Contents

§ 1 Introduction.....	1
1.1 Thermodynamics in surface chemistry	1
1.2 Two-dimensional model catalysts	3
1.3 Adsorption calorimetry on planar substrates	4
1.4 Motivation and outline of the work	7
§ 2 Methodology.....	11
2.1 Chiral metal surfaces	11
2.1.1 Stereoselective heterogeneous catalysis	11
2.1.2 Chirality at surfaces.....	12
2.1.3 Chiral modifier 1-(1-naphthyl)ethylamine (NEA)	14
2.1.4 Chiral modifier 2-methylbutanoic acid (MBA)	17
2.2 Metal oxide surfaces.....	19
2.2.1 Surface chemistry of metal oxides	19
2.2.2 Thin Fe ₃ O ₄ (111) film.....	21
2.2.3 Thin Fe ₃ O ₄ (100) film.....	25
2.2.4 Water on iron oxides	27
2.3 Single-crystal adsorption calorimetry	30
2.3.1 Principles	30
2.3.2 Enthalpimetric analysis	33
2.3.3 SCAC experimental setup.....	37
2.4 Infrared reflection-absorption spectroscopy	46
2.4.1 Principles	46
2.4.2 IRAS experimental setup	47

§ 3 Research synopsis.....	49
3.1 Adsorption calorimetry on chiral metal surfaces	49
3.2 Adsorption calorimetry on metal oxide surfaces.....	53
§ 4 Chirally-modified metal surfaces: energetics of interaction with chiral molecules	59
4.1 Abstract.....	59
4.2 Introduction.....	59
4.3 Experimental section.....	63
4.4 Results	64
4.4.1 PO adsorption on R-NEA-modified Pt(111)	64
4.4.2 PO adsorption on S-MBA-modified Pt(111)	68
4.5 Discussion	73
4.6 Conclusions	77
§ 5 Water interaction with iron oxides.....	79
5.1 Abstract.....	79
5.2 Introduction.....	79
5.3 Results and discussion	81
5.4 Conclusions	89
§ 6 Surface chemistry of water on magnetite: a mechanistic study	90
6.1 Abstract.....	90
6.2 Introduction.....	90
6.3 Results and Discussion.....	93
6.3.1 Energy Measurement at 120 K	93
6.3.2 Energy Measurement at 180-300 K	96

6.3.3 Infrared Spectroscopy at 300 and 240 K.....	98
6.3.4 Infrared Spectroscopy at 180 and 120 K.....	104
6.3.5 Correlation between adsorption energy and spectroscopic information on surface species.....	109
6.4 Conclusions	111
6.5 Experimental section.....	113
6.6 Supporting information	114
6.6.1 Sticking coefficients	114
6.6.2 Infrared spectra	118
§ 7 Adsorption energy of water on Fe ₃ O ₄ (100) by microcalorimetry	119
7.1 Abstract.....	119
7.2 Introduction.....	119
7.3 Experimental details	121
7.4 Results and Discussion.....	121
7.5 Conclusions	127
§ 8 Final conclusions and outlook.....	129
Appendix	131
List of publications	133
Conference presentations	134
Acknowledgments.....	135
Abbreviations	136
References	137

§ 1 Introduction

1.1 Thermodynamics in surface chemistry

In the last decade, primary energy consumption in the European Union decreased by 12 %, whereas the share of fossil sources in final consumption still exceeds 70 %.^[1] Industry and transportation would require more innovations in order to improve the efficient energy use. In this respect, catalysis serves for the energy efficiency in production of a majority of valuable large-volume chemicals, e.g., ammonia and sulfuric acid. Catalysts lower the activation barriers of chemical reactions, thereby enabling desirable processes to be carried out at lower temperatures, i.e. consuming less energy.^[2] Catalytic processes are nowadays embedded in many applications from pharmaceutical synthesis to automobile exhaust systems. More importantly, catalysis is a significant component of almost all perspective renewable energy technologies such as solar fuels, biomass conversion, energy storage, and fuel cells.^[3]

Even though catalysts are not consumed in the catalyzed reactions, they do participate in the chemical transformation. A heterogeneous catalyst, for instance, accommodates reactant molecules on its surface changing their molecular geometry, electronic structure, or even transforming them into new intermediate species, typically smaller dissociated fragments. The catalyst surface also plays a role of a medium, where different reagents meet each other. Depending on conditions, product molecules can, in turn, stay on the surface, inhibiting further reaction progress. A good catalyst must therefore interact with reagent molecules in the most appropriate way, so that they are bonded to the surface neither too strongly, nor too weakly. This rule, known as the Sabatier principle,^[2] was formulated a hundred years ago and reflects the crucial importance of thermodynamics in catalysis, despite the latter is a kinetic effect. Indeed, catalysts do not change chemical equilibria, but there are certain connections between catalytic activity and thermodynamics of elementary surface reactions recognized in such fundamental concepts as Brønsted-Evans-Polanyi relationships and volcano plots.^[4] Hence, not only enthalpies of overall reactions and their activation

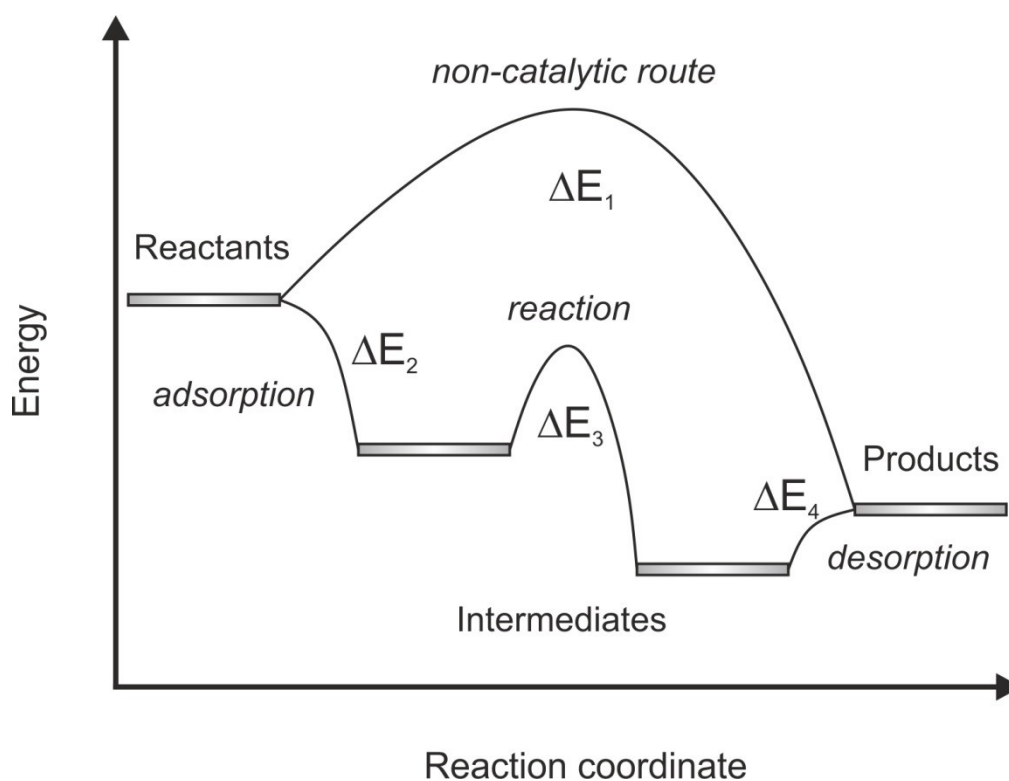


Figure 1.1 A schematic energy profile of a heterogeneously catalyzed reaction. ΔE_1 and ΔE_3 are activation barriers; ΔE_2 and ΔE_4 are adsorption energies for reactant and product species, respectively.

barriers determine performance of a catalytic cycle, but also enthalpies of formation of each intermediate and the ratios between them matter for reaction kinetics (Fig. 1.1). Consequently, knowledge on thermodynamic parameters is of great importance for the catalytic production and for surface chemistry in general.

Among chemical interactions with and on solid surfaces, adsorption is a primary process, by which molecules from a gas or liquid phase are transferred to a surface. Provided a certain compound, at given conditions, adsorbs on a catalyst surface, there is a release of heat according to the second law of thermodynamics. Due to the loss of a translational degree of freedom, the negative change in entropy has to be compensated by a decrease in the adsorption enthalpy. Adsorption calorimetry is a method to detect such energy changes, and it allows for obtaining quantitative information on the strength of the adsorbate-surface bonding. Since Pierre-Antoine Favre conducted the first thermochemical experiment on gas-solid

interactions in 1854, adsorption calorimetry on powder and porous materials has been substantially developed.^[5] Presently, it is used for characterization of catalyst surfaces by establishing acidic-basic nature of the active sites, assessing their concentration, and obtaining average adsorption energies for different types of sites.^[6] The capability of the instrumentation used to determine true thermodynamic parameters is very limited because of the vast complexity of heterogeneous catalysts, which often possess diverse chemical composition, multiple phase constituents, such as nanoparticles dispersed on a support, and a very large surface area exhibiting all possible geometric faces simultaneously.

1.2 Two-dimensional model catalysts

The most promising strategy to obtain microscopic understanding of heterogeneous reactions consists in reduction of the structural and chemical complexity of real catalysts by studying more simplistic systems.^[7, 8] Specifically, the use of single-crystal substrates as catalyst models offers several advantages over conventional catalysis research. The planar samples become accessible to the surface sensitive characterization techniques which allow for detailed investigation of the surface composition and morphology. Adsorption experiments on such well-defined substrates under ultrahigh vacuum (UHV) conditions enable to identify the surface species formed, the nature of the active sites, and eventually the reaction mechanism. One can also prepare different substrates to vary the structural parameters and address their influence on the surface reactivity.

The surface science approach has helped to gain insight into elementary steps of many important catalytic reactions such as, e.g., the Haber–Bosch process.^[9] In order to bridge the so-called materials gap, the model catalysts have evolved from pristine metal surfaces to more complex supported nanoparticles.^[10-12] Particularly, significant progress was made by the development of the thin film methodology for preparing well-defined metal oxide surfaces.^[13] Diversity of the proposed metal oxide substrates allow to successfully mimic supported metals catalysts and to study support, electronic, geometric, and other effects in the catalytic activity.^[14] With the

model catalysts developed, adsorption of molecules can be studied at the atomistic level. Most importantly, kinetic and thermodynamic characteristics of the surface reactions can be potentially determined.^[15]

1.3 Adsorption calorimetry on planar substrates

Single-crystal samples have too low of a surface-to-volume ratio to enable adsorption energy to be measured by conventional temperature sensors. Direct calorimetric studies on well-defined planar substrates have therefore been a long-standing challenge. Nevertheless, the energetics of adsorbate-surface interactions has been probed by a few indirect techniques, relying on the assumption of the absolute adsorption reversibility. Temperature programmed desorption (TPD) is probably the simplest and most widespread approach which in some cases gives fairly reliable estimates of adsorption energies. A TPD experiment consists in adsorption of a known amount of a gas on a sample, kept at relatively low temperature, followed by a controllable heating of the sample up to the temperature when all adsorbates are supposed to be removed. A relative number of desorbing molecules is monitored in the gas phase by a mass-spectrometer, as a function of the substrate temperature. The TPD spectra allow extracting information on desorption kinetics, namely determination of the activation energy for desorption which is then correlated with the adsorption energy. TPD analysis is generally based on the Polanyi-Wigner equation relating the rate of desorption to the density of adsorption sites, relative coverage, and surface temperature.^[16] As system specific parameters, the activation energy and the pre-exponential frequency factor are included in the equation and can in principle both depend on surface coverage. There are several ways to determine their values out of the experimental TPD data, but they all rely on a certain degree of assumptions.

In equilibrium adsorption isotherms/isobars (EAI), adsorption energy is derived via the classical Clausius-Clapeyron relation, describing phase-transition equilibria.^[16] The method implies separation of the thermodynamic parameters for the adsorbates and the substrate, i.e. suits only for weakly interacting systems. Experimentally, surface coverage is measured as a

function of pressure at a constant temperature or vice versa, and then the data is plotted as a logarithm of pressure versus reciprocal temperature. The slope of these curves yields coverage-dependent adsorption energy. In practice, establishment of real adsorption-desorption equilibria is often a matter of speculation, and determination of absolute surface coverages under such sensitive conditions is rather challenging. Similar to TPD, the EAI approach neglects chemical transformations, which may take place prior to desorption, and does not consider possible changes in the surface structure caused by temperature variations during heating or cooling. Furthermore, irreversible reactive adsorption, diffusion of the adsorbates into the bulk, and many other phenomena cannot be studied by the desorption-based methods.

It took many years before the idea of adsorption calorimetry was fully implemented in surface science research.^[17] The first attempt to enlarge the surface area to weight ratio was made in the 1930s, when a microcalorimeter on fine wires was proposed.^[18] In this approach, metal wires could be repeatedly cleaned by flash heating and served simultaneously as an adsorbent and as a resistance thermometer.^[19] Almost concurrently, Otto Beeck introduced an adsorption calorimeter on supported polycrystalline films, where thin metal films were deposited in vacuum onto the inner side of a thin-walled glass vessel, whereas a long wire wound outside worked as a resistance temperature detector.^[20] The surface area of such films was typically around 100 cm², and temperature changes as low as 10⁻⁶ K could be measured.^[21, 22] These methods ensured much cleaner and better defined surfaces than powder samples and provided important insight into the energetics of gas-solid interactions. However, intrinsic heterogeneity of evaporated films and wires complicated the assignment of the measured heats.

Only in the early 1990s, David King at the University of Cambridge constructed an adsorption microcalorimeter that could operate on clean two-dimensional substrates, where the nature of adsorption sites and chemical formulae of the adsorbates are clearly determined.^[23, 24] The instrument was based on free-standing metal single crystals of ~200 nm in thickness and

employed infrared thermometry as a heat detector. Therefore, the heat capacity of the sample was greatly reduced, and the temperature rise upon adsorption became available for detection. King's group was able to measure adsorption energy as a detailed function of surface coverage by exposing the sample to the gas of interest in the form of short molecular beam pulses. To calibrate the pyrometer, the sample was irradiated by laser light of known intensity, and the instrument detection limit was proved to be as low as ~ 10 kJ mol⁻¹ of adsorbates.^[25]

The new technique, known now as Single-Crystal Adsorption Calorimetry (SCAC), was further developed by Charles Campbell in Seattle who invented a novel heat detection principle.^[26-28] In Campbell's device, a transient temperature rise occurring upon adsorption of a gas pulse is measured by a pyroelectric polymer ribbon which is brought into mechanical contact with the back side of an ultrathin sample. The pyroelectric detection scheme proposed by Campbell is much more sensitive in comparison to an optical pyrometry, so that the new approach offered multiple advantages over previous SCAC designs. Ability to use thicker single crystals (1 μ m or more) enabled variety of possible materials of interest to be greatly expanded and also simplified their preparation, since thicker substrates are easier accessible for high-temperature treatments. Moreover, low-temperature adsorption experiments became routinely feasible with the novel SCAC apparatus, so that by changing the conditions one can differentiate various processes taking place upon adsorption and measure separately their energetic effects, e.g., for molecular adsorption and dissociation.

In its current state, SCAC is a powerful surface science technique which has a great impact on the understanding of the energetics of surface reactions.^[29] There are already several SCAC instruments running around the world: recently upgraded King's calorimeter in Cambridge; two SCAC machines for separate studying of adsorption of atoms and molecular species in Campbell's group; the SCAC apparatus in Berlin used in the present study;^[30] the compact calorimeter at TU Darmstadt;^[31] the liquid phase SCAC adaptation for electrochemical reactions realized at KIT.^[32] A wide variety of adsorbing species combined with a number of different

substrates has been thoroughly studied to date.^[25, 33-36] Those include molecular, dissociative, and co-adsorption on late transition metals (Co, Ni, Pd, Pt, Rh), metals atom adsorption on oxide surfaces (MgO, CeO₂, Fe₃O₄), and several other systems.

1.4 Motivation and outline of the work

Metals usually possess enough mechanical stability which is necessarily required for preparation of ultrathin single crystals in SCAC experiments, and therefore pristine metallic surfaces represent the simplest model substrates for adsorption calorimetry. However, they do not reproduce many relevant structural properties of real catalytic materials which are, as a rule, finely dispersed oxides and/or supported metal nanoparticles. The single-crystal adsorption calorimeter constructed at the Fritz Haber Institute was specially designed for studies on well-defined hierarchical model catalysts, i.e. metal nanoparticles deposited on planar thin oxide films.^[30] Since its development, the microcalorimeter has been successfully applied to the investigation of such a fundamental problem as the particle size effect, when adsorption energy of simple prototypic gases (CO, O₂) was measured on supported Pd nanoparticles.^[37-39] The present thesis continues to utilize the novel SCAC instrument in the context of other important issues of heterogeneous catalysis, where more complex adsorbates have been investigated. The first problem addressed is interaction of chiral species with chirally-modified surfaces, and the second one concerns surface chemistry on metal oxides.

In the first part of the work, adsorption of PO on Pt(111) modified by NEA and MBA is studied in light of enantioselectivity, which is one of the most challenging issues for modern synthetic chemistry. Current demands of pharmaceutical and agrochemical industries in chirally pure chemicals are covered by natural chiral precursors, enzyme, and rarely homogeneous enantioselective catalysis. Implementation of heterogeneous catalysts into the enantioselective synthesis would have many advantages.^[40] The main widely recognized strategy for preferential production of one enantiomer over the other is a modification of usual metal catalysts by adsorption of chiral

organic molecules – chiral modifiers.^[41] There are two proposed mechanisms of the stabilizing interaction between a modifier and a reactant which are believed to be responsible for chirality induction. The first one is the docking interaction that is the formation of one-to-one complexes between modifier and reactant molecules. The second mechanism, known as the chiral templating, is through the formation of two-dimensional ensembles of modifier molecules which provide stereospecific adsorption sites for reagent molecules. Both models imply a difference in enthalpy of formation between competing pro-chiral configurations of the adsorbed reactant. Using chiral adsorbates as a probe, model TPD studies often reveal appreciable energy differences between two adsorbing enantiomers, and the number of adsorbates which can be accommodated on chiral surfaces may also substantially vary.^[42] However, enantioselectivity effects measured in TPD experiments suffer from the drawbacks discussed above, especially considering the fact that large organic molecules are heated on highly active precious metal surfaces.^[43, 44] The present study aims to conduct the first isothermal measurement of the adsorption energy of chiral molecules on chirally-modified surfaces with a direct calorimetric method and to study the impact of the nature of modifiers on stereoselectivity in adsorption.

Interaction of water with the iron oxide Fe_3O_4 is the second subject of the present study. Metal oxides are widely used as a support for metal catalysts and also as catalysts themselves.^[45] Thus, catalysts based on iron oxides are employed in the water-gas shift reaction which is used in hydrogen production and is consequently a highly relevant step in many processes such as steam reforming and the Fischer–Tropsch process.^[46] Since metal oxide surfaces can have several chemically different adsorption sites, their reactivity may substantially vary depending on a particular surface plane exposed. For example, there is still no consensus on the elementary steps underlying the water-gas shift reaction, particularly the nature of the active form of water is unknown.^[47] Although adsorption of water on planar Fe_3O_4 substrates has been studied before, it is not clear whether the model of dissociation into two surface hydroxyl groups is valid.^[48] Previous TPD studies suggest the adsorption energy of water on magnetite ($\sim 65 \text{ kJ mol}^{-1}$)

to be similar to that on inert substrates (50 kJ mol^{-1}).^[49] Spectroscopic information available for the most stable $\text{Fe}_3\text{O}_4(111)$ and $\text{Fe}_3\text{O}_4(100)$ surfaces is also poor and contradictory.^[50, 51] In this work, SCAC is used together with infrared spectroscopy (IRAS) to study interaction of water with well-defined epitaxial magnetite substrates of two different surface terminations. The aim is to obtain a detailed mechanistic understanding of the surface reaction on the metal oxide and to reveal structure-reactivity correlations caused by rearrangements of the surface atoms.

The given introductory part is followed by a review *Chapter 2*. It starts with the description of the two-dimensional model catalysts of interest. Particularly, the concept of chiral surfaces is introduced along with an overview on major types of solid enantioselective catalysts, and the two model systems studied are described afterwards. Preparation of the model iron oxides substrates is reviewed next with a special emphasis placed on their surface structures. Existing adsorption models of water on magnetite are presented as well. Experimental techniques employed in this study, including their principles, resulting information, and instrumental performance, are described in detail in the subsequent sections of *Chapter 2*.

Chapter 3 represents an extended summary of the results obtained in this study, and its content partly overlaps with the following chapters. The first section is devoted to the SCAC study of the adsorption of R- and S-PO on $\text{Pt}(111)$ modified by R-NEA and S-MBA. In the second part, SCAC and IRAS measurements of water adsorption on $\text{Fe}_3\text{O}_4(111)$ and $\text{Fe}_3\text{O}_4(100)$ are presented and briefly discussed.

Accordingly, the low-temperature SCAC experiments on adsorption of PO enantiomers on two chirally-modified $\text{Pt}(111)$ substrates are described in detail in *Chapter 4*. The model chiral modifiers are characterized in terms of selectivity towards adsorption of chiral adsorbates. Some considerations on the mechanisms of their interaction with the probe molecules are given as well. Detailed discussion on the surface chemistry of water on $\text{Fe}_3\text{O}_4(111)$ is given in *Chapters 5* and *6*. In this case, calorimetry measurements were done at various temperatures and were accompanied by infrared spectroscopy experiments. A new adsorption model was elaborated in result

of this combined study, supported by quantum chemical calculations, which were carried out by the group of Professor Joachim Sauer at the Humboldt University of Berlin. In *Chapter 7*, interaction of water with the $\text{Fe}_3\text{O}_4(111)$ and $\text{Fe}_3\text{O}_4(100)$ surfaces is compared on the basis of the SCAC data. The structure-reactivity relationship obtained is discussed in terms of electrophilic properties of the surface cation sites.

Chapter 8 draws final conclusions of the thesis and gives some outlooks for future SCAC applications. Additional remarks on the experiments performed during this doctoral study are made in the *Appendix*.

§ 2 Methodology

2.1 Chiral metal surfaces

2.1.1 Stereoselective heterogeneous catalysis

Asymmetric heterogeneous catalysis can be accomplished with immobilized enantioselective homogeneous catalysts, via diastereoselective transformation of chiral reactants, or on chirally-modified surfaces.^[40] The latter approach is technically rather simple and inexpensive, and there are many successful examples known which use chiral organic compounds to make ordinary metal catalysts enantioselective. Thus, platinum modified with cinchona alkaloids efficiently hydrogenates ketones possessing an electron-donor substituent in the α -position. Nickel modified with tartaric acid is in turn important in hydrogenation of β -functionalized ketones. Despite both catalysts are capable of providing stereoselectivity up to 90% *ee* (enantiomeric excess) and more, the mechanism of their action is not well understood yet. The enantioselective reactions are often very sensitive to variations in conditions, e.g., type of a solvent, temperature, modifier concentration, and hydrogen pressure.

It is clear that interaction of the modifier molecules with the reactant species and/or the catalyst is the key selectivity-determining factor. The most straightforward idea one can come up with is a direct interaction between modifier and reactant molecules adsorbed on a catalyst surface.^[41] Supramolecular chirality at the surface is another interesting concept implying that modifier species organize into ordered surface arrays and that such kind of chiral overlayers are primarily responsible for the enantiodifferentiation. It was also proposed that enantiospecific surface restructuring may occur upon adsorption of chiral modifiers and that the chiral metal sites being formed are relevant in the stereoselective transformations. In principle, a chiral modifier can also preferentially occupy the R- or S-kink sites, equally inhabiting polycrystalline metal catalysts, and leave the opposite type of the adsorption sites available for reactant molecules.

As shown in recent *in situ* spectroscopic studies, adsorbed modifier species interact with reactant molecules through hydrogen bonding.^[52-54] It is not surprising that large cinchona-like molecules, possessing multiple functionalities, are capable of forming stable diastereomeric complexes with pro-chiral adsorbates similarly to the function of enzymes, and there exist even indications of 1:1 complexation in the bulk solutions.^[55] The situation is drastically different with smaller modifiers like tartaric acid, where supramolecular self-assembly seems to be the dominant way of enantiodiscrimination.^[56] Generally, mechanistic insights into complex processes, such as heterogeneously catalyzed enantioselective reactions, can be at least partially obtained in model surface science studies.^[57]

2.1.2 Chirality at surfaces

Since a surface does not allow the symmetry elements parallel to its plane, molecular adsorption often leads to mirror symmetry breaking.^[58] As a result, the molecules which are normally achiral may become chiral upon adsorption. In heterogeneous catalysis, such pro-chiral species can be converted into chiral products (Fig. 2.1). Enantioselective catalysts differentiate between two possible structures and let only one of them to be preferentially formed. Catalysis at intrinsically chiral surfaces is an interesting research goal. As first proposed by Andrew Gellman in Pittsburgh, kinked step structured single crystal metal surfaces can be chiral themselves, if the kink sites have different step lengths or step faces.^[59] Gellman introduced an experimental methodology to characterize chiral surfaces by interaction with probe chiral adsorbates, and with this approach his group has extensively studied various high Miller index surfaces of multiple metals.^[60-64] Based on TPD, small differences in adsorption energetics between enantiomers have been reported. For example, desorption kinetics of lysine on chiral copper surfaces reveals enantiospecific difference of around 2.5 kJ mol⁻¹, namely L-Lysine adsorbs stronger on Cu(3,1,17)^R than on Cu(3,1,17)^S surface and D-Lysine, on the contrary, has higher affinity to Cu(3,1,17)^S than to Cu(3,1,17)^R.^[65]

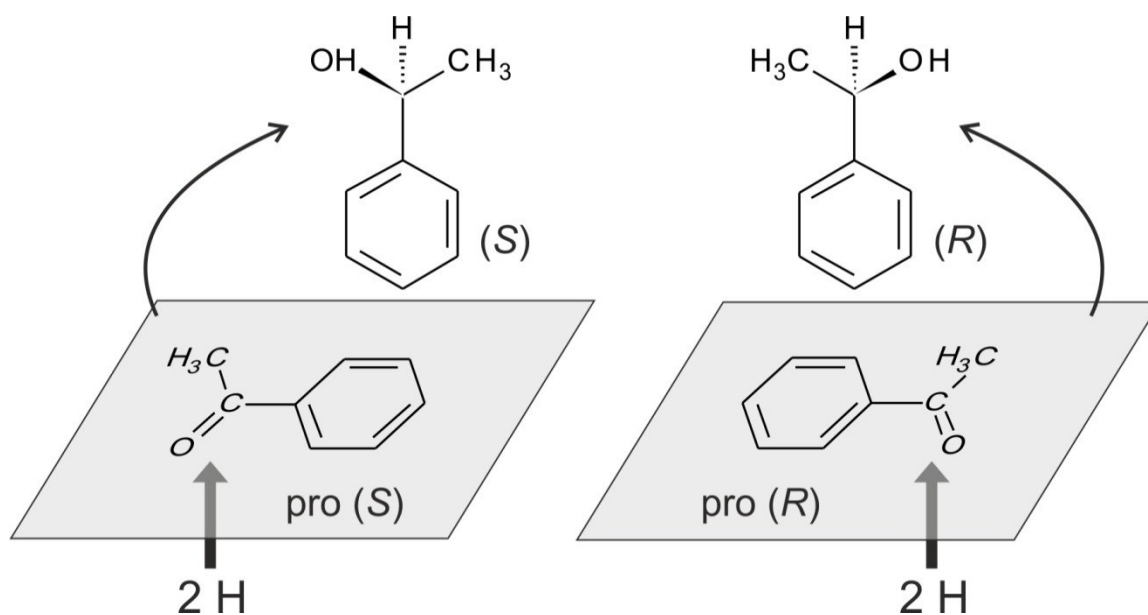


Figure 2.1 Schematic for enantioselective catalysis: *pro*-chiral phenylacetone becomes chiral upon adsorption; hydrogenation of the double bond by atomic hydrogen coming from the surface leads to the chiral products; if the surface is able to distinguish between two adsorbate geometries, only one enantiomer will be produced.

Although the significance of the naturally chiral metal surfaces has not been decisively demonstrated in the enantioselective synthesis, the UHV methodology pioneered by Gellman greatly facilitated model studies on chirally-modified catalysts. TPD titration experiments with chiral probe molecules have been similarly applied to the metal surfaces decorated by adsorption of modifier species.^[66, 67] Gellman's research has also put forward the idea of chiral surface restructuring, when energetically favorable enantiospecific adsorption can promote homochiral reconstruction of the initially achiral metal surface. As revealed by STM and LEED, molecules of tartaric acid adsorbed on Cu(110) can order the metal surface and imprint its chirality.^[68] Generally, surface microscopy together with vibrational spectroscopy have been widely employed in many laboratories for studying adsorption of chiral molecules on metal surfaces, including their interactions between themselves as well as with *pro*-chiral species.^[69-74] For instance, formation of a bimolecular modifier-reactant surface complex was directly

shown in the case of chiral NEA and pro-chiral 2,2,2-trifluoroacetophenone adsorbed on Pt(111).^[75]

Surface chemistry on chirally-modified precious metal surfaces has been extensively investigated by the groups of Wilfred Tysoe and Francisco Zaera.^[42] Following the TPD titration procedure, a number of different model chiral modifiers, including 2-butanol, proline, alanine, MBA and 2-aminobutanoate species, NEA, and tartaric acid, has been tested on catalytically relevant Pd(111) and Pt(111) surface.^[43, 44, 76-84] These studies have considerably complemented the models of docking 1:1 complexation and chiral templating. It is basically confirmed that larger molecules can transfer chiral information individually, whereas smaller adsorbates need to interact with each other in order to bestow surface chirality. Based on the results of these experiments, two specific systems have been elected to be characterized by SCAC in the present work: Pt(111) modified by NEA and Pt(111) modified by MBA. As adsorbing molecules, we use enantiomers of PO which has been previously shown to be a simple and effective chiral probe. In the above mentioned studies, enantioselective adsorption of PO was often detected via differences in the positions of desorption maxima and/or inequality of the integral areas under the TPD traces.^[43, 44, 67] PO adsorbs molecularly on Pt(111) binding to the surface via its oxygen atom, and desorption peaks for monolayer and multilayer states are well separated by about 50 K.^[85]

2.1.3 Chiral modifier 1-(1-naphthyl)ethylamine (NEA)

NEA is a synthetic compound which has been long used as a model for cinchona chiral modifiers. As compared to cinchona alkaloids, the molecular structure of NEA is rather simple; however, it still possesses all necessary functionalities immanent to natural modifiers (Fig. 2.2). The first required feature is an aromatic ring which is believed to anchor to the metal substrate. Furthermore, the modifier has to have a chiral carbon center capable of attractive intermolecular interactions. In the case of NEA, the role of a docking site is played by an amino group which can form hydrogen bonds. Despite its simplicity, NEA was intriguingly proved to be very efficient

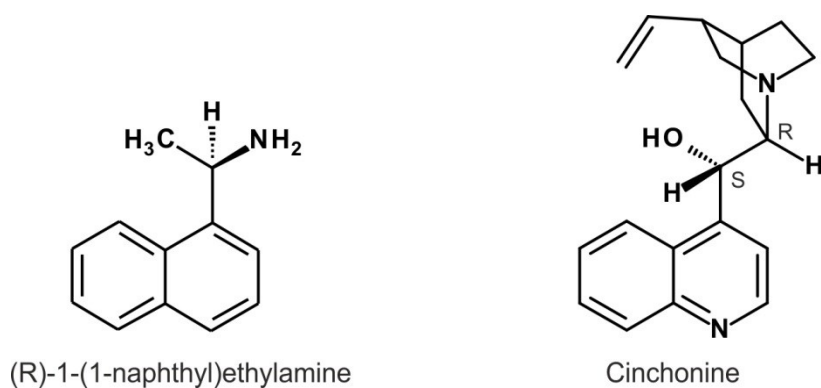


Figure 2.2 Molecular structure of *R*-NEA in comparison with that of the natural alkaloid cinchonine.

in enantioselective hydrogenation of ethyl pyruvate over Pt/alumina catalysts.^[86] Without any optimizations, it gives enantioselectivity up to 67% and also makes the reaction to be 6 times faster compared to the unmodified catalysts. Accordingly, many efforts have been dedicated to the microscopic characterization of NEA under well-controlled UHV conditions.

On Pt(111), NEA was found to adsorb molecularly at room temperature, and the complete monolayer is reached at coverage of $\sim 10^{14}$ molecules cm^{-2} which corresponds to 1 modifier molecule per almost 15 surface Pt atoms.^[87] As revealed by NEXAFS spectroscopy, S-NEA molecules are strongly tilted toward the surface normal, and the angle between the naphthalene ring and the surface plane equals to $\sim 45^\circ$. It was proposed that binding to the surface is accomplished both through the aromatic π -system and the lone electron pair of the amino group. Further TPD measurements showed that NEA adsorbates undergo stepwise decomposition as temperature exceeds 320 K.^[88] At coverages close to the saturation, STM data obtained in the same study revealed no long-range surface order for the NEA adsorbates, neither alone nor co-adsorbed with hydrogen, methyl pyruvate, and both together. It was the first surface science indication that NEA modifier works via the 1:1 docking mechanism rather than the templating one requiring ordered structures to be formed.

That conclusion was supported by the IRAS work by McBreen and co-workers who studied co-adsorption of NEA with methyl pyruvate on

Pt(111).^[89] Spectral signatures associated with the hydrogen bonding were identified, and formation of intermolecular NEA-methyl pyruvate complexes was proposed. Further evidence for the existence of such one-to-one surface complexes was obtained in TPD experiments, where stabilization effect of the docking interaction was demonstrated by a shift in the decomposition temperature for methyl pyruvate.^[90] As already mentioned, bimolecular complexation between NEA and 2,2,2-trifluoroacetophenone (TFAP) on Pt(111) surface was later visualized directly by STM.^[75] Furthermore, the authors managed to monitor the full cycle of the enantioselective hydrogenation of TFAP on R-NEA-modified Pt(111) in a UHV chamber.^[91] Successive chemisorption, chiral preorganization and hydrogenation were clearly distinguished. Similar diastereomeric complexes were also found between NEA and 3,3,3-trifluoropyruvate, methyl benzoylformate, and ketopantolactone.^[92-94]

Enantioselectivity in adsorption on Pt(111) modified by NEA was macroscopically examined by Zaera et al.^[44] They used PO enantiomers as a chiral probe and performed TPD and IRAS measurements. Molecular orientation of the adsorbed NEA molecules was confirmed to be non-parallel to the surface, even at low coverages. When co-adsorbed with PO, geometry of the NEA adsorbates was detected by vibrational spectroscopy to slightly change indicating some conformational rearrangements caused by intermolecular interactions. At the same time, there is a pronounced enantioselective effect seen in the TPD experiments. As revealed by the desorption spectra, the amount of PO which can be directly accommodated on the Pt surface greatly varies between different probe-modifier pairs, i.e. it can be twice as larger for the S-S combination compared to the R-S and vice versa. The effect strongly depends on the modifier coverage and reaches its maximum when NEA occupies approximately 50-65% of the surface. Moreover, in the presence of NEA, the PO desorption trace splits into two peaks separated by 25 K. For the homochiral probe-modifier combinations, the maxima of both peaks are shifted by 5 K towards higher temperature compared to the heterochiral pairs. These findings point to some kind of interplay between the one-to-one and the templating mechanisms of chirality

induction. Indeed, Monte Carlo simulations confirm that such behavior cannot be rationalized in terms of simple pairwise interactions, and cooperative effects between the modifier and probe adsorbates have to be considered instead.^[95]

In a similar manner, Tysoe and co-workers have studied structural and chemical properties of NEA-modified Pd(111) substrate.^[81, 96, 97] For the lone modifier, no ordered arrays were found with STM, and again the adsorbates were proved to be thermally stable below 300 K. Enantioselective chemisorption of PO and 2-butanol was explored by TPD and IRAS. PO enantiomers reveal no stereospecificity on NEA-covered Pd, while two regimes of enantioselectivity were clearly detected for 2-butanol. When NEA occupies ~55 % of the surface, a maximum enantioselective ratio of 2 was measured in favor of the homochiral probe-modifier combination. Additionally, a comparable effect was found at the modifier coverage of ~0.85 ML. Hydrogen bonding interactions between modifier and probe species as well as cooperative effects between them were concluded to be crucial for the enantioselective adsorption.

2.1.4 Chiral modifier 2-methylbutanoic acid (MBA)

MBA serves as a simplified analogue for the chiral modifiers employed in the enantioselective hydrogenation of β -ketoesters over Ni (Fig. 2.3). Despite originally used modifiers, e.g. tartaric and glutamic acids, possess hydroxyl and amino groups directly bonded to the chiral center, MBA is believed to fulfil the minimal structural requirements to model the templating mechanism of chiral induction. Thus, its molecules have a primitive chiral center, i.e. a tertiary carbon atom, and a carboxylic group acting as a surface anchoring moiety. Indeed, MBA was shown by IRAS and TPD to be adsorbed on Pd(111) via deprotonated carboxylates with an intact aliphatic skeleton.^[77] However, MBA overlayers do not produce enantioselective adsorption sites for PO, as opposed to its closest structural relatives 2-butanol and 2-aminobutanoic acid. Conformational rigidity was proposed to influence intermolecular interactions.



Figure 2.3 *Molecular structure of S-MBA in comparison with that of the natural (R,R)-tartaric acid.*

On the other hand, MBA does impart chirality to the Pt(111) substrate.^[43] As revealed by IRAS, MBA preserves its molecular structure at 100 K in the whole range of submonolayer coverages. Upon heating, the MBA adsorbates transform into carboxylate species at 230 K and completely decompose above room temperature. Co-adsorption of S-MBA and PO enantiomers was characterized both by TPD and IRAS. Prior to PO exposure, surface MBA was transformed into its carboxylate state by annealing at 230 K. Depending on MBA initial coverage, TPD traces reveal clear differences between R- and S-PO. First, the number of PO molecules desorbing from the Pt surface is appreciably higher for the homochiral combination, and the maximum ratio of the TPD yields amounts to 1.24. There is also a pronounced high-temperature shift in the desorption maxima of S-PO compared to the R-enantiomer, indicating a stronger interaction between the modifier and probe molecules of the same chirality.

The enantioselective effect is qualitatively confirmed in the vibrational spectra, where the intensity of the ring deformation band unequally redistributes between multilayer and monolayer states depending on the molecular chirality. Comparing their data with those reported by Tysoe's group, Zaera et al. proposed that chirality-bestowing behavior of organic adsorbates may depend on the nature of the underlying metal substrate. They also concluded that MBA modifier is likely to act through long-range surface ordering, and cooperative effects between the modifier and probe adsorbates were speculated as well.

2.2 Metal oxide surfaces

2.2.1 Surface chemistry of metal oxides

Although flat oxide surfaces can be in many cases prepared under well-defined UHV conditions by simple mechanical cleavage of a bulk single crystal, understanding of the surface chemistry on metal oxides has been long time lagged compared to bare metals. This is, on the one hand, due to low thermal and electric conductivity of oxide materials which gives rise to such undesirable effects as electrostatic charging during electron spectroscopy and microscopy experiments.^[98] It is also quite difficult to mount and heat such samples because of their brittleness. On the other hand, oxides surfaces are often of much more complex structure than metals, and model substrates with a desired set of properties, e.g., exact surface plane, certain stoichiometry, and defects concentration, are difficult to prepare. There are few metal oxides whose surface chemistry can be studied in detail with bulk samples, among them titanium dioxide is probably the most prominent example.^[99] For its rutile form, various low Miller index surfaces are readily available by crystal polishing, and electroconductivity of the substrates can be enhanced through simple UHV treatments.^[100]

In addition to the bulk cleavage and ordinary mechanical preparation, metal oxides can be grown in the form of thin single-crystalline films supported on conducting metal substrates.^[13] Macroscopic transport properties of such systems are dominated by a bulk metal, so the resulting oxides surfaces become accessible to any chemical analysis and morphology characterization technique.^[101] Structural properties of the oxide phase are essentially determined by epitaxial relations and can be within a certain range tuned, thereby enabling such important crystal characteristics as density of defects to be controlled. Another advantage of this methodology consists in that thin films can be easily sputtered away and, if necessary, fresh surfaces are relatively fast restored. In contrast to the bulk materials, purity of the epitaxial substrates can be very well controlled. Furthermore,

some experimental methods such as SCAC can only be applied to the supported oxides rather than bulk substrates.

The simplest method to produce an oxide film is oxidizing a pure metal or an alloy, and well-ordered oxide layers prepared by the direct oxidation are known, for example, for NiO(100) on Ni(100) and Al₂O₃ on NiAl(110).^[102, 103] Nevertheless, the most versatile preparation procedure is based on the physical vapor deposition, when a metal of interest is deposited onto an inert substrate followed or accompanied by an oxidative treatment. Varying the supporting material and its particular surface planes as well as introducing buffer layers, a great diversity of thin films can be prepared, and one can even find appropriate lattice matches allowing for different surfaces of the same oxide to be grown. The successful examples span magnesium oxide on Ag(100), Fe(100), Mo(100),^[104] zinc oxide on Pd(111), Pt(111), Cu(111),^[105] chromium oxide on Cu(111), Cu(100), Cu(110),^[106] ceria on Ru(1000), Ni(111),^[107] iron oxides on Pt(111), Pt(100), MgO(100),^[16] and many other binary and more complex metal oxides. As a rule, surface properties of the thin film substrates reproduce very well those of the bulk materials, hence being highly important models for the catalytic research.^[108]

Magnetite is an important oxide material whose chemical properties have been traditionally drawing attention of surface scientists. Since the chemical formula of magnetite is Fe₃O₄, it comprises both Fe²⁺ and Fe³⁺ oxidation states. This iron oxide has a crystal structure of the inverse spinel, in which oxygen anions are packed into a face-centered cubic sublattice providing octahedral and tetrahedral cation sites (Fig. 2.4).^[109] A half of all Fe³⁺ ions are distributed over the tetrahedral sites, while the octahedral positions are equally occupied by Fe³⁺ and Fe²⁺ cations. There is a rapid electron hopping between Fe²⁺ and Fe³⁺ ions occurring above 125 K, which imparts high electric conductivity to magnetite.^[110] Similar to titanium dioxide, surface properties of magnetite have been studied with ordinary single crystals samples.^[111, 112] However, the thin films approach can offer additional advantages over the bulk material. As multiple phases exist in the iron-oxygen binary system (Fe₂O₃, Fe₃O₄, FeO), the use of the supported substrates was proved to be more convenient in studying equilibrium bulk

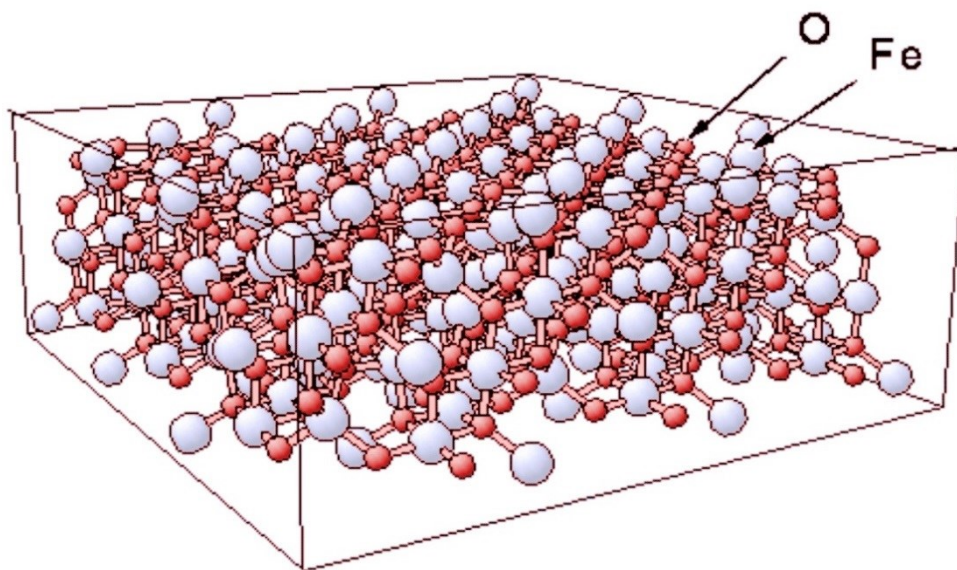


Figure 2.4 *Crystal structure of magnetite.*[□]

and surface structures.^[109] To date, a vast amount of research has been conducted with iron oxides thin films which provide a solid justification of choosing magnetite as a subject of the present study. Comparison of chemical properties for the most abundant (111) and (100) magnetite surfaces by SCAC seems to be a fairly achievable research goal.

2.2.2 Thin $\text{Fe}_3\text{O}_4(111)$ film

Perpendicular to the [111] direction, the magnetite crystal lattice has close-packed hexagonal oxygen arrays stacked into an ABC lateral sequence.^[113] The oxygen layers are separated by two alternating types of iron layers. A side view of the Fe_3O_4 structure and top views of the cation layers are shown in Figure 2.5. The so-called Kagomé layers contain octahedrally coordinated iron cations which occupy $\frac{3}{4}$ of all available sites and organize into a periodic structure with a ~ 6 Å hexagonal unit cell. Iron located in this plane is a 1:2 mixture of the Fe^{3+} and Fe^{2+} states. In turn, the mix-trigonal configuration consists of both octahedral and tetrahedral positions, and the

[□] The figure has been taken from the Balsac Picture Gallery at <http://www.fhi-berlin.mpg.de/KHsoftware/-Balsac/pictures.html> based on the Balsac software, Version 4, by K. Hermann (FHI), Berlin, 2015; see also <http://www.fhi-berlin.mpg.de/KHsoftware/-Balsac/index.html>.

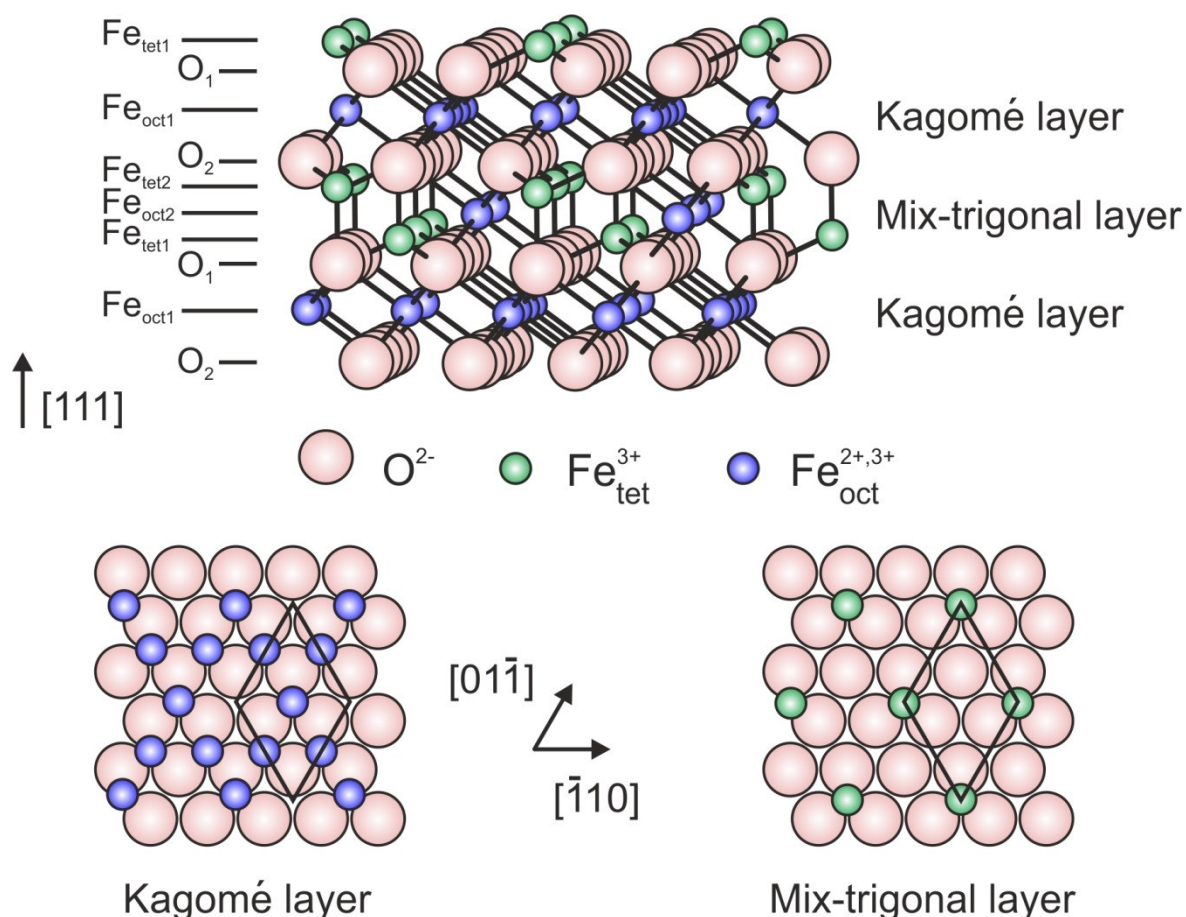


Figure 2.5 Side and top views of the Fe_3O_4 lattice along the $[111]$ direction. Stacking sequence of atomic arrays and bulk-truncated surface terminations are depicted on the side view. Top views show two types of iron layers.

iron cations are actually situated in three parallel planes. There are tetrahedrally coordinated Fe^{3+} next to each of the two opposite oxygen layers, whereas octahedral species comprise the middle cation array. In each of these layers, cations form hexagonal periodicity with the same lattice constant of $\sim 6 \text{ \AA}$. As depicted in Figure 2.5, six formal bulk-truncated terminations are possible for the (111) surface of magnetite. O_1 and O_2 are two close-packed oxygen terminations whose atomic density defines a surface monolayer ($\sim 1.3 \cdot 10^{15} \text{ cm}^{-2}$). If the crystal is truncated by the Kagomé layer, one has $\text{Fe}_{\text{oct}1}$ surface termination characterized by $\frac{3}{4}$ ML of iron atoms over an oxygen layer. Correspondingly, $\text{Fe}_{\text{tet}1}$ and $\text{Fe}_{\text{tet}2}$ terminations expose $\frac{1}{4}$ ML of cations in tetrahedral positions, and $\text{Fe}_{\text{oct}2}$ termination exposes $\frac{1}{4}$ ML of sixfold-coordinated Fe.

From the experimental point of view, there is no consensus on the thermodynamically most favorable surface structure reached, and several models have been proposed depending on preparation conditions. Early STM and LEED studies on polished natural $\text{Fe}_3\text{O}_4(111)$ crystals revealed coexistence of two different terminations.^[114] The first one shows features separated by 6 Å and exposes $\frac{3}{4}$ ML of iron atoms and $\frac{1}{4}$ ML of oxygen atoms. It was ascribed to the O-capped $\text{Fe}_{\text{oct}1}$ termination, where an O atom occupies the center of the Fe triangle in the Kagomé layer. The second structure exhibiting a honeycomb pattern with a 3.6 Å periodicity was attributed to the $\text{Fe}_{\text{oct}2}$ termination and was predicted to be more stable. When a sample is prepared under reducing conditions, a reconstructed surface appears which represents a biphasic ordering between $\text{Fe}_3\text{O}_4(111)$ and $\text{FeO}(111)$ islands.^[115] On the contrary, a highly regular oxygen terminated surface forming a 42 Å superstructure is found, if the final annealing step is followed by cooling in oxygen atmosphere.^[116] Moreover, annealing at 1123 K gives rise to three coexisting surfaces: $\text{Fe}_{\text{tet}1}$ and oxygen capped $\text{Fe}_{\text{tet}1}$ and $\text{Fe}_{\text{oct}2}$ terminations.^[117] Interchange between different terminations was further demonstrated to occur depending on oxidizing/reducing preparation conditions.^[112, 118]

Similarly, surface termination of epitaxial $\text{Fe}_3\text{O}_4(111)$ films seems to vary with the growth parameters. Weiss and co-workers originally found the relaxed $\text{Fe}_{\text{tet}1}$ termination to be a dominant structure formed after a final oxidation step at 1000 K.^[113] For lower oxidation temperatures ~ 870 K, several additional terminations were identified which are the biphasic in nature and cover 5-15 % of the film surface.^[119] However, further experiments by Shaikhutdinov *et al.* on CO adsorption pointed to the $\text{Fe}_{\text{oct}2}$ termination.^[120] Sala *et al.* showed later that the $\text{Fe}_{\text{tet}1}$ termination appears only if the sample is finally annealed in UHV at 900 K, otherwise small FeO islands are observed.^[121] However, a recent XPS and XAS study indicated Fe^{3+} enrichment of the $\text{Fe}_3\text{O}_4(111)$ surface region and octahedral cation environment.^[122]

A standard recipe for the $\text{Fe}_3\text{O}_4(111)$ film growth employs a $\text{Pt}(111)$ substrate as a support and is a multistep process.^[16] The procedure has

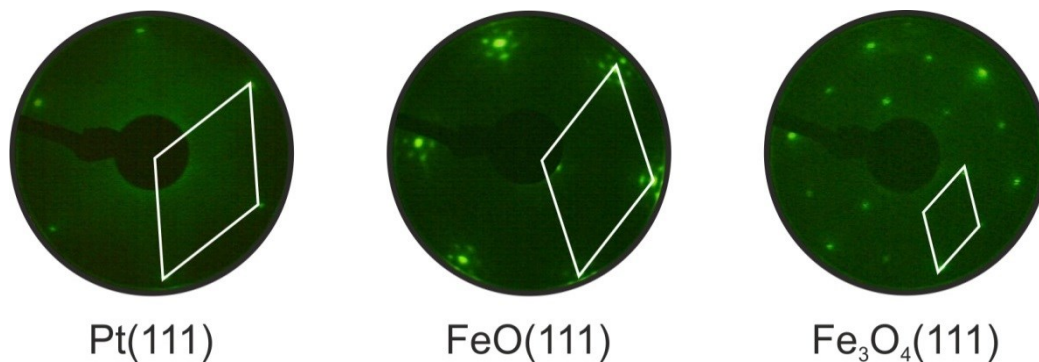


Figure 2.6 *LEED patterns (at 50 eV) of Pt(111), FeO(111) and Fe₃O₄(111) during epitaxial oxide films growth on Pt(111) substrate.*

been successfully adapted to be used with 1 μm thick Pt crystals in SCAC studies.^[37] The Pt(111) surface is preliminary cleaned by repeated cycles of argon sputtering followed by UHV annealing at 1200 K and annealing in 10^{-6} mbar oxygen atmosphere at 1000 K. A clean Pt(111) surface shows a sharp hexagonal LEED pattern (Fig. 2.6). The oxide preparation procedure starts with a deposition of an atomic layer of iron at room temperature which is then transformed into a FeO bilayer film. Experimentally, a 1 \AA thick iron layer is deposited in UHV at a deposition rate of $\sim 1 \text{ \AA min}^{-1}$ and subsequently oxidized for 5 min at 1000 K in $5 \cdot 10^{-7}$ mbar O_2 . The oxygen pressure is preserved upon cooling down until the temperature reaches 500 K. The FeO bilayer completely wets the Pt(111) substrate and has an O-terminated hexagonal closed-packed structure. Figure 2.6 illustrates a characteristic LEED image consisting of the superimposed FeO and Pt patterns. The main diffraction spots of the FeO lattice are surrounded by satellite spots which may originate from multiple diffraction processes between Pt(111) and the oxide overlayer. There is also a rotational mismatch between the FeO layer and Pt(111) surface leading to a so-called Moiré superstructure which is characterized by a 25 \AA periodicity and may contribute to the satellite spots.

After the FeO layer is prepared, the sample is kept at a low temperature to make a thin crystal flat enough and enable LEED diffraction to be detected. Therefore, further iron deposition is done at $T < 150 \text{ K}$, and before

the sample is always flashed to 700 K to remove gas residuals adsorbates. A ~5 nm thick Fe₃O₄ film is produced via six successive growth cycles. Each cycle includes deposition of 4 Å of iron followed by 5 min oxidation at 873 K in O₂ at pressure of 5·10⁻⁷ mbar (8·10⁻⁷ mbar for the last two cycles). Again, oxygen is only pumped out when the sample cools down to 500 K. Fe₃O₄ was shown to grow in the Stranski–Krastanov mode. When Fe₃O₄ islands coalesce and a closed film is formed, one can observe a characteristic hexagonal LEED pattern which appears as a (2×2) superstructure in respect of the Pt(111) surface (Fig. 2.6).

2.2.3 Thin Fe₃O₄(100) film

Two types of atomic arrays, usually termed as A and B layers, alternate along the [100] direction of the magnetite crystal structure (Fig. 2.7).^[123] The A layer contains only tetrahedrally coordinated Fe³⁺ cations arranged into a periodic structure with a fourfold rotational symmetry. The mixed B layer consists of oxygen atoms and octahedrally coordinated iron atoms forming rows in the [110] direction. Although two bulk-truncated terminations are possible for the Fe₃O₄(100) surface, neither of them is found experimentally. Instead, a ($\sqrt{2}\times\sqrt{2}$)R45° surface reconstruction is commonly observed in LEED on both epitaxial and natural samples.^[124, 125] There have been longstanding debates on the atomic nature of this reconstruction, and only recently a comprehensive model has been elaborated.^[126-130] Based on IV-LEED, STM, and DFT calculations, Bliem *et al.* showed that distorted bulk-truncated B termination is actually stabilized by an ordered array of subsurface cation vacancies (SCV).^[131] In this model, two octahedrally coordinated iron cations are missing in the third layer, while one iron atom appears as an interstitial in the second A layer. The SCV structure was calculated to be thermodynamically favorable in a wide range of oxygen pressure up to 10⁻⁵ mbar, and inter alia it gracefully explains the appearance of highly stable not conglomerating metal adatoms deposited on Fe₃O₄(100) surface.^[132, 133]

Similar to Fe₃O₄(111), epitaxial Fe₃O₄(100) films are well-known model substrates. MgO(100) was originally proposed to be an appropriate support

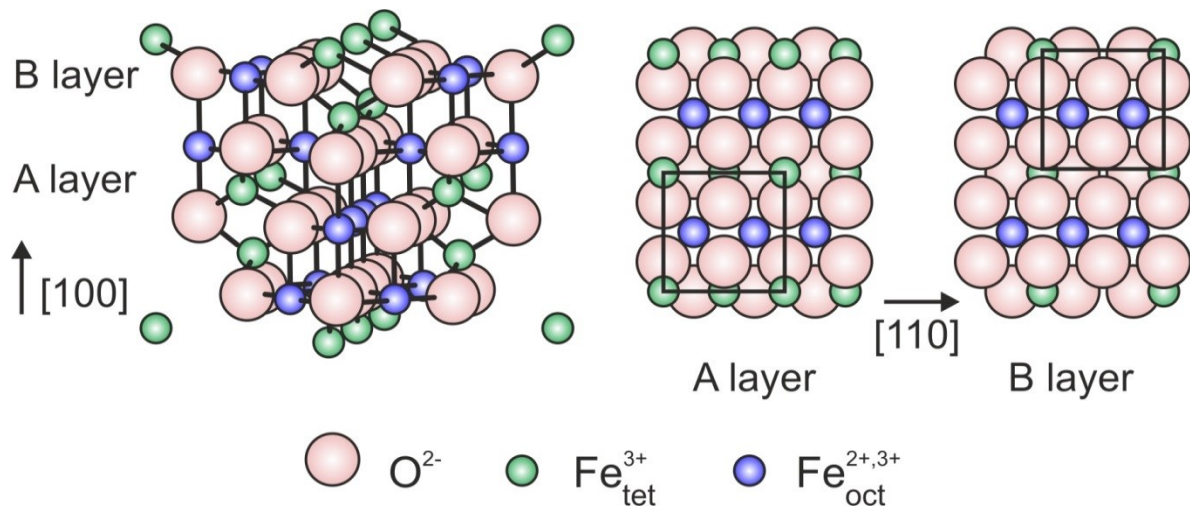


Figure 2.7 Side and top views of the Fe_3O_4 lattice along the $[100]$ direction. Stacking sequence of atomic arrays is shown on the side view. Top views illustrate two types of ideal bulk-truncated surface terminations.

for growing $Fe_3O_4(100)$ films with a small lattice mismatch of 0.3 %.^[134] Initially, Chambers and co-workers employed oxygen plasma to assist oxide growth directly on a polished and UHV cleaned MgO crystal.^[135] Iron deposition onto a cleaved MgO crystal in 10^{-7} - 10^{-6} mbar oxygen atmosphere also gave satisfactory results.^[136, 137] Later Korecki *et al.* improved the preparation by introducing a thin Fe(100) buffer layer.^[138] Reactive iron deposition at 520 K in 10^{-6} mbar O_2 followed by 1 hour annealing at 770 K gives a very stable $(\sqrt{2} \times \sqrt{2})R45^\circ$ reconstructed surface. Alternatively, $Fe_3O_4(100)$ films can be grown on a Mo(100) substrate.^[139] In this case, iron is deposited at 570 K in 10^{-7} mbar O_2 with two subsequent annealing steps in UHV and 10^{-8} mbar O_2 . Davis *et al.* have recently developed a new procedure for preparing magnetite films on Pt(100).^[140] It is also based on reactive deposition and requires creation of an iron buffer layer. The thickness of the buffer layer was shown to be very crucial for the (100) growth, and different surface terminations can be obtained depending on the preparation conditions.

Since operation of SCAC was proved to be very convenient with ultrathin Pt crystals, the $Fe_3O_4(100)$ preparation by Davis *et al.* has been employed in the present study. The recipe for the most stable $(\sqrt{2} \times \sqrt{2})R45^\circ$ surface was

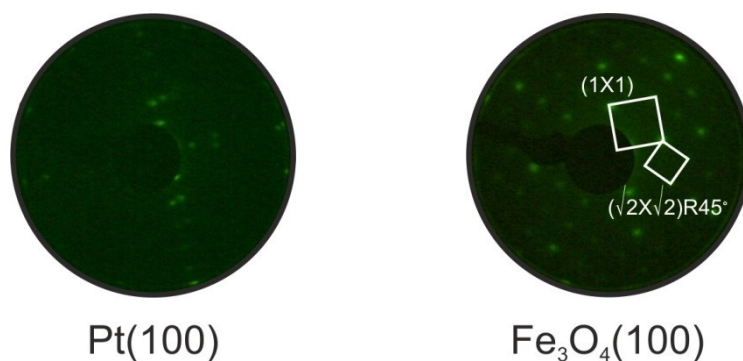


Figure 2.8 LEED patterns of Pt(100) (at 50 eV) and Fe₃O₄(100) (at 95 eV) during epitaxial oxide film growth on Pt(100) substrate.

slightly modified in order to enable the SCAC experiments to be reasonably fast repeating. The Pt(100) surface is cleaned as described above for the case of Pt(111), and during oxide growth it is kept at room temperature. A 3 nm iron buffer layer is deposited first in UHV at a deposition rate of $\sim 1 \text{ \AA min}^{-1}$. Afterwards, oxygen is introduced into the chamber, and iron deposition is continued in 10^{-6} mbar O₂. When amount of deposited iron corresponds to the effective thickness of 3 nm, the deposition is stopped, and oxygen is pumped out. Three successive annealing steps are then carried out: 1) 20 min in UHV at 880 K; 2) 20 min in UHV at 1080 K; 3) 5 min in $5 \cdot 10^{-7}$ mbar O₂. Eventually, a LEED pattern corresponding to the $(\sqrt{2} \times \sqrt{2})R45^\circ$ reconstruction is reached, as shown in Figure 2.8.

2.2.4 Water on iron oxides

Interaction of water with magnetite surfaces has been amply studied both on bulk single crystals and epitaxial films. Room-temperature XPS experiments indicated that both (111) and (100) Fe₃O₄ crystals readily undergo hydroxylation which commences at $\sim 10^{-5}$ mbar H₂O and can, at higher exposures, penetrate several layers deep.^[50] As recently specified by Kendelewicz *et al.*, adsorbed water can persist in its molecular nature on Fe₃O₄(100) even up to 10^{-4} - 10^{-2} mbar pressure.^[51] Conversely, surface hydroxyls on Fe₃O₄(111) were found at 10^{-6} mbar H₂O and temperatures below 240 K.^[141] These apparent contradictions are believed to originate from

a strong coverage dependence of the surface reaction, i.e. the intermolecular mechanism of water dissociation was proposed to play a significant role.

Low coverage water chemistry on epitaxial $\text{Fe}_3\text{O}_4(111)$ films was studied in detail under UHV conditions by Weiss and co-workers.^[49, 142, 143] As revealed by TPD and photoelectron spectroscopy, three adsorption states are sequentially populated on $\text{Fe}_3\text{O}_4(111)$. The most strongly bound γ -species desorb at 270-280 K and were ascribed to the dissociated water. It was proposed that hydroxyl groups occupy the topmost iron atoms of the $\text{Fe}_{\text{tet}1}$ surface, while protons are able to move over the corresponding oxygen atoms. Saturation coverage for these species was estimated to be in the order of the density of surface unit cells. Equilibrium adsorption isobars recorded at water partial pressure of 10^{-8} , 10^{-7} , and 10^{-6} mbar yielded adsorption energy of the γ -species to be 60-73 kJ mol^{-1} , in contrast to the analysis of the second-order desorption kinetics which gave only 50 kJ mol^{-1} . At higher water coverages, β - and α -species appear which are similar to those on oxygen terminated $\text{FeO}(111)$ film and were attributed to the physisorbed molecular water and condensed ice multilayers, respectively. Interestingly, the amount of the physisorbed water molecules was found to equal to that of the dissociated species, and the authors proposed that they reside on the three-fold hollow sites filling the space between the surface hydroxyl groups. These findings were later supported by infrared spectroscopy experiments.^[48] As shown by Leist *et al*, low coverage water adsorbates on $\text{Fe}_3\text{O}_4(111)$ exhibit two absorption bands at 2712 and 2691 cm^{-1} which were assigned to the discussed above γ -species. The peak at 2590 cm^{-1} arising upon higher water exposures was identified to originate from hydrogen bonding between dissociated and molecular water. A dimer-like structure was proposed, in which an oxygen atom from the intact water molecule bridges two hydrogen atoms of the dissociated species. Basic aspects of water surface chemistry under UHV conditions have been also confirmed by XPS, TPD, and STM studies on bulk $\text{Fe}_3\text{O}_4(111)$ samples.^[144-146]

Early TPD experiments with water on epitaxial $\text{Fe}_3\text{O}_4(100)$ films showed three adsorption states in the first layer which have approximately equal saturation concentrations and desorb at 225, 280, and 300 K.^[147] Diebold

and co-workers studied room temperature adsorption of water on a bulk $\text{Fe}_3\text{O}_4(100)$ crystal and found an unprecedented behavior.^[148] After the clean oxide surface is exposed to water vapor, STM measurements show only one type of surface hydroxyls, namely H atoms accommodated on the oxygen sublattice. Upon increasing exposure, the monolayer coverage of these species can be reached, however the other type of hydroxyls containing oxygen from water molecules is never seen on the surface, neither in STM nor in He^+ low energy ion scattering (LEIS). Instead, surface hydrogen was shown to desorb at 520 K subtracting lattice oxygen atoms and forming gaseous H_2O . The authors concluded that H_2O dissociates on $\text{Fe}_3\text{O}_4(100)$, but due to the geometry reasons OH groups formed out of the water molecules efficiently disproportionate at room temperature and readily leave the surface enabling protons to accumulate on the oxide. Liu *et al.* have recently reported AES, LEED, UPS, and HREELS data on adsorption of water on $\text{Fe}_3\text{O}_4(100)$ films grown on $\text{Mo}(100)$.^[139] Water was found to dissociate at temperatures as low as 150 K, and up to 240 K dissociated species were shown to coexist with hydrogen bonded molecular adsorbates. Above that temperature, hydroxyls are likely to be only hydrogen atoms bound to the lattice oxygen and persisting on the surface up to ~400 K.

2.3 Single-crystal adsorption calorimetry

2.3.1 Principles

As a method for probing energetics of adsorbate-surface interactions, single crystal adsorption calorimetry necessarily includes two simultaneous types of measurements. First, the amount of heat released upon gas adsorption and/or a subsequent surface reaction is quantified by a pyroelectric detector. Second, a sticking coefficient enabling the molar adsorption energy and the absolute surface coverage to be determined is measured by a mass-spectrometer. Under the adiabatic assumption, adsorption of 1 % of a monolayer would typically heat up an ultrathin sample by several mK. Practically, if the desired number of gaseous species interacts with the surface over a long period of time, heat transfer from the sample to the detector can be totally suppressed by dissipation into the surroundings. In SCAC experiments, adsorbing molecules are therefore supplied to the surface in the form of short molecular beam pulses. Being a directional gas flow with a very precise spatial distribution, a molecular beam provides stable fluxes of high enough intensity and can be divided into fixed doses containing a well-defined number of molecules.

Figure 2.9 illustrates the principle of a SCAC experiment. An ultrathin single-crystal sample is supported by a hollow frame, so that its backside can be brought into a gentle mechanical contact with a pyroelectric detector. The detector represents a thin β -polyvinylidene fluoride (PVDF) ribbon which is bent into a flexible arc and coated on both sides with metal for electrical contacts. The sample is positioned in front of the last molecular beam orifice (not shown) and can be exposed to gas pulses with well-controlled duration on the millisecond timescale. Adsorption of molecules causes a transient heat release and a corresponding temperature rise in the sample, and due to the thermal contact a part of this energy is transferred to the detector. In response to the heat input the pyroelectric ribbon produces a face-to-face current signal which is amplified and measured electronically. A typical calorimeter output is shown in Figure 2.10a.

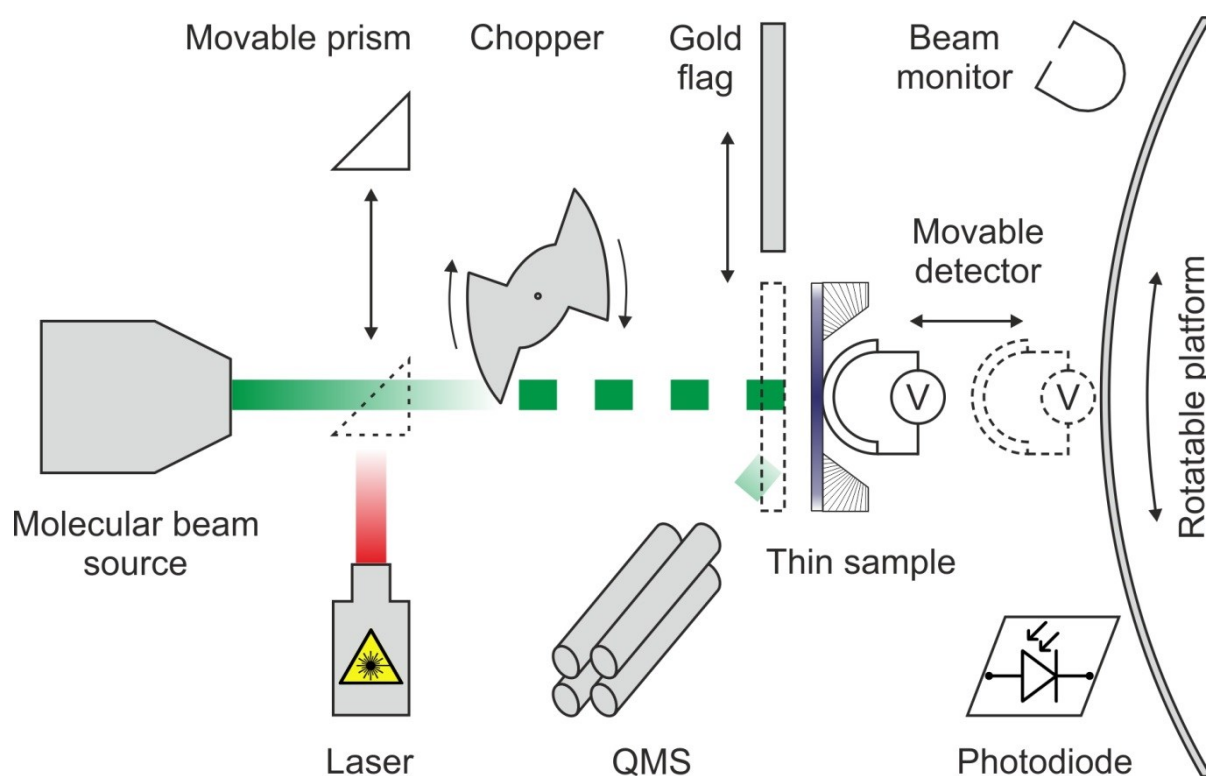


Figure 2.9 Schematic representation of the SCAC apparatus. The sample, the pyroelectric detector, the photodiode as well as the beam monitor are located on a movable housing and can be all positioned in the same place in front of the beam opening. The calibration laser is outside the chamber, and its shutter and the UHV window are not shown on the diagram.

Absolute calorimeter calibration is attained with the help of laser radiation of known intensity. Specifically, a light beam from a He-Ne laser is introduced into the UHV chamber and passes through the same collimation path as the molecular beam. Immediately following the heat measurement, the molecular beam is closed and the sample is irradiated by the identically modulated laser beam. The sample absorbs the light, and a corresponding temperature change is also registered by the pyroelectric detector (Fig. 2.10a). Calorimeter signals produced by absorption of radiation and gas adsorption are usually of the same shape and can be easily compared by their height. Afterwards, a photodiode is placed in the sample position, and the laser power is measured *in situ*. Providing the sample reflectivity at the laser wavelength is known, a correspondence between the energy input and the detector output can be strictly established for a given thermal contact.

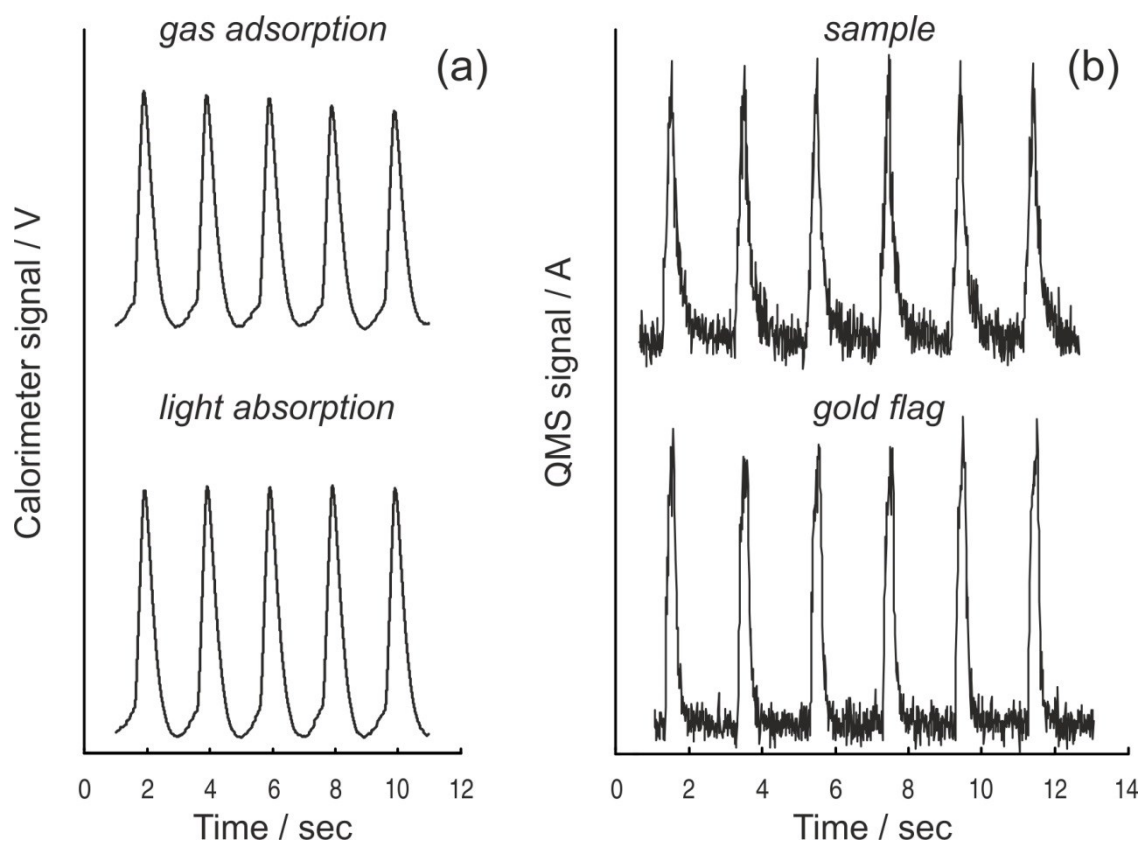


Figure 2.10 Examples of row SCAC data. a) Calorimeter signals upon adsorption of 266 ms long pulses of H_2O on $\text{Fe}_3\text{O}_4(111)$ at 120 K and corresponding calibration by laser irradiation of the same modulation. b) QMS signals recorded when 266 ms pulses of CO_2 impinge on a $\text{Fe}_3\text{O}_4(111)$ sample at 180 K and on a gold flag at 300 K respectively.

To obtain the number of molecules contributing to a certain calorimeter signal, the sticking coefficient is measured simultaneously with the energy. According to the King-Wells method, a quadrupole mass-spectrometer is located out of sight of the sample, so that molecules scattered from the surface can be quantitatively detected (Fig. 2.10b). If such a pressure rise is rationed to that recorded on the inert gold flag, where all molecules are reflected, one obtains a fraction of molecules sticking to the surface at a certain gas pulse. In practice, the entire area under QMS signals has to be considered in order to account slowly desorbing adsorbates. The flux and the cross-section of the molecular beam can be precisely determined by the beam monitor which is a stagnation chamber equipped with a high accuracy ion gauge.

2.3.2 Enthalpimetric analysis

The energy release q and the sticking coefficient s represent the primary SCAC data for every molecular beam pulse impinging on the sample surface. Since the pulse duration t is a priori known, the total number of molecules n in a single gas pulse is defined by a simple relation:

$$n = \sigma \cdot F \cdot t$$

where the beam cross-section σ and the flux F are independently determined parameters. Correspondingly, the number of adsorbates N_{ads} producing an energy signal q at a given molecular beam pulse is obtained as a product:

$$N_{ads} = n \cdot s$$

where the sticking coefficient s is also a function of the pulse number j . Next, the molar heat of adsorption Q_{cal} can be determined as following:

$$Q_{cal} = \frac{q \cdot N_A}{N_{ads}}$$

where N_A is the Avogadro constant.

To calculate the absolute surface coverage θ achieved upon adsorption of the j^{th} gas pulse, one has to sum up the number of molecules stuck to the sample during all previous pulses rationed to the adsorbate surface area:

$$\theta(j) = \frac{1}{\sigma} \cdot \sum_0^j N_{ads}(j) = F \cdot t \cdot \sum_0^j s(j)$$

It should be noted that the sticking coefficient s and the energy release q may have constant nonzero values even after the surface coverage θ reaches its saturation value at given temperature. This is due to the fact that saturation coverage also depends on the pressure, and it may differ upon molecular beam exposure and under UHV conditions. Therefore adsorbed molecules may partly desorb before the next molecular beam pulse arrives. In such a situation, two types of sticking coefficients are computed over different integration periods in order to accurately determine Q_{cal} and θ .

Generally, the temperature of adsorbing molecules delivered to the surface by a beam pulse is different from the substrate temperature. While

the sample temperature T_{sample} is a pre-set calorimeter temperature, the temperature of the gas does not equal to that of the molecular beam source T_{source} . Indeed, according to the Maxwell-Boltzmann distribution the root mean square speed of molecules in a flow differs from that in a volume. For an effusive source, average kinetic energy of molecules in the beam exceeds molecular translational energy in the stagnation chamber by $\frac{1}{2} RT_{source}$, where R is the gas constant. Thus, one can distinguish two major contributions to the heat release measured in a SCAC experiment. The first one is associated with the thermal equilibration, when arriving gas-phase molecules adopt the calorimeter temperature. The second term encompasses all isothermal energy changes in the interacting adsorbate-surface system such as enthalpy changes due to bond breaking and bond formation, any work done by the system, energetic effects caused by lateral interactions between adsorbates, etc.

In the course of the present study, we deal with adsorption energy E_{ads} which is defined as following:

$$E_{ads} = Q_{cal} - \int_{T_{sample}}^{T_{source}} (C_v + \frac{1}{2} R) dT$$

where C_v refers to the heat capacity of a gas at constant volume, and the integral accounts for the thermal equilibration. Since most experiments are conducted at cryogenic temperatures ($\ll 300$ K), when sticking coefficients are very close to unity, the impact of desorbing molecules is neglected. Although SCAC yields differential adsorption energy $E_{ads}(\theta)$, i.e. a detailed function of surface coverage measured during incremental adsorption, an integral value over a certain coverage range can be derived as well.

As discussed, the introduced quantity E_{ads} is directly related to the thermodynamic parameters of a gas-solid system being at temperature T . According to the first law of thermodynamics, its negative can be expressed in a generalized form:

$$-E_{ads} = \Delta U + W$$

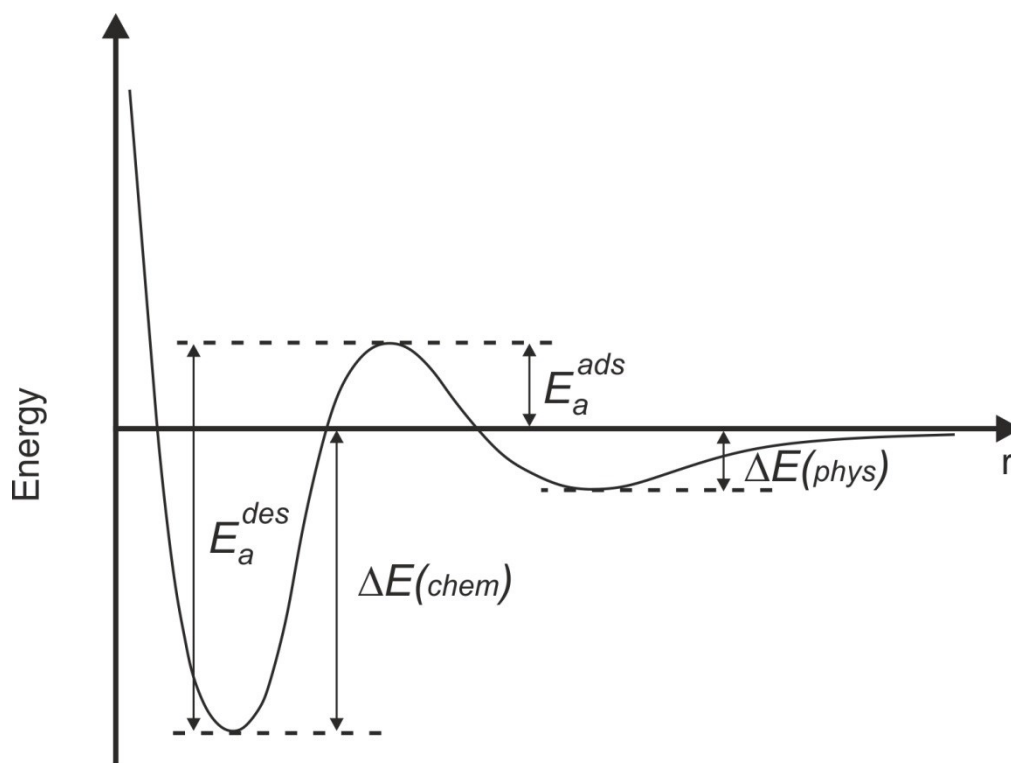


Figure 2.11 Lennard-Jones representation of a potential energy diagram for precursor-mediated dissociative adsorption. $\Delta E(\text{phys})$ is adsorption energy for the molecular precursor state; $\Delta E(\text{chem})$ is adsorption energy for the dissociated state; E_a^{ads} is activation energy for adsorption, E_a^{des} is activation energy for desorption.

where ΔU is a total energy change associated with all internal degrees of freedom (it has a negative sign because energy lowers upon adsorption) and W is a work done by the system (with a positive sign). It is often the case that W is much smaller than ΔU , particularly if it comprises only the gas-phase pressure-volume work usually amounting to the order of RT . Therefore, E_{ads} can be considered as a measure of the driving force for adsorption and, if applicable, it correlates with the energetic characteristics obtained by other experimental techniques.

Figure 2.11 illustrates schematically a potential energy curve for a complex adsorption process containing a molecular precursor state and activated dissociation. $\Delta E(\text{phys})$ is an energy gain acquired upon the physisorption process, and at the same time it is the minimal amount of energy required molecular adsorbates to leave the surface and return back

to the gas phase, i.e. activation energy for desorption E_a^{des} . In contrast, activation energy for desorption from the dissociated state is a sum of adsorption energy $E(chem)$ and activation energy for adsorption E_a^{ads} . Thus, adsorption energy measured in the SCAC experiments equals to the activation energy for thermal desorption only in case of physisorption and non-activated chemisorption, that is if $E_a^{ads} \leq 0$.

In temperature-programmed desorption (TPD) studies, the Arrhenius activation energy for desorption is extracted from the Polanyi-Wigner equation:

$$r_{des} = -\frac{d\theta}{dt} = -v_n(\theta) \cdot \exp\left(-\frac{E_{des}(\theta)}{kT}\right) \cdot \theta^n$$

where the experimentally determined desorption rate r_{des} is expressed as a function of temperature and surface coverage θ with a desorption order n . Since the pre-exponential frequency factor $v_n(\theta)$ is the second unknown in this equation, TPD analysis usually requires some sort of assumptions. For example, in the simple Redhead analysis the coverage dependence is completely neglected, and the prefactor v is accepted to be in a reasonable range of values, so that activation energy for desorption is related to the peak maximum temperature T_{max} taken from the TPD spectra:

$$E_{des} = RT_{max} \cdot \left[\ln\left(\frac{v \cdot T_{max}}{\beta}\right) - 3.46 \right]$$

where β is an experimentally controlled heating rate.

On the other hand, weakly bound adsorbates, such as those with adsorption energy $\Delta E(phys)$ in Figure 2.11, can be treated as a separate thermodynamic phase. The classical machinery for describing phase transitions is then applicable to such reversible processes, providing that adsorbed species are truly equilibrated with the gas phase. The method of equilibrium adsorption isobars/isotherms (EAI) is based on the Clausius-Clapeyron equation:

$$\left(\frac{\partial \ln p}{\partial T}\right)_\theta = -\frac{q_{st}}{RT^2}$$

where p is the pressure in the gas phase, and the isosteric heat of adsorption q_{st} defined at a certain surface coverage θ is nothing as the adsorption energy measured in calorimetry. In theory, EAI also allows for isosteric heat of adsorption to be determined as a function of surface coverage. At least two pairs of temperature and pressure giving rise to the same coverage value have to be known in order to enable the Clausius-Clapeyron analysis:

$$\ln\left(\frac{p_1}{p_2}\right) = \frac{q_{st}}{R} \cdot \left(\frac{1}{T_1} - \frac{1}{T_2}\right)$$

2.3.3 SCAC experimental setup

The SCAC apparatus at the Fritz Haber Institute was designed to enable adsorption calorimetry studies on complex model catalysts.^[30] Figure 2.12 illustrates schematically the primary elements of the experimental setup. It consists of two UHV chambers separated by a gate valve, and the sample transfer between the chambers is performed by a long-range translational rod. The preparation chamber is equipped with a variety of sample treatment capabilities and allows for preparation of different well-defined substrates, including supported metal nanoparticles. Adsorption experiments are conducted in the calorimetry chamber which is integrated with a molecular beam source. Both chambers as well as the transfer rod section are pumped by individual turbo molecular pumps (TMP) and have base pressure better than $2 \cdot 10^{-10}$ mbar; if necessary, they all can be opened independently. In the following, experimental techniques and methods which are particularly relevant for the present work will be described and discussed in detail.

Ultrathin Pt single crystals (both 111 and 100 orientations) are supplied by Jacques Chevallier from the Department of Physics and Astronomy at Aarhus University in Denmark and represent 1 μm thick films grown by physical vapor deposition (PVD) on appropriately prepared NaCl crystals. After dissolving the salt support, a Pt sample is mounted on a rigid Mo holder and becomes accessible to ordinary UHV procedures. The unsupported part of the thin crystal has the circular shape with a diameter of 8 mm.

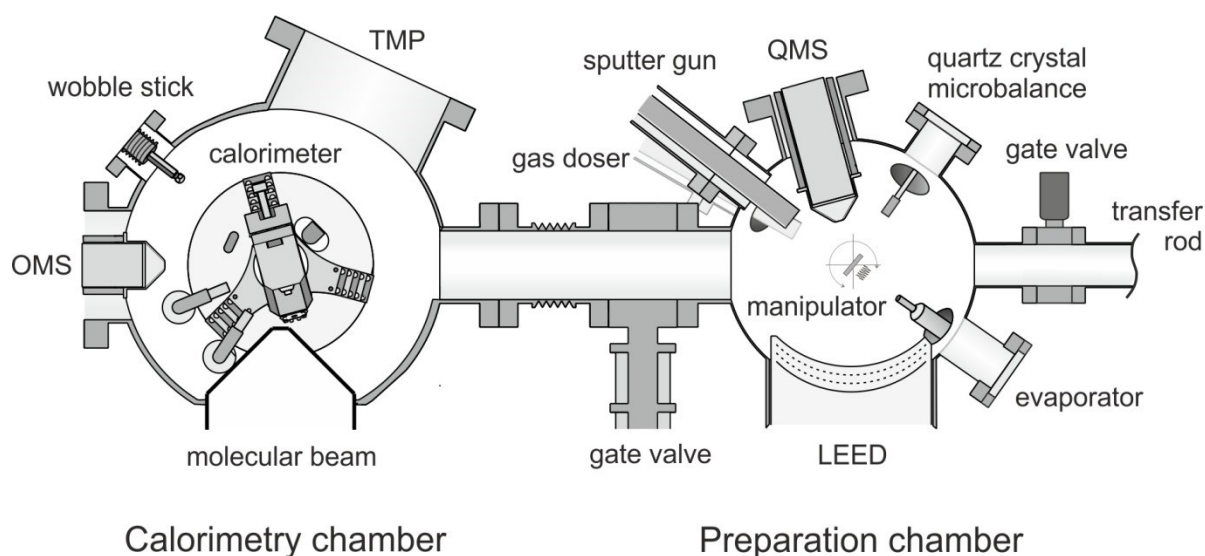


Figure 2.12 Schematic representation of the SCAC apparatus. A part of the components such as the second metal evaporator, the second gas doser, the window for reflectivity measurements and optical pyrometer, etc., are not seen in this top view diagram.

Preparation chamber

Sample cleaning facilities include a sputter gun (Omicron, ISE-10) and a W filament for radiative and electron bombardment heating. As thermocouple mounting is not possible for a 1 μm crystal, temperature measurements are done remotely with an infrared pyrometer (Sensortherm, MP25). Pt samples are usually cleaned with repeated cycles of argon sputtering and UHV annealing, while annealing in oxygen is additionally employed to remove carbon residuals (when deal with organic deposits) and to facilitate iron segregation (when deal with oxide films). Argon sputtering is carried out with 10 mA discharge current and ion energy of 1keV. The target current achieved is typically 4-5 μA , and single treatment usually takes 20-40 min. UHV annealing is performed at 1200 K for 5 min and, if necessary, is followed by 5 min oxidation in 10^{-6} mbar O_2 atmosphere at 1000 K. High temperature heating is achieved by electron bombardment to the backside of the thin sample at bias voltage of 800 V.

Low energy electron diffraction (LEED) (SPECS, ErLEED) is usually employed to evaluate the surface cleanliness. In fact, LEED is a surface

sensitive technique which allows for determining surface periodicity. PVD Pt samples are always free of bulk impurities, therefore the surface is supposed to be clean as soon as the right LEED pattern is observed. Despite there is also an Auger electron spectrometer (AES) (combined with LEED) available, it is rarely applied to ultrathin samples because of the risk of damage by a high energy electron beam. LEED is operated at the filament current of 1.50 A and the screen voltage of 5.5 kV.

Organic compounds (e.g. chiral modifiers) are deposited onto the sample surface through a home-made differentially pumped gas doser. It is mounted on a translational stage and is equipped with a hand-driven shutter located at the end of the dosing tube. The sample can be positioned directly in front of the shutter at a distance as short as 1 cm. The doser is connected to the gas supply system, and its backing pressure can be controlled with a capacitance manometer (MKS, Baratron 122). Prior to deposition, the gas doser is saturated with a vapor of interest for ca. 20 min, and the sample cleanliness is recovered by flash heating to 700 K.

Iron oxides are prepared with the help of an electron beam evaporator (Focus, EFM 3) which has an integrated shutter and a flux monitor measuring an ion current. It is water-cooled and normally requires 10 min warming to produce a stable evaporant beam. For the iron evaporation, the filament current and acceleration voltage are typically set to 2 A and 800-850 V, respectively. Since some part of the evaporated material is ionized, during deposition the sample is held at the same potential as the Fe rod in order to avoid ion acceleration and corresponding defects formation in the surface. Before every iron deposition cycle, the sample surface is flashed to 700 K in order to remove residual adsorbates.

Calibration of the evaporator flux is done by a quartz crystal microbalance (QCM) (Sigma Instruments), and this information is very crucial for SCAC studies. Indeed, the amount of energy absorbed upon laser irradiation during the calorimeter calibration is essentially determined by the sample reflectivity. For the iron oxide substrates, the reflectivity was shown to strongly depend on a film thickness.^[149] In practice, systematic calorimetry measurements are possible only if oxide films are ensured to be

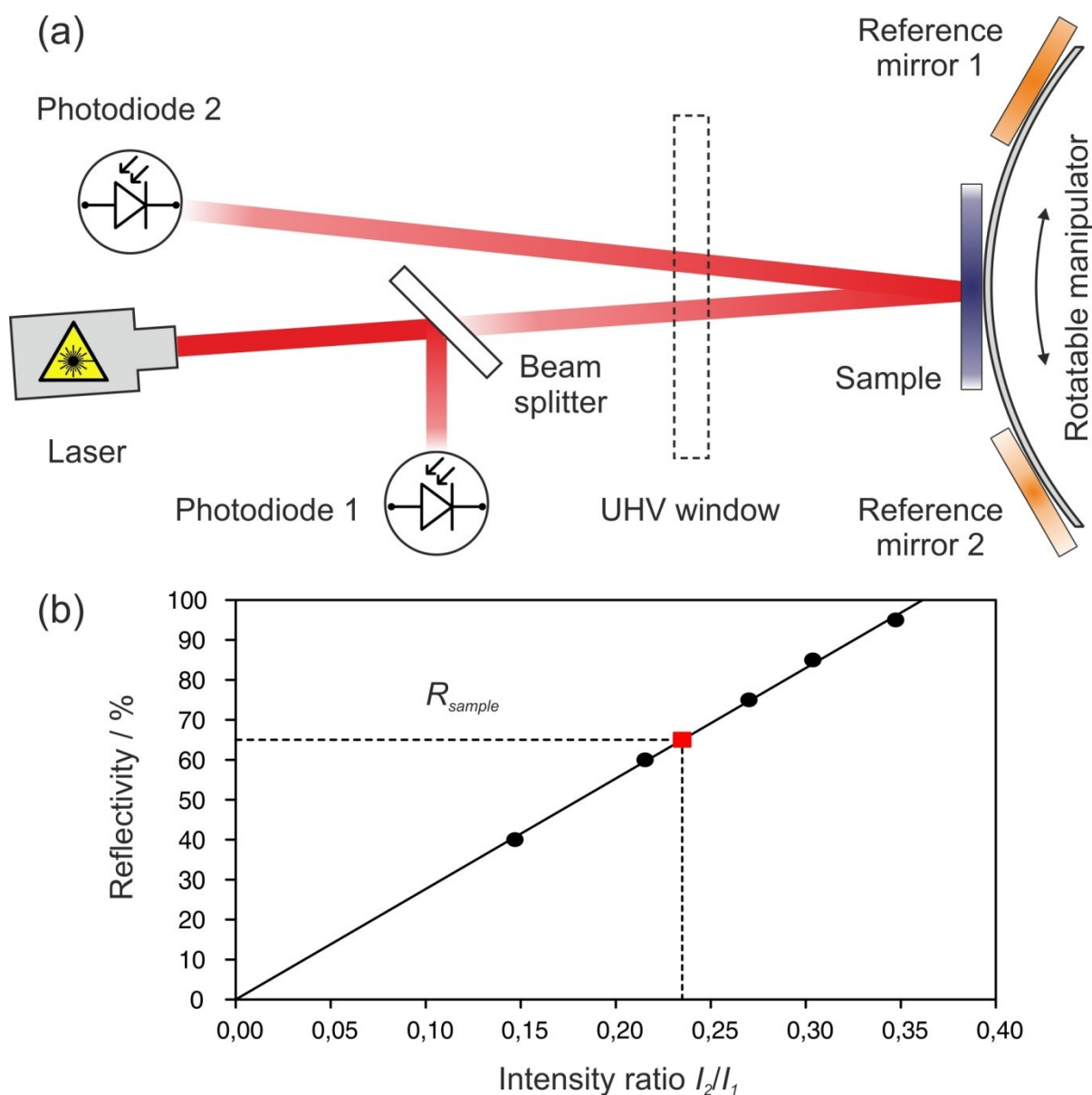


Figure 2.13 *In situ reflectivity measurements. a) Schematic view of the experimental setup. The laser and the photodiodes are placed outside the UHV chamber, reference mirrors are mounted on the sample manipulator. b) Example of a reflectivity calibration plot. The black circles are data obtained with five reference mirrors, while the red square corresponds to the sample.*

grown at the same deposition rate. Thus, QCM provides an external reference for the evaporator flux monitor. The evaporator is initially tuned to have a certain Fe flux as measured by QCM, ordinarily 1 \AA min^{-1} . In the course of the film growth, the evaporator settings are adjusted in such a way that the corresponding value of the ion current is kept constant. This is

mainly achieved by regulating the bias voltage and advancing the evaporant rod.

When a new preparation recipe is adapted, e.g. for a novel oxide film, reflectivity of a substrate is inherently unknown and has to be quantitatively determined. In the preparation chamber, a special procedure is implemented for *in situ* reflectivity measurements. It is not an absolute method but rather based on the comparison with externally defined reference points. A principal experimental scheme is depicted in Figure 2.13a. A light beam from a He-Ne laser (Lasos, 632.8nm, 2mW, cw) is split into two parts, one of which is introduced into the chamber. The laser is positioned in the geometry allowing its beam to reach the sample surface and the reflected light to exit the chamber through the same window. Intensity of the outgoing beam is measured by a photodiode (Silicon Sensor, PS100-2) and can be correlated with that of the second part of the originally divided laser beam. The ratio I_2/I_1 is thus a function of the sample reflectivity. However, the measured quantity carries no information about the absolute value, because the light penetrates twice a thick borosilicate window and part of it is inevitably scattered and/or absorbed. To obtain an absolute number, the same measurements are done with reference mirrors of well-defined reflectivity which are put inside the UHV chamber.

Figure 2.13b shows an example of the *in situ* reflectivity determination. Specifically, five dielectric mirrors (LayerTec) mounted on a so-called mirror revolver are first used to plot a calibration curve $R(I_2/I_1)$. Then, a I_2/I_1 value is measured for a sample of interest – a $\text{Fe}_3\text{O}_4(100)$ film grown on Pt(100) support (Fe nominal coverage 60 Å – 30 Å for the buffer layer and 30 Å for the oxide). The calibration plot yields the sample reflectivity to be ~65% which agrees with the reflectivity trend obtained previously for $\text{Fe}_3\text{O}_4(111)$ films of varied thickness.^[149] Reflectivity measurements are repeated several times on newly prepared samples in order to account possible variations in the film thickness caused by fluctuations of the evaporator flux during the oxide growth. Since ultrathin crystals are not ideally flat and often have microscopic holes, thick samples (~2 mm) are normally used for reflectivity studies.

Calorimetry chamber

As opposed to TPD and EAI, SCAC enables surface reactions to be studied at isothermal conditions. In order to exploit this advantage and probe adsorption energetics as a function of temperature, one has to be able to vary the calorimeter temperature. It is particularly important to carry out adsorption experiments at cryogenic temperatures because under UHV conditions many adsorbates are not stable at room temperature. Therefore, the calorimetry chamber is designed in such a way that the experimental temperature can be accurately controlled in the range 100-300 K.

The SCAC detector and the sample housing depicted in Figure 2.9 are located on a massive piece of copper (~2 kg mass) which serves as a thermal reservoir. In the bottom part of the chamber, the copper block is thermally coupled with a small reservoir having two exits outside the UHV chamber. The reservoir is directly connected to a liquid nitrogen tank (Apollo®100) through a thermally isolated hose. When liquid nitrogen (or cold N₂ vapor) passes the reservoir, the copper block is cooled down as well. In principle, the liquid nitrogen cooling can be balanced with the heating by the ambient, so that the calorimeter temperature can be stabilized at any desired temperature from 300 K down to ca. 100 K.

Figure 2.14 illustrates principles of the SCAC temperature regulation. Dosing of liquid nitrogen is performed via an electromagnetic valve governed by an advanced temperature controller (Eurotherm, 3508). In fact, heat transfer, i.e. thermal equilibration, between the copper block and the cryogenic reservoir is rather slow, because they are linked by means of thin copper wires, and the former has a considerably larger mass. Consequently, two process variables and two control circles are used to stabilize the calorimeter temperature. One thermocouple (TC1) is mounted directly on the sample housing and monitors the actual operation temperature. Another thermocouple (TC2) is placed outside the UHV chamber and approximately indicates the temperature of the cooling reservoir. Two control loops (L1 and L2) are coupled in such a way that opening of the liquid nitrogen valve (E/M valve) depends not only on how the real calorimeter temperature (TC1) is far from the desired one (SP) but also correlates with reservoir temperature

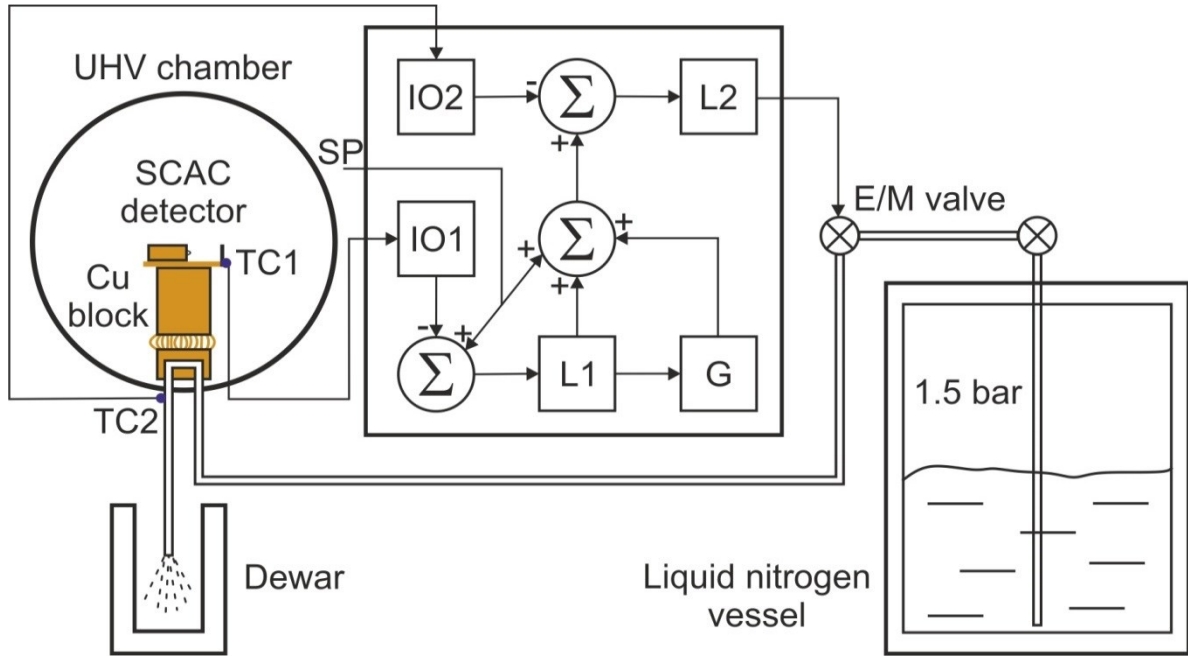


Figure 2.14 SCAC temperature control diagram. TC1 and TC2 are the thermocouples, E/M valve is the electromagnetic valve supplying liquid nitrogen, SP is the input device to set desired SCAC temperature. The input module IO1 measures the calorimeter temperature, while the primary PID controller L1 determines the set point for the secondary PID controller L2. The module G (gradient) accounts for the optimal cooling rate. The input module IO2 measures the reservoir temperature and defines the opening time for the electromagnetic valve.

(TC2). This control scheme prevents calorimeter overcooling and allows the temperature set point to be achieved within 1 K accuracy. Furthermore, there is an option to program the set point temperature to be changing with time according to the following law:

$$T_{SP} = C - B \cdot t$$

where T_{SP} is the working setpoint of the temperature control circle, t is time in hours, B is a time constant equal to 15 K hour⁻¹, and C is an externally defined parameter. One can set such a value of C that enables desired calorimeter temperature to be obtained by a certain period of time. For example, we plan to conduct a SCAC experiment at 150 K and launch the calorimeter cooling in advance. By setting the parameter C to be 375 K, the

calorimeter temperature of 150 K is reached in 15 hours. That allows for saving consumption of liquid nitrogen, when an exhaust emitted by the cooling reservoir is mostly in the gaseous form, i.e. no liquid enters the receiving dewar.

Despite the photodiode and the beam monitor are mounted on the same rotation mechanism as the calorimeter detector, the construction of the damping platform makes them not to be influenced by the cooling system. The beam monitor chamber is a vertically situated tube (490 mm long and 14 mm in diameter) with a 1 mm opening on the top end which can be placed in front of the 4 mm molecular beam aperture. Base pressure in the beam monitor is $4\text{-}5\cdot 10^{-9}$ mbar as measured by its internal ion gauge (Granville-Phillips, 370 Stabil-Ion) located in the bottom part of the stagnation tube. During the beam calibration, the pressure in the beam monitor increases, and its equilibrated value can be related to the incoming flux as following:

$$F = \frac{p}{\sqrt{2\pi mk_B T}}$$

where p and T are the pressure and temperature (300 K) in the stagnation chamber, m is the molecular mass of the probe gas and k_B is the Boltzmann constant.

As mentioned in Section 2.3.2, the molecular beam source is operated in the effusive mode, i.e. at the Knudsen number $Kn \gg 1$:

$$Kn = \frac{\lambda}{L}$$

where λ is the molecular mean free path in the stagnation reservoir and L is the nozzle size. Under such expansion conditions, effusing molecules preserve their initial speed distribution making the overall thermodynamic analysis given above valid. Practically, the gas expansion is done through a 1 mm long glass capillary array (GCA) (Galileo) with a channel diameter of 50 μm , and the beam is further collimated by two differentially pumped stages with 4 mm orifices. The pressure in the beam stagnation stage is regulated by a mass-flow controller (based on components from MKS Instruments). Between 10^{-3} and 10^{-1} mbar, the molecular beam flux produced by the GCA

is directly proportional to the backing pressure, and its typical operation value amounts to $1 \cdot 10^{14} \text{ cm}^{-2} \text{ s}^{-1}$. Prior to adsorption experiments, the molecular beam source is saturated with a gas of interest for 30-60 min until the amount of molecules penetrating the calorimetry chamber (at a closed beam chopper) reaches a constant value. The latter can be monitored with a quadrupole mass-spectrometer (Hiden, HAL 301/3F PIC) which is primarily used for the sticking coefficient measurement.

The molecular beam source is combined with the laser calibration system. Particularly, its second pumping stage is equipped with a UHV window and a retractable prism positioned in 90° internal reflection geometry. Accordingly, a light ray from a He-Ne laser (Linco, 632.8nm, 2mW, cw) can be coupled with the molecular beam path right before the modulating chopper. During the calorimeter calibration, the laser light is attenuated by a set of optical filters, so that a calibration curve can be plotted for a wide range of energy inputs. Absolute laser power is measured by the photodiode (Silicon Sensor, PS95-4) which can be also placed in the sample position.

2.4 Infrared reflection-absorption spectroscopy

2.4.1 Principles

Since SCAC cannot provide any information about chemical nature of the surface species being formed upon adsorption, calorimetry experiments need to be accompanied by additional structural data in order to assign the measured energetics to a certain process. It is generally advisable to study those surface reactions which have been already characterized by other methods, so that one initially knows what species are formed during the experiment. In the present study, SCAC measurements were supported by infrared spectroscopy experiments.

Infrared spectroscopy probes vibrational energy levels of molecules (or a matter in general) and is therefore highly sensitive to the molecular structure. In the harmonic approximation, the frequency of a molecular vibration is given as following:

$$\nu = \frac{1}{2\pi} \cdot \sqrt{\frac{k}{\mu}}$$

where k is a force constant for a chemical bond between two atoms and μ is a reduced mass of the atoms. Due to this relation, many chemical bonds and functional groups, such as, e.g., O-H, N-H, C-H, C=O, appear as structural fingerprints in vibrational spectra of molecules. Infrared spectroscopy is usually done in the transmission mode, when electromagnetic wave passes through the volume of randomly distributed species. The light is absorbed by all infrared active vibrations (with a non-zero dynamic dipole moment), and the amount of absorbed energy follows the linear Beer-Lambert-Bouguer law. Despite, quantitative evaluation of infrared spectra is complicated by dipole-dipole interactions.

In adsorption studies, transmission experiments are less common because most solid substrates are not transparent to infrared radiation, and absolute volume concentration of adsorbates is too low to distinguish their optical absorption from that of the substrate. However, the spectral information can be also obtained by analyzing the light reflected from the

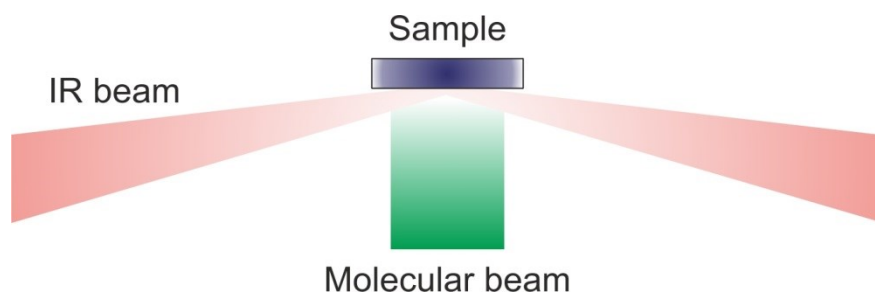


Figure 2.15 *Schematic view of an IRAS experiment combined with molecular beam exposure. An IR beam enters and exits the UHV chamber through compatible KBr windows.*

sample. Infrared Reflection-Absorption Spectroscopy (IRAS or RAIRS) is one of the reflectance techniques which is primarily suitable for flat single crystal samples. In this method, the incident light beam impinges on the sample surface at a small grazing angle, and an absorption spectrum of the surface species is detected as an attenuation of the specularly reflected radiation (Fig. 2.15). Absorption spectroscopy in such external reflection geometry is applicable only to highly-reflective samples, and hence one can study all metallic surfaces and even supported thin oxide films.

Since adsorbed species are spatially constrained, IRAS spectroscopy is subject to additional selection rules. According to the metal surface selection rule, one can detect only those vibrations which are associated with an oscillating dipole moment perpendicular to the surface.^[150] This influences the intensity of the absorption bands observed which becomes strongly dependent on the adsorption geometry and can change significantly with surface coverage. Also, the dipole coupling between different surface species can give rise to such effects as intensity borrowing between two vibrations of a similar frequency. Correspondingly, the intensity of one peak is strongly attenuated, while the other peak becomes very intense. Thus, quantitative interpretation of IRAS data is usually difficult.

2.4.2 IRAS experimental setup

The molecular beam/surface spectroscopy apparatus at the Fritz Haber Institute designed for studying surface chemistry on model catalysts is

described in detail elsewhere.^[151] Briefly, it consists of two chambers separated by a gate valve, and a sample is permanently mounted on a long-travel manipulator. Similarly to the SCAC instrument, the preparation chamber possesses all necessary equipment for sample cleaning and thin films growth, its base pressure is in the mid 10^{-10} mbar range. During the study, sample preparation for IRAS experiments, particularly $\text{Fe}_3\text{O}_4(111)$ films growth, imitated that performed in the SCAC machine. A Pt(111) single crystal sample of ~ 2 mm in thickness is attached from the back side to a ceramic heating plate, and its temperature is monitored by a type K thermocouple spot-welded to the edge. The sample temperature can be stabilized between 120 and 500 K (or higher) by controlling the heating current, while the whole manipulator is cooled by liquid nitrogen. TPD measurements can be also carried out in the preparation chamber with a shielded quadrupole mass-spectrometer (HIDEN Analytical RC PIC).

The measurement chamber is equipped with several molecular beam sources and has base pressure better than $1 \cdot 10^{-10}$ mbar. Two independent effusive beams with similar characteristics as in the SCAC instrument were used in the present work. Beam fluxes can be varied from $\sim 10^{13}$ up to $\sim 6 \cdot 10^{14} \text{ cm}^{-2} \text{ s}^{-1}$, and both sources can work either in a pulsed (minimal duration for an individual pulse is 5 sec) or continuous mode. The beams are crossed in the sample position and cover the entire surface area, so that adsorption of two different compounds can be achieved at the same time. A Fourier transform infrared spectrometer (Bruker, IFS66v/S) is operated with a liquid nitrogen cooled MCT detector and has spectral resolution of 2 cm^{-1} . Before gas exposure, the sample is flashed to 700 K, and background spectra are recorded every time prior the adsorption experiments.

§ 3 Research synopsis

3.1 Adsorption calorimetry on chiral metal surfaces

Chirally-modified metals represent a very promising class of solid enantioselective catalysts for the production of valuable chiral compounds such as drugs and pesticides.^[41] As shown in *Section 2.1*, practical development of this approach requires deeper insights into the nature of interactions between pro-chiral adsorbates and chirally-modified surfaces. There are two main mechanisms of the chiral induction proposed, where chiral modifiers govern stereoselectivity either individually (“one-to-one” model) or collectively (“templating” model).^[57] The one-to-one modifiers form bimolecular complexes with reactant adsorbates and can bestow selectivity even at low concentrations, whereas a certain surface coverage of the templating modifiers is needed to create chiral supramolecular arrays. Nevertheless, both interactions imply a thermodynamic difference in stability of the competing pro-R and pro-S adsorption configurations. Model surface science studies employing chiral adsorbates as a probe can in principle explore all these effects and, as reviewed above, many successful efforts have been already undertaken.^[67, 72, 75, 83, 152] Temperature-programmed desorption (TPD) has been often used to quantify adsorption energetics on chirally-modified surfaces.^[42] However, the disadvantage of TPD is that both modifier and probe species can undergo thermal chemistry during a temperature increase. In this work, SCAC was used to conduct isothermal low-temperature adsorption experiments on chirally-modified metal surfaces.^[153] We examined two model systems which are likely to follow different chirality induction mechanisms. *Section 2.1* provides a detailed overview on the selected chiral modifiers.

Adsorption of propylene oxide (PO) was first studied on R-1-(1-naphthyl)ethylamine (NEA) modified Pt(111) at 110 K. Relative surface coverage of the modifier was varied between 0 and 1. Figure 3.1 demonstrates differential adsorption energy of both PO enantiomers for different modifier coverages. On bare Pt(111), the adsorption energy decreases with coverage from initial 50 ± 1 kJ mol⁻¹ to 42-43 kJ mol⁻¹ at

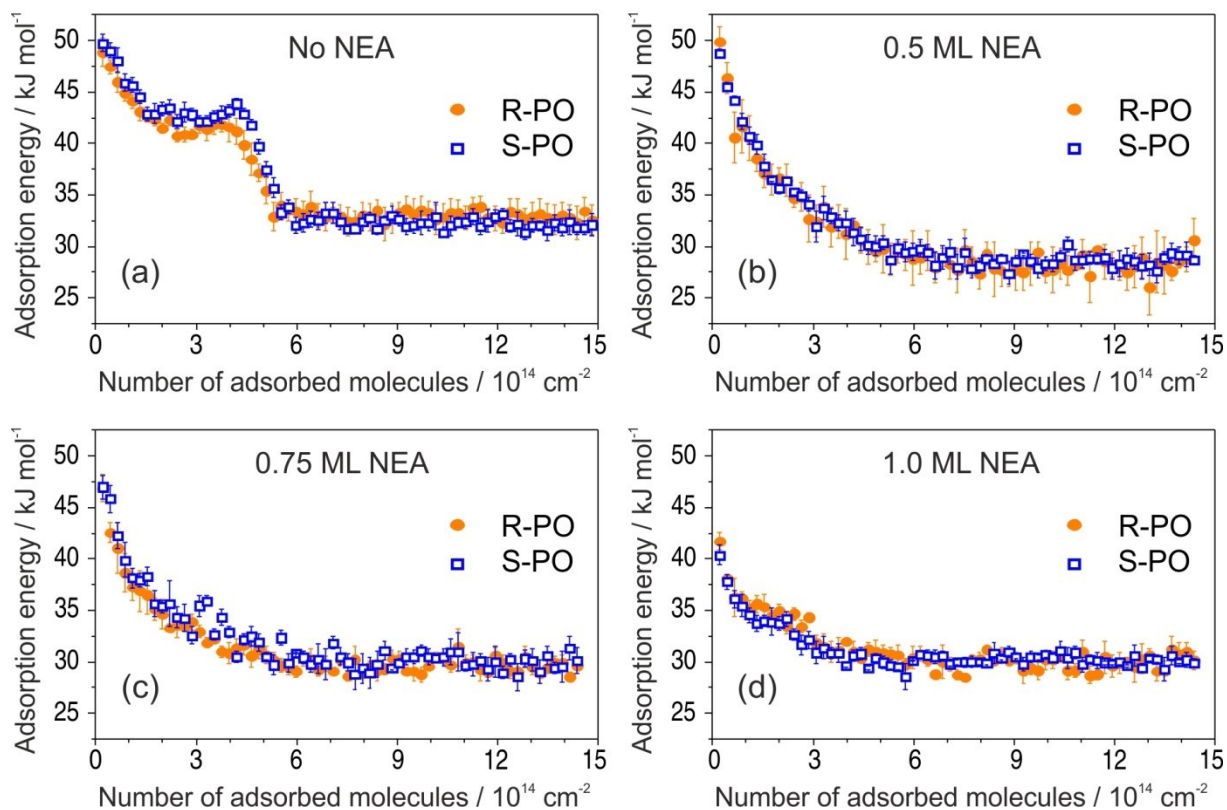


Figure 3.1 Differential adsorption energy of *S*- and *R*-PO enantiomers on *R*-NEA-modified Pt(111). The data points are averages of 3–5 independent measurements; the error bars show the error of the mean.

$1.5 \cdot 10^{14}$ molecules cm^{-2} , stays constant up to $4.1 \cdot 10^{14}$ molecules cm^{-2} and afterwards goes abruptly down to 34 ± 1 kJ mol^{-1} (Fig. 3.1a). This constant value observed at higher PO uptakes corresponds to adsorption in the second and subsequent layers. Thus, the steep between $4.1 \cdot 10^{14}$ and $5.5 \cdot 10^{14}$ molecules cm^{-2} indicates completion of the monolayer and transition to the multilayer regime. In contrast, PO adsorption on NEA-covered surfaces exhibits monotonically decreasing adsorption energy for all modifier coverages (Fig. 3.1b-d). Initial adsorption energy changes from ~ 49 kJ mol^{-1} on 0.5 ML NEA to 41 ± 1 kJ mol^{-1} on the fully covered surface. The constant value of adsorption energy associated with the multilayer always appears at the same PO uptake amounting to $\sim 6 \cdot 10^{14}$ molecules cm^{-2} . Consequently, PO monolayer on the NEA-modified Pt(111) comprises molecules adsorbed both on the metal and on the modifier species, so that their total amount remains

the same as on the pristine surface. For all modified surfaces, the adsorption energy reveals no difference between R- and S-PO enantiomers.

Further, Pt(111) modified by S-2-methylbutanoic acid (MBA) was studied towards interaction with chiral adsorbates. Specifically, surfaces with different MBA amounts corresponding to a relative coverage of 0.4, 0.6, 0.8, and 1.0 ML were similarly characterized by adsorption of R- and S-PO enantiomers. As shown in Figure 3.2, differential adsorption energy on all MBA covered samples resembles that one on bare Pt(111) (Fig. 3.1a) in a sense that there is a characteristic steep present. Although the initial adsorption energy slightly varies between 45 and 47 kJ mol⁻¹, it also decays to 42-43 kJ mol⁻¹ and then rapidly reaches the constant multilayer value of 30-32 kJ mol⁻¹. For different MBA amounts, this transition occurs, however, at different PO uptakes which exhibit a linear dependence on the modifier surface coverage. PO is likely to adsorb preferentially on the free metal sites available between the MBA species, and even at the highest modifier coverage PO uptake is almost a half of that on bare Pt(111). Within experimental error no enantioselectivity is found on MBA-covered surfaces, neither in the adsorption energetics nor in the number of adsorbed probe molecules.

The SCAC data obtained indicate that NEA and MBA chiral modifiers behave on the Pt(111) surface differently. While small amounts of NEA completely change PO adsorption mode compared to that on bare Pt(111), the shape of the adsorption energy curve observed on the metal persists on MBA-modified surfaces. Significant changes of the adsorption energy by NEA indicate a strong influence of the modifier species onto the incoming PO molecules either directly, e.g. via dipole coupling, or indirectly, e.g. by changing the electronic properties of the Pt surface. It is likely that PO adsorbs in the vicinity of NEA which prevents PO islands formation on the still available metal patches. This type of adsorption behavior suggests a specific interaction between PO molecules and surface modifier species which might be indicative of the formation of intermolecular complexes, e.g. 1:1 adducts. In contrast, MBA species seem to have a very weak impact on the underlying substrate and low affinity towards PO molecules. Most likely,

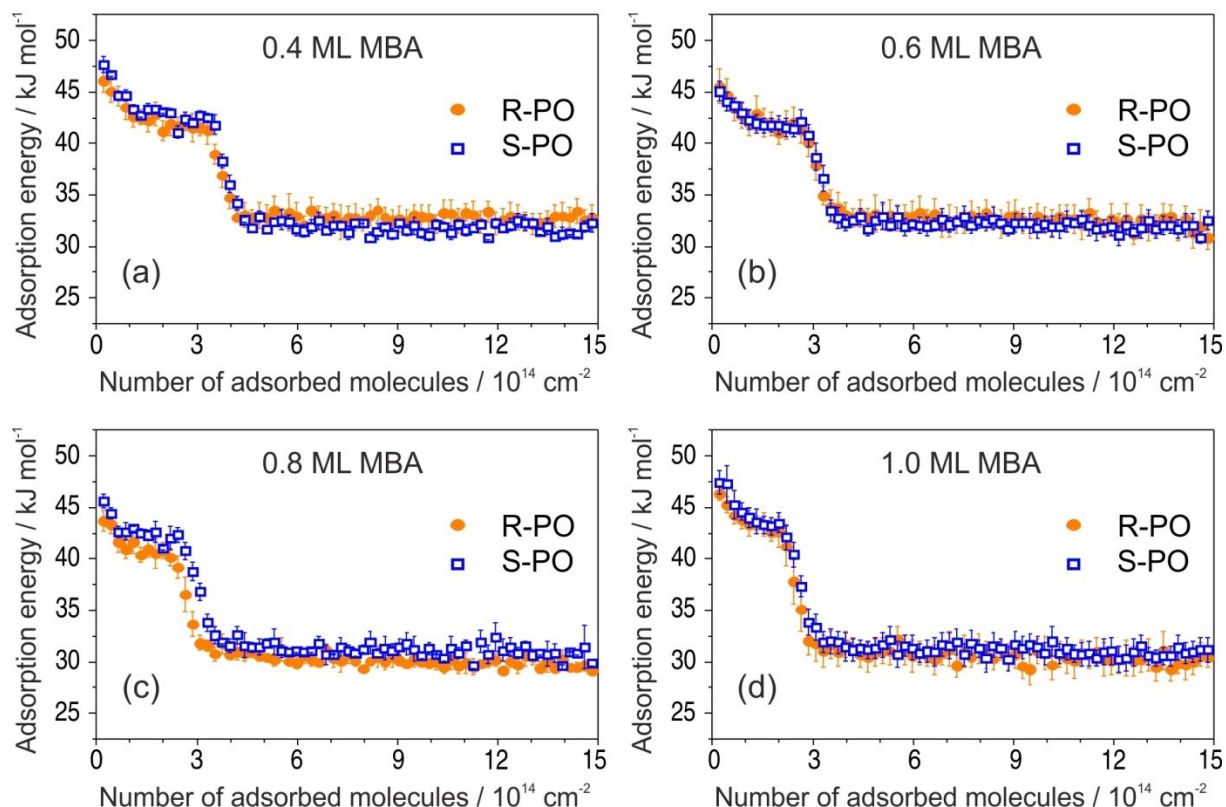


Figure 3.2 Differential adsorption energy of *S*- and *R*-PO enantiomers on *S*-MBA-modified Pt(111). The data points are averages of 3–5 independent measurements; the error bars show the error of the mean.

MBA forms compact patches on Pt(111) and leaves relatively large areas of Pt surface atoms free, at which PO adsorbs in the same way as on the pristine Pt(111) surface. Thus, MBA surface species seem to affect PO adsorption on metal sites only sterically, consistent with the supramolecular model.

Both adsorption systems investigated showed no enantioselective effects either in terms of the adsorption energy or in terms of the absolute PO uptake. On the contrary, the same systems were previously reported to exhibit pronounced stereoselectivity in desorption studies (Section 2.1).^[43, 44] The apparent discrepancy between our SCAC results and the earlier reported data originates most likely from the differences in the applied experimental methods and correspondingly in the physicochemical processes probed. These differences as well as further arguments on the chirality bestowing mechanisms are discussed in detail in Chapter 4.

3.2 Adsorption calorimetry on metal oxide surfaces

Industrial catalytic processes widely employ oxide materials in order to support catalytically active metal nanoparticles or as reactive substrates themselves.^[45] Due to the reasons described in *Section 2.2*, mechanistic understanding of chemical reactions on metal oxide surfaces is rather poor. Particularly, elementary steps for surface chemistry of water on iron oxides, playing an important role in the water-gas shift reaction, are still under debate.^[47] Although the interaction of magnetite with water has been characterized by a number of surface sensitive techniques, it is not clear whether the model of dissociative adsorption is valid.^[48, 142] Indeed, adsorption energies on $\text{Fe}_3\text{O}_4(111)$ derived from TPD and EAI (50 and 65 kJ mol^{-1} respectively) are both rather low and do not match the energetic scale characteristic to strong chemical interactions (order of hundreds kJ mol^{-1}).^[49] There is also no systematic information available allowing for comparison of relative reactivity for different magnetite surfaces. Purely computational studies are not very reliable in this context because they often fail even in predicting equilibrium surface structures. Herein, thin films approach was used to characterize quantitatively interaction of water with the most abundant (111) and (100) surfaces of magnetite. SCAC experiments were accompanied by TPD and IRAS measurements, as well as by externally conducted DFT calculations.

First, adsorption of water was studied on a well-defined $\text{Fe}_3\text{O}_4(111)$ substrate. Differential adsorption energy of D_2O on this surface at 120 K is shown in Figure 3.3a in comparison with that on bare $\text{Pt}(111)$ and on an ultrathin $\text{FeO}(111)$ film. Water is known to physisorb on metallic Pt ^[154, 155] which agrees with the measured initial adsorption energy of $\sim 45 \text{ kJ mol}^{-1}$. Similarly, oxygen-terminated FeO bilayer exhibits the adsorption energy of water typical for physisorption processes which is in fact hardly distinguishable from the adsorption energy in multilayer seen at higher water coverage. In contrast to molecular adsorption on $\text{Pt}(111)$ and $\text{FeO}(111)$, the initial adsorption energy of water on magnetite is almost twice as higher amounting to $87 \pm 1 \text{ kJ mol}^{-1}$. It is even higher at elevated temperatures and reaches near 100 kJ mol^{-1} , as measured at 180, 240, and 300 K (Fig. 3.3b).

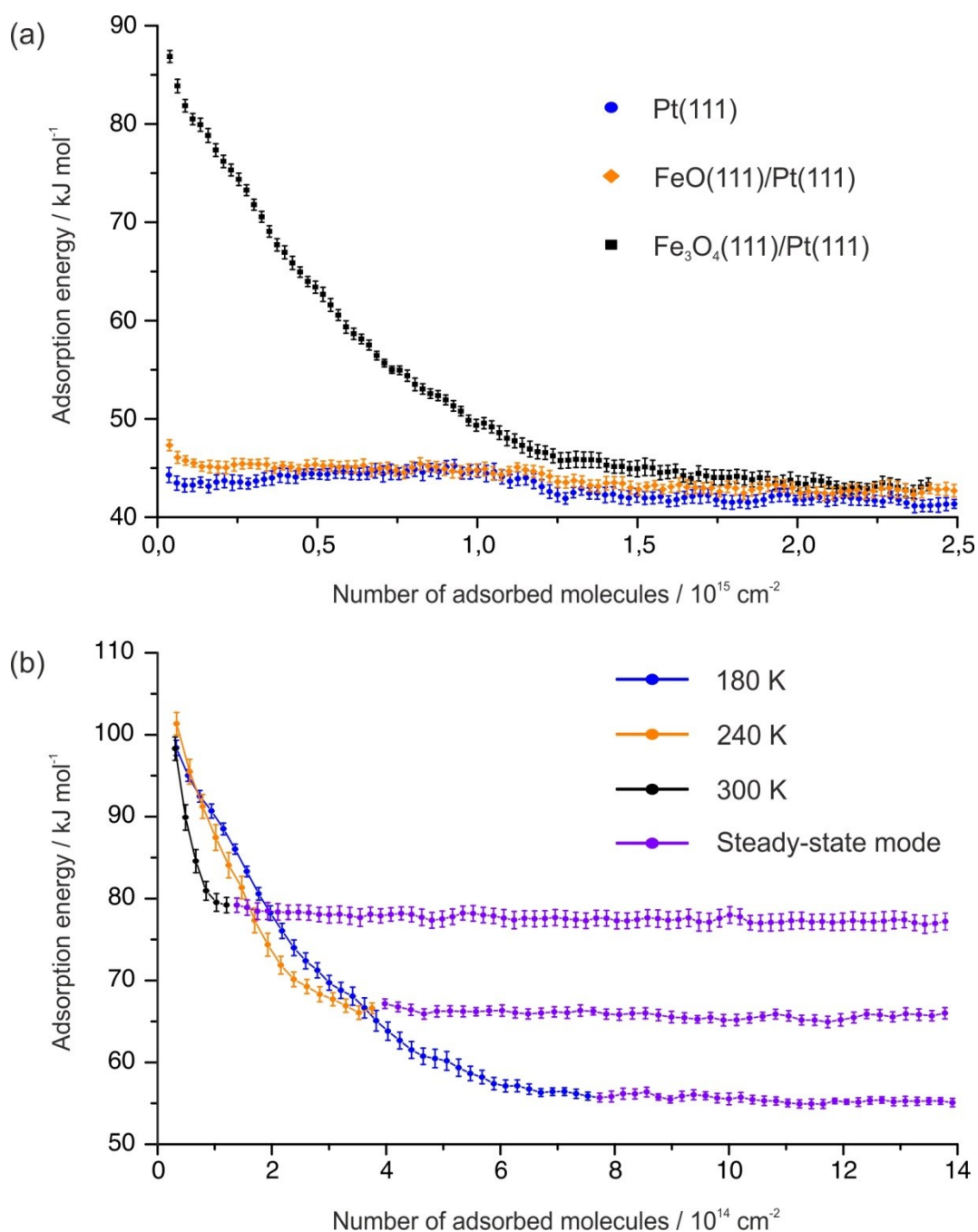


Figure 3.3 a) Differential adsorption energy of D_2O on Pt(111), FeO(111), and Fe₃O₄(111) measured at 120 K. b) Differential adsorption energy of D_2O on Fe₃O₄(111) measured at elevated temperature. The data points are averages of ~ 10 independent measurements; the error bars show the error of the mean.

Such high adsorption energy immediately indicates some chemical transformations which might be consistent with the dissociation mechanism. The difference between 120 K and high temperatures is likely caused by

kinetic hindrance of the surface reaction. The adsorption energy strongly decreases with increasing surface coverage, indicating changes in the electronic structure of the oxide surface. While at 120 K one can see a smooth transition from the monolayer to the multilayer adsorption regime, taking place in the coverage range $1\text{--}1.5\cdot 10^{15}$ molecules cm^{-2} , the situation is different at higher temperatures, where water does not form a multilayer under UHV conditions. At 180, 240, and 300 K adsorption energy was revealed to level off at certain coverages and enter to a steady-state mode depicted by purple bars in Figure 3.3b. As discussed in *Section 2.3*, such a behavior results from adsorption-desorption equilibria and in the present case points to a temperature-dependent saturation surface coverage. Thus, saturation coverages of water on $\text{Fe}_3\text{O}_4(111)$ at 10^{-10} mbar equal to $7.5\cdot 10^{14}$, $3.9\cdot 10^{14}$, and $1.3\cdot 10^{14}$ molecules cm^{-2} as going from 180 to 240 and 300 K, respectively.

Despite the SCAC data clearly show that water reacts with $\text{Fe}_3\text{O}_4(111)$ surface, the obtained value of adsorption energy is substantially higher than those reported in early TPD and EAI studies. In order to verify whether this discrepancy originates from the above described drawbacks of the desorption-based methods, we performed reference TPD and IRAS experiments. TPD traces measured with D_2O and infrared spectra recorded at 120 K reproduce very well all previously reported data which indicates similar structural and chemical properties of the epitaxial $\text{Fe}_3\text{O}_4(111)$ films prepared in different studies. Additionally, vibrational spectra of water on magnetite were for the first time acquired at higher temperatures, so that the adsorption energy measured can be directly correlated with certain surface species formed. Two absorption bands at 2720 and 2695 cm^{-1} are seen in low-coverage IRAS spectra (Fig. 3.4). According to the model of dissociative adsorption proposed before, the two peaks might belong to two types of surface hydroxyl groups: the one originating from a water molecule and the other one formed between a proton and a lattice oxygen atom. However, the two bands are not distinguishable in isotopic exchange experiments, that is, when the surface is alternately exposed to either H_2O or D_2O (Fig. 3.4a). There is simply reversible replacement of the two isotopologue forms

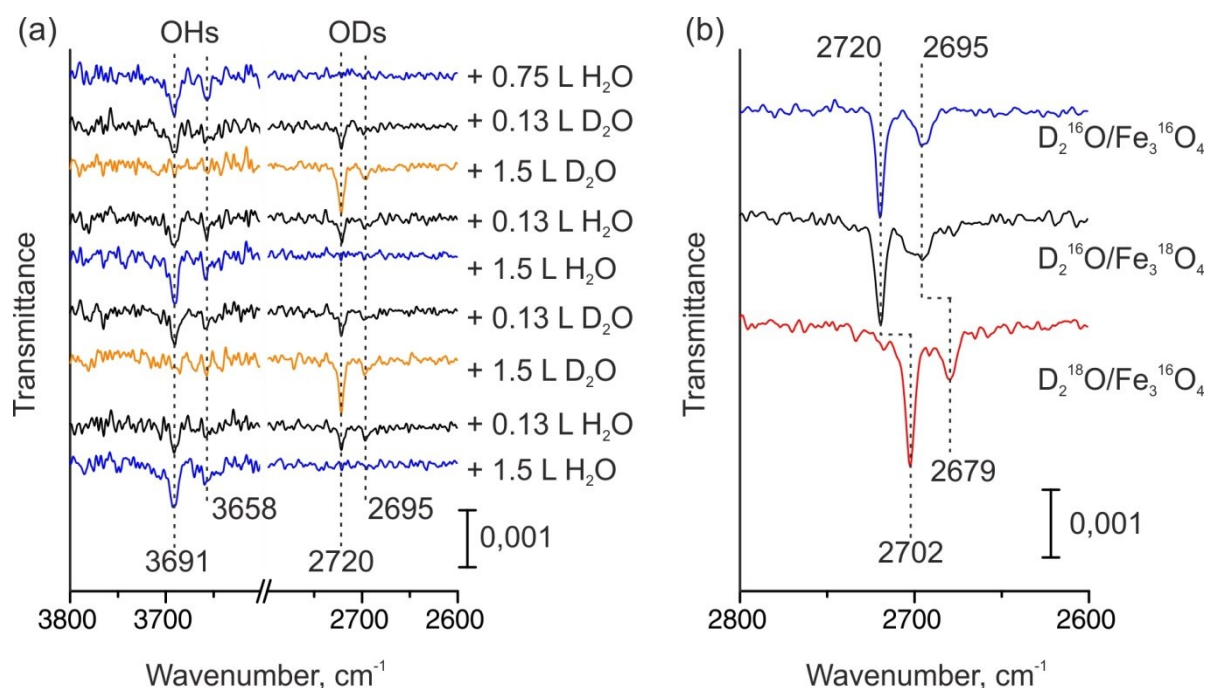


Figure 3.4 a) IRAS spectra in the regions of terminal OH and OD stretching vibrations collected at 300 K after successive exposing the Fe₃O₄(111) sample to the indicated amounts of H₂O and D₂O. b) IRAS spectra of D₂O on Fe₃O₄(111) at 300 upon isotopic labelling with ¹⁸O. The shown spectra were obtained at saturation coverage.

observed, meaning that two oxygen-hydrogen bonds are likely to comprise the same species rather than present individually. As revealed by isotopic labelling experiments, both spectral features exhibit a red shift only upon using doubly labelled water and not on the oxide substrate grown with ¹⁸O (Fig. 3.4b). These data disprove the previously proposed adsorption mechanism, where only one of the two hydroxyls groups contains oxygen from the adsorbing water.

Based on DFT calculations by Joachim Sauer and coworkers (HU Berlin), a new adsorption model was developed, in which both OD bonds observed originate from incoming water molecules. Specifically, the most thermodynamically favorable reaction pathway was found to be the formation of a hydroxyl-water dimer-like complex. These species consist of one water molecule dissociated to two OH groups and one non-dissociated molecule bridging the surface hydroxyl groups by hydrogen bonding. Such

molecular structure agrees with the available experimental results both in terms of adsorption energy and vibrational frequencies. More information on water interaction with $\text{Fe}_3\text{O}_4(111)$, including extensive spectroscopic data and computational details, can be found in *Chapters 5 and 6*.

Finally, adsorption of water was investigated on a $\text{Fe}_3\text{O}_4(100)$ film. Figure 3.5a shows differential adsorption energy of D_2O measured at 120 as compared to the reference $\text{Pt}(100)$ surface. Similar to $\text{Fe}_3\text{O}_4(111)$, initial adsorption energy on the bare oxide is higher than on the metal and amounts to $65 \pm 1 \text{ kJ mol}^{-1}$. Adsorption energy decreases with surface coverage, and starting with $1.5 \cdot 10^{15} \text{ molecules cm}^{-2}$ constant adsorption energy corresponding to the ice condensation is seen. Higher adsorption energy in the sub-monolayer indicates chemical transformations, consistent with the previously reported data on water dissociation. At elevated temperature, saturation water coverages exist, and initial adsorption energy is higher than at 120 K. However, quantitatively adsorption energetics on $\text{Fe}_3\text{O}_4(100)$ is different than on $\text{Fe}_3\text{O}_4(111)$ (Fig. 3.5b). One can see that the initial adsorption energy of water on the two iron oxide surfaces differs by almost 20 kJ mol^{-1} . It means that (111) surface is more reactive than (100). Thus, surface chemistry does strongly depend on which surface plane of the oxide is exposed.

The structure-reactivity relation obtained by SCAC can be interpreted in terms of acid-base properties immanent to ionic compounds. Three types of ions exist in the magnetite crystal structure which can in principle work both as Brønsted base (O^{2-} anions) and Lewis acid (Fe^{2+} and Fe^{3+} cations). Taking into account diversity of possible coordination sites for the topmost surface layers, one can now rationalize different affinity of the two magnetite substrates towards water. As described in *Section 2.2*, the subsurface cation vacancy structure of $\text{Fe}_3\text{O}_4(100)$ exposes iron atoms in octahedral positions having a coordination number 5. On the contrary, the same cations are threefold coordinately unsaturated in the $\text{Fe}_{\text{oct}2}$ termination, which was shown in the present study to be the most stable surface for $\text{Fe}_3\text{O}_4(111)$. One can therefore conclude that the observed behavior of (111) and (100) magnetite surfaces in the reaction with electron-donor species relates to

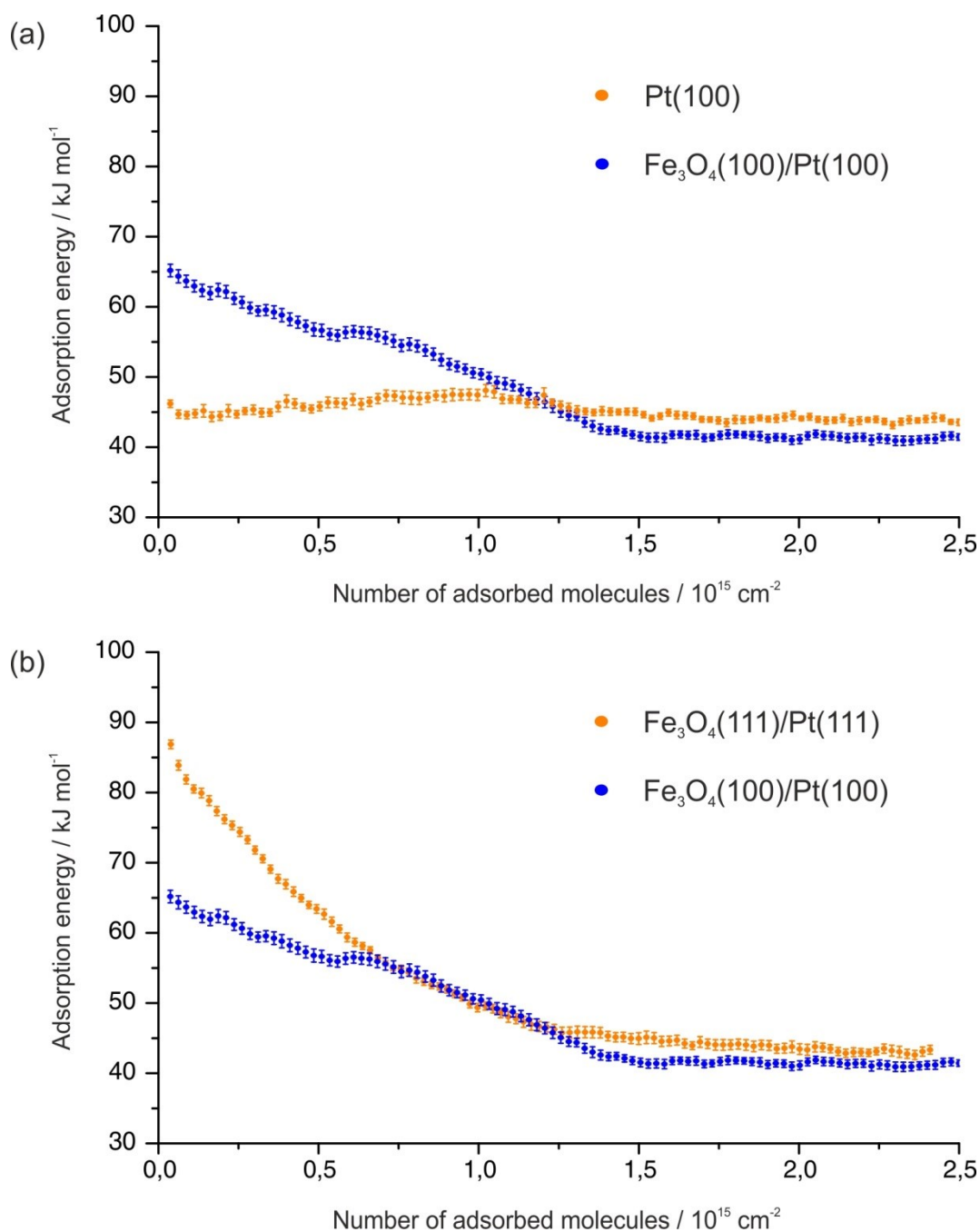


Figure 3.5 a) Differential adsorption energy of D_2O on $\text{Pt}(100)$ and $\text{Fe}_3\text{O}_4(100)$ measured at 120 K. b) Differential adsorption energy of D_2O on $\text{Fe}_3\text{O}_4(111)$ and $\text{Fe}_3\text{O}_4(100)$ measured at 120 K. The data points are averages of ~ 10 independent measurements; the error bars show the error of the mean.

different electrophilicity of their surface iron sites. In other words, $\text{Fe}_3\text{O}_4(111)$ surface has stronger acidic character than $\text{Fe}_3\text{O}_4(100)$. Further considerations on this issue are presented in *Chapter 7*.

§ 4 Chirally-modified metal surfaces: energetics of interaction with chiral molecules[□]

4.1 Abstract

Imparting chirality to non-chiral metal surfaces by adsorption of chiral modifiers is a highly promising route to create effective heterogeneously catalyzed processes for the production of enantiopure pharmaceuticals. One of the major current challenges in heterogeneous chiral catalysis is the fundamental-level understanding of how such chirally-modified surfaces interact with chiral and prochiral molecules to induce their enantioselective transformations. Herein we report the first direct calorimetric measurement of the adsorption energy of chiral molecules onto well-defined chirally-modified surfaces. Two model modifiers 1-(1-naphthyl)ethylamine and 2-methylbutanoic acid were used to impart chirality to Pt(111) and their interaction with propylene oxide was investigated by means of single-crystal adsorption calorimetry. Differential adsorption energies and absolute surface uptakes were obtained for the R- and S-enantiomers of propylene oxide under clean ultrahigh vacuum conditions. Two types of adsorption behavior were observed for different chiral modifiers, pointing to different mechanisms of imparting chirality to metal surfaces. The results are analyzed and discussed in view of previously reported stereoselectivity of adsorption processes.

4.2 Introduction

Production and purification of enantiopure chemicals is a topic of vast practical importance arising from the fact that most biologically important molecules are chiral. Heterogeneous catalysts for enantioselective processes combine the chiral media to induce enantioselectivity into an underlying non-chiral substrate (e.g. metal) with the highly catalytically active metal

[□] The following chapter is reprinted (adapted) from the publication by Petr Dementyev, Matthias Peter, Sergey Adamovsky and Svetlana Schauermann *Phys.Chem.Chem.Phys.*, 2015, 17, 22726

nanoparticles and with this hold great potential to achieve tremendous synergetic effects.^[41] There is a rapidly emerging research field, which focuses on designing chirally-modified catalytic surfaces that have been successfully tested under laboratory conditions and batch reactors.^[156-158] Despite the impressive development in this field in the past years, the mechanistic details of the underlying microscopic processes are still under debate.^[159] In particular, it is not clear how the chiral surface binds the reactant molecules in a specific prochiral configuration that yields only one preferential enantiomer as a product. On the way to obtaining microscopic insights into the enantioselective surface chemistry, in situ spectroscopic characterization of the catalytic reactions has significantly progressed in powdered materials.^[53, 55, 160] Thus, Baiker and coworkers recently showed that hydrogen bonding between the pro-chiral reactant and chiral modifier molecules takes place.^[52] Molecular chirality has also attracted much interest in surface science research, ^[161, 162] where adsorption of chiral molecules on well-defined single-crystal surfaces and their interaction with other adsorbates have been extensively studied using a variety of surface sensitive techniques.^[43, 44, 56, 63, 67, 71, 75, 92, 96, 163-169] A recent review by Gellman, Tysoe and Zaera summarizes the latest report on chiral surface chemistry performed on model single crystalline surfaces.^[42] As one of the major results of these studies, the authors put forward the idea that enantioselectivity arises from the energetic differences in the interaction of two opposite enantiomers with a chiral surface.

Chiral differentiation can be generally accomplished on three types of metal surfaces: (i) intrinsically chiral terminations of higher Miller index surfaces; (ii) surfaces templated by ordered structures of chiral modifiers (this type of chirality is frequently referred to as “supramolecular chirality”) and (iii) the surfaces carrying individual chiral modifiers which form 1:1 complexes with pro-chiral reactant molecules. As shown by Gellman et al., natural chiral surfaces Cu(3,1,17)^{R&S} can efficiently separate racemic mixture of aspartic acid.^[63] In the case of asymmetric surfaces, on which chirality is imposed by supramolecular assemblies of chiral adsorbates, the stereoselective adsorption sites are produced by so called “chiral pockets” in

the ordered chiral overlayers. The interaction of chiral molecules with the chiral pockets in such supramolecular chiral surfaces has been extensively investigated by Tysoe's group.^[76-78, 80, 170] In particular, R- and S-propylene oxides (PO) were adsorbed on Pd(111) chirally modified with R- or S-2-butanol. At specific modifier coverage, significant enhancement (up to a factor of two) of the adsorbed amount of a homochiral enantiomer as compared to the enantiomer of the opposite chirality was detected in temperature-programmed desorption (TPD).^[76, 170] A similar approach has been successfully applied by Zaera et al. to chirally modified Pt(111) surfaces.^[43, 44, 82] Pt(111) modified with 2-methylbutanoic acid was titrated by PO enantiomers and was found to exhibit a 25% higher TPD yield for the homochiral adsorbate, i.e. S-PO desorbing from (S)-2-methylbutanoic acid modified Pt(111). The energetic difference as measured by TPD was estimated to be $\sim 2 \text{ kJ mol}^{-1}$.^[43] Another successful example of a specific enantioselective interaction is Pt(111) modified with 1-(1-naphthyl)ethylamine (NEA), which was found to split the PO desorption trace into two peaks.^[44] For the high temperature desorption trace, the TPD yield of PO in a homochiral adsorbate-modifier pair was found to be higher than for the adsorbate-modifier pair of the opposite chirality by a factor of four. The difference in the PO desorption peak positions was measured to be about 5 K, corresponding to the energy difference of $1\text{--}2 \text{ kJ mol}^{-1}$. Two desorption states of PO were interpreted to be indicative of the formation of 1:1 complexes between the modifier and the probe molecules.

Despite these advances in the understanding of the enantiospecific interaction on chirally-modified surfaces, there is still a lack of detailed quantitative information on the interaction strength within the reactant-modifier pair. In previous studies, only indirect desorption-based methods, such as TPD, were used in order to estimate the interaction energies. However, these methods have a number of serious drawbacks, mainly arising from the fact that they can be correctly applied only for fully reversible processes and that the estimate of the desorption energies relies on some critical assumptions on the details of the desorption process.

Additionally, the adsorbates and/or modifier overlayers can undergo restructuring, be destroyed or decompose due to the increasing temperature.

As a strategy to overcome these problems, we applied for the first time single-crystal adsorption calorimetry (SCAC) based on molecular beam techniques as a direct method allowing the measurement of adsorption energies of chiral molecules onto chirally-modified metal surfaces. This technique enables the direct and very precise measurements of the adsorption energy of gaseous molecules on well-defined surfaces under isothermal conditions and does not rely on any assumptions on the desorption process.^[39, 171] By carrying out the adsorption measurements under low temperature conditions, we can probe the adsorption energetics of very sensitive adsorption systems, such as e.g. chirally-modified surfaces interacting with light hydrocarbons. Additionally, SCAC allows for measuring adsorption energies as a very detailed function of the surface coverage of the adsorbates. The sticking coefficient measurement, which is an integral part of a SCAC experiment, provides an experimental possibility of studying the evolution of the surface coverage, for example, to monitor how adsorbates populate specific surface areas depending on the temperature or the coverage of the chiral modifier.

We investigate two previously characterized model chiral modifiers 1-(1-naphthyl)ethylamine (NEA) and 2-methylbutanoic acid (MBA) supported on Pt(111). The structural formulae of these molecules are shown in Fig. 4.1. As mentioned above, both chirally-modified surfaces were previously reported to exhibit appreciable enantioselectivity in the adsorption of PO enantiomers, both in terms of the adsorption energies and of the amount of the adsorbed PO.^[43, 44] To verify these findings and to obtain accurate adsorption energies using a direct calorimetric measurement, we measured the PO adsorption energies as a detailed function of the PO coverage at a constant modifier coverage. Complementarily, we varied the surface coverages of the chiral modifiers to tune the properties of the chiral surface overlayers and determined the PO adsorption energies on these surfaces.

Two types of adsorption behavior were observed for different chiral modifiers, pointing to different mechanisms of imparting chirality to metal

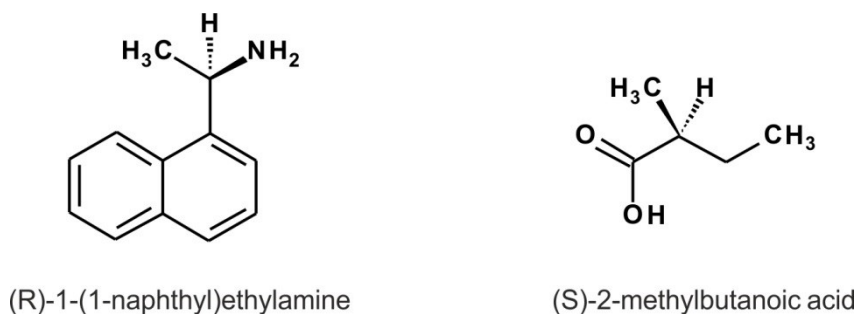


Figure 4.1 *Structural formulae of the chiral modifiers studied.*

surface. The results will be analyzed and discussed in view of previously reported stereoselectivity of the same adsorption processes.

4.3 Experimental section

All experiments were carried out at the Fritz Haber Institute (Berlin, Germany) in an ultrahigh vacuum SCAC apparatus described in detail elsewhere.^[30] An ultrathin Pt(111) single crystal was cleaned by Ar sputtering followed by oxidation and annealing. Deposition of a modifier onto a clean metal surface was performed through a differentially pumped gas-doser. The vapor of R-NEA ($\geq 99\%$ (R)-(+)-1-(1-naphthyl)ethylamine, Sigma-Aldrich) at the saturation pressure was directly introduced into the gas-doser while the NEA flask was kept in an ice-water bath. For dosing S-MBA (98% (S)-(+)-2-methylbutanoic acid, Sigma-Aldrich) a backing pressure of 0.100 mbar was used. The amounts of deposited surface modifiers were controlled by the exposure time. The sample preparation procedure closely resembled the previously described preparation by Zaera and coworkers for better comparison.^[43, 44] NEA was deposited onto a metal surface kept at a temperature below 100 K. MBA was deposited at approximately 100 K followed by annealing at 230 K. The obtained modifier coverage values were calibrated as discussed in the next section.

A freshly prepared sample was transferred from the preparation chamber to the pre-cooled calorimeter. A molecular beam of either R- or S-enantiomers of propylene oxide (99% (R)-(+)-propylene oxide and 99% (S)-(-)-

propylene oxide, Alfa Aesar, Sigma-Aldrich) was formed and cut into 266 ms pulses that were allowed to impinge on the sample surface. The energies were measured by a pyroelectric detector (6- μm thick β -PVDF ribbon from Piezotech), whose response was calibrated by a He-Ne laser of known intensity. For a detailed description of the calorimetric setup, see ref. [30]. Propylene oxide was degassed by freeze-pump-thaw cycles prior to experiments. Sticking probabilities were determined via the King-Wells method^[172] with a mass spectrometer (Hiden Analytical, HAL 301/3F PIC) following the PO fragment at $m/z = 58$.

Further in the text we use the term adsorption energy, which we define as the following:

$$E_{ads} = Q_{cal} - \int_{T_{sample}}^{T_{source}} (C_v + 1/2 R) dT$$

where Q_{cal} is a measured heat release, T_{sample} is the temperature of the calorimeter, T_{source} is the temperature of the molecular beam source (around 300 K), C_v is a constant-volume heat capacity of the probe gas. The integral accounts for gas cooling from the temperature in the molecular beam to the sample temperature. The calculation was performed by using the ideal gas C_v of PO linearly approximated in the temperature range 100–300 K.^[173]

4.4 Results

4.4.1 PO adsorption on R-NEA-modified Pt(111)

NEA is a model chiral modifier, which has an aromatic moiety for binding to a metal surface and an amino group close to the chiral center capable of hydrogen-bonding.^[88] To control the modifier coverage we first calibrated the gas-dosing system. For this, carbon monoxide was used as a probe molecule for free metal sites. CO was dosed onto the surface pre-covered by NEA and sticking coefficient measurements were performed via the King-Wells method^[172] at room temperature. The measured sticking coefficients of carbon monoxide on Pt precovered with various amounts of NEA and the corresponding calibration curve are shown in Fig. 4.2. On bare Pt(111), the

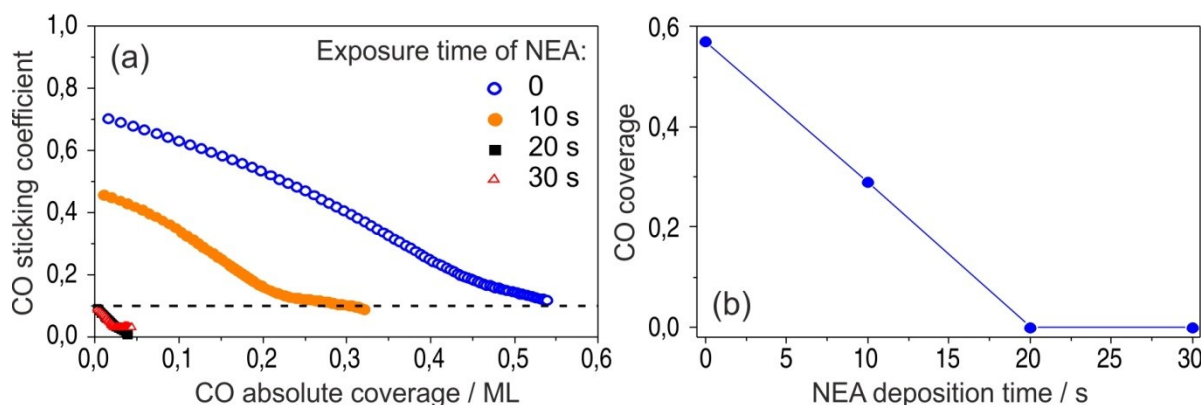


Figure 4.2 (a) Sticking coefficients of CO at 300 K on NEA covered Pt(111) for different NEA deposition times. The CO coverage is given as a ratio of the number of adsorbed CO molecules to the number of Pt surface atoms ($1.5 \cdot 10^{15} \text{ cm}^{-2}$). (b) The CO saturation coverage (in ML) reached on the NEA-covered Pt(111) plotted as a function of the NEA deposition time.

initial sticking coefficient was measured to be ~ 0.7 and then strongly decay with increasing CO surface coverage. This behavior corresponds well to previously reported values of CO sticking coefficients on Pt(111).^[174] Saturation of a monolayer takes place at the CO coverage of ~ 0.55 ML as referred to the absolute amount of Pt atoms $1.5 \cdot 10^{15} \text{ cm}^{-2}$. When NEA is deposited onto the surface, the initial sticking coefficient becomes smaller and fewer CO molecules are required to saturate the monolayer, which implies that NEA molecules do block the CO adsorption sites. When the NEA deposition time exceeds 20 s, the CO sticking coefficient becomes vanishingly small, indicating that NEA adsorbates completely cover the Pt surface and prevent CO adsorption. Note that on the clean Pt(111) substrate the sticking coefficient levels off at approximately 0.1 and does not decrease to 0. This effect is related to the measurement of the sticking coefficient by applying short molecular beam pulses in such adsorption systems, where the saturation coverage strongly depends on the pressure of the adsorbing molecule. For CO adsorption on Pt(111), it was established in previous studies that the CO saturation coverage during the molecular beam is slightly higher than under the UHV conditions.^[30] Therefore, close to saturation the system runs into a quasi-steady state regime, in which

adsorption during the pulse is compensated by desorption between the pulses and the final sticking coefficient remains non-zero. In contrast, on the NEA covered surfaces the final sticking coefficient was found to be zero, indicating that no additional CO can be added to this surface by applying higher CO pressures. The saturation coverage of CO is plotted as a function of the NEA deposition time in Fig. 4.2b. In the following, we define a relative coverage of NEA on Pt(111) Θ_{NEA} as equal to 0 on the pristine surface and equal to 1 when CO adsorption is fully hindered.

Adsorption of S- and R-PO was studied on samples with three different R-NEA coverage values as well as on pristine Pt at 110 K. The sticking probability of PO was determined to be unity at the experimental temperature (110 K) on all investigated surfaces. Fig. 4.3 shows adsorption energy of both the R- and S-enantiomers of PO as a function of the number of adsorbed PO molecules.

On bare Pt(111) (Fig. 4.3a), PO shows non-monotonic changes in the adsorption energy with increasing coverage. The PO adsorption energy starts at 50 ± 1 kJ mol⁻¹ and decreases to the level of 42–43 kJ mol⁻¹ at the coverage of $\sim 1.5 \cdot 10^{14}$ molecules cm⁻², which corresponds to the adsorption of ~ 0.1 PO molecule per one surface Pt atom. Above this coverage, the adsorption energy either goes through a small local maximum (S-PO) or rather remains constant (R-PO) up to the coverage of $4.1 \cdot 10^{14}$ molecules cm⁻², followed by a rapid decrease corresponding to the completion of the monolayer at the value of about $5.5 \cdot 10^{14}$ molecules cm⁻². This number agrees well with the previous IRAS and TPD data indicating that the PO monolayer on Pt(111) saturates after 1.6–2 L exposure corresponding to $4.2\text{--}5.3 \cdot 10^{14}$ molecules cm⁻².^[82] Starting from the coverage of $\sim 5.5 \cdot 10^{14}$ molecules cm⁻², a constant adsorption energy of 34 ± 1 kJ mol⁻¹ was observed, which is related to PO adsorption in the second and subsequent layers. Almost no differences in PO adsorption on pristine Pt(111) surfaces were observed for both stereoisomers.

For NEA-covered surfaces, the adsorption behavior of both PO enantiomers strongly changes exhibiting adsorption energy monotonically decreasing (with the decay greater than linear) to constant energy values

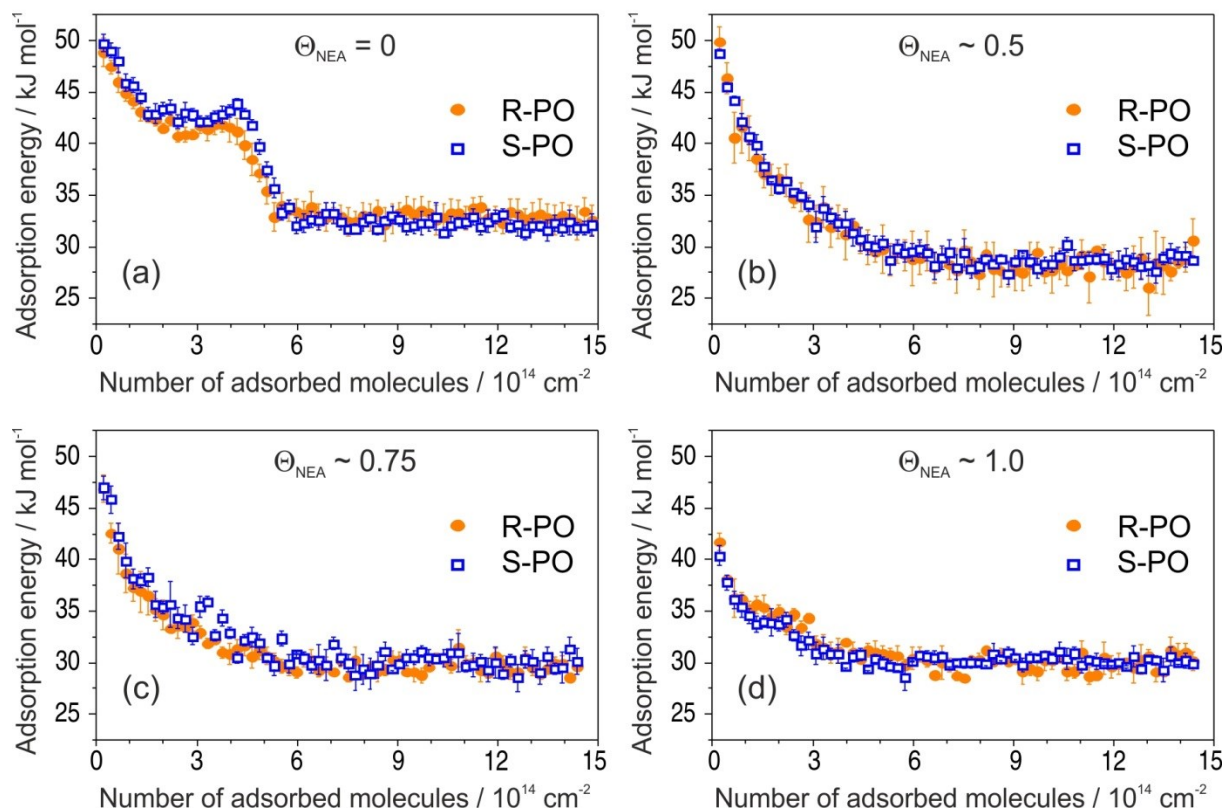


Figure 4.3 Adsorption energy of S- and R-PO as a function of the number of adsorbed molecules on: (a) bare Pt(111); as well as R-NEA-covered Pt(111) with the R-NEA relative coverage of (b) 0.5; (c) 0.75; (d) 1. The data points are averages of 3–5 independent measurements; the error bars show the error of the mean.

varying between 28 and 30 kJ mol⁻¹. Note that even for the smallest NEA coverage the plateau-like character of the adsorption curves, as observed on pristine Pt(111), completely vanishes. One can also clearly see that for all modifier coverage, PO multilayer condensation in the second layer starts at approximately the same PO uptake of $\sim 6 \cdot 10^{14}$ molecules cm⁻², which is also true for bare Pt. This observation indicates that the complete PO monolayer on the NEA-modified surfaces contains not only PO molecules adsorbed on the metal but also those adsorbed on-top of NEA modifier and their total amount remains similar for all modifier coverages. Note that the adsorption energy of PO in the second layer is not very sensitive to the presence of NEA on the underlying surface.

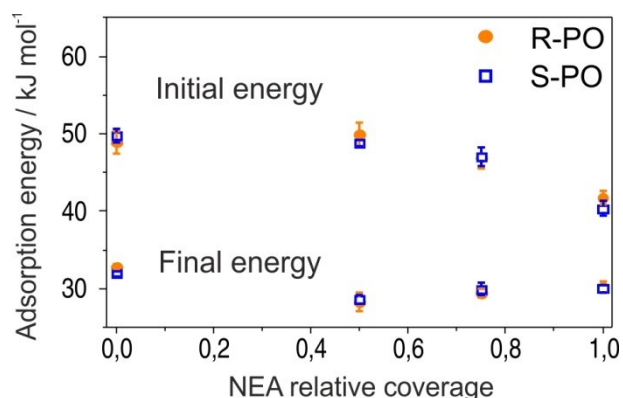


Figure 4.4 Initial and final adsorption energies of S- and R-PO plotted as a function of the NEA relative coverage. The initial adsorption energy is shown in the upper part, while the final adsorption energy is plotted in the lower part of the graph.

The initial adsorption energies corresponding to the first PO pulses and the final energy values are plotted in Fig. 4.4 as a function of the NEA coverage. For both stereoisomers, the initial adsorption energy decreases upon going from bare Pt(111) to 1 ML NEA/Pt(111). Note that the adsorption energy of PO on 1 ML NEA is still higher than that on PO ice. This observation suggests a stronger interaction between PO and NEA than PO and PO ice. Within experimental error no difference between adsorption energies of different stereoisomers of PO on R-NEA was observed. The final energy on the surfaces partially covered with the modifier was found to be somewhat lower than those on bare and fully covered surfaces. These differences might be related either to our experimental accuracy or to the fact the PO adsorbed in the second and a few next layers might be still sensitive to the particular structure of the underlying substrate.

4.4.2 PO adsorption on S-MBA-modified Pt(111)

The second model system investigated in this study is Pt(111) modified by S-MBA. This chiral modifier was previously shown to produce the carboxylate species upon thermal treatment.^[43, 77] In contrast to NEA, the chiral center of MBA does not possess the ability to form hydrogen bonds. Instead, it is

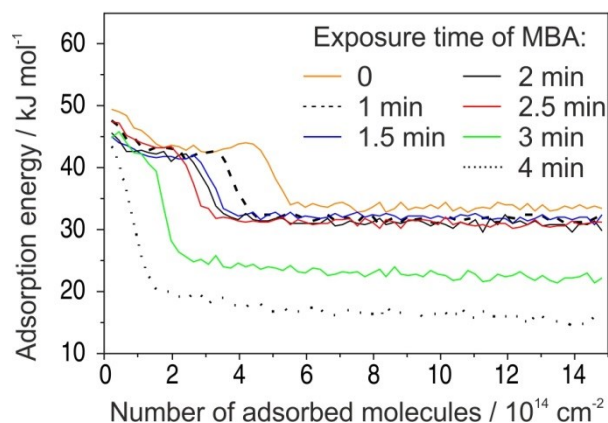


Figure 4.5 Adsorption energy of S-PO at 120 K on MBA covered Pt(111) for different MBA deposition times.

hypothesized that the adsorbed MBA molecules form supramolecular structures with a long-range order.^[43] This overlayer can be considered as a proxy for a templating-type of chirality induction.

It was well-established in previous IRAS studies that MBA partly dehydrogenates on Pt(111) at 230 K to form 2-methylbutanoate species and further decomposes and partly desorbs above this temperature.^[43] These surface processes prevent the precise calibration of the deposited MBA amounts by measuring the CO sticking coefficient as described above for the case of NEA. In the following, we will report the amount of deposited MBA in terms of the deposition time and give some consideration to the absolute MBA coverage achieved in our deposition procedure. The bare Pt(111) was exposed to MBA at gradually increased exposure times and heated to 230 K to produce 2-methylbutanoate species. Adsorption of S- and R-PO was measured at 120 K, the corresponding adsorption energies are plotted in Fig. 4.5 as a function of the number of adsorbed PO molecules for different amounts of the surface modifier. Up to the deposition time of about 2.5 minutes, the energy curves were found to be very similar in shape to the ones obtained in the case of PO adsorption experiments on pristine Pt(111), exhibiting a plateau or a small maximum followed by a sharp decrease of the adsorption energy to ~ 32 kJ mol⁻¹. This behavior is dramatically different for the deposition times above 2.5 minutes: the adsorption energy decreases

continuously with increasing PO coverage and the finally reached energy level lies well below 32 kJ mol⁻¹. These observations can be rationalized if one assumes that the saturation of one monolayer of MBA occurs at the deposition time close to approximately 2.5 minutes. In the scope of this assumption, the similar form of the adsorption curves below the modifier exposure of 2.5 minutes corresponds to the situation where PO adsorbs on the free metal surface between the modifier molecules and exhibits the same adsorption behavior as on the pristine Pt surface. The change of the PO adsorption behavior above 2.5 minutes MBA exposure can be most likely attributed to the onset of formation of a second and further MBA layers so that almost no free metal surface is exposed and PO adsorbs on top of that layer very weakly. Following this argument, we assume that a monolayer of MBA is reached after about 2.5 minutes exposure and use a term of relative modifier coverage with $\Theta_{\text{MBA}}=0$ on pristine metal and $\Theta_{\text{MBA}}=1$ after 2.5 minutes exposure.

Fig. 4.6 shows adsorption energies of both PO enantiomers as a function of PO coverage for four different modifier amounts. The adsorption energy on bare Pt was found to be almost the same as that displayed in Fig. 4.3a. For all investigated MBA coverage, the initial adsorption energy of both S- and R-PO lies between 45 and 47 kJ mol⁻¹ and decays to 30–32 kJ mol⁻¹ in the multilayer regime. The PO adsorption behavior on MBA-covered Pt(111) drastically differs from that one on the NEA modified Pt surface. For all MBA modifier coverage, the adsorption energy is not strictly monotonically decaying (see Fig. 4.6 b–d) but follows the pattern observed on the bare Pt(111) surface, i.e. it exhibits a clear plateau-like region followed by a fast decay to a constant level of 31±1 kJ mol⁻¹. As discussed above, we attribute the earlier stages of PO adsorption to adsorption on the metal, while the drop to the constant final value is related to PO adsorption in the second and the following layers.

It is interesting to note that the presence of the MBA surface modifier almost does not change the shape of the measured curves and only the transition to the multilayer adsorption occurs at lower PO exposures in the presence of higher MBA amounts. This behavior suggests a very weak

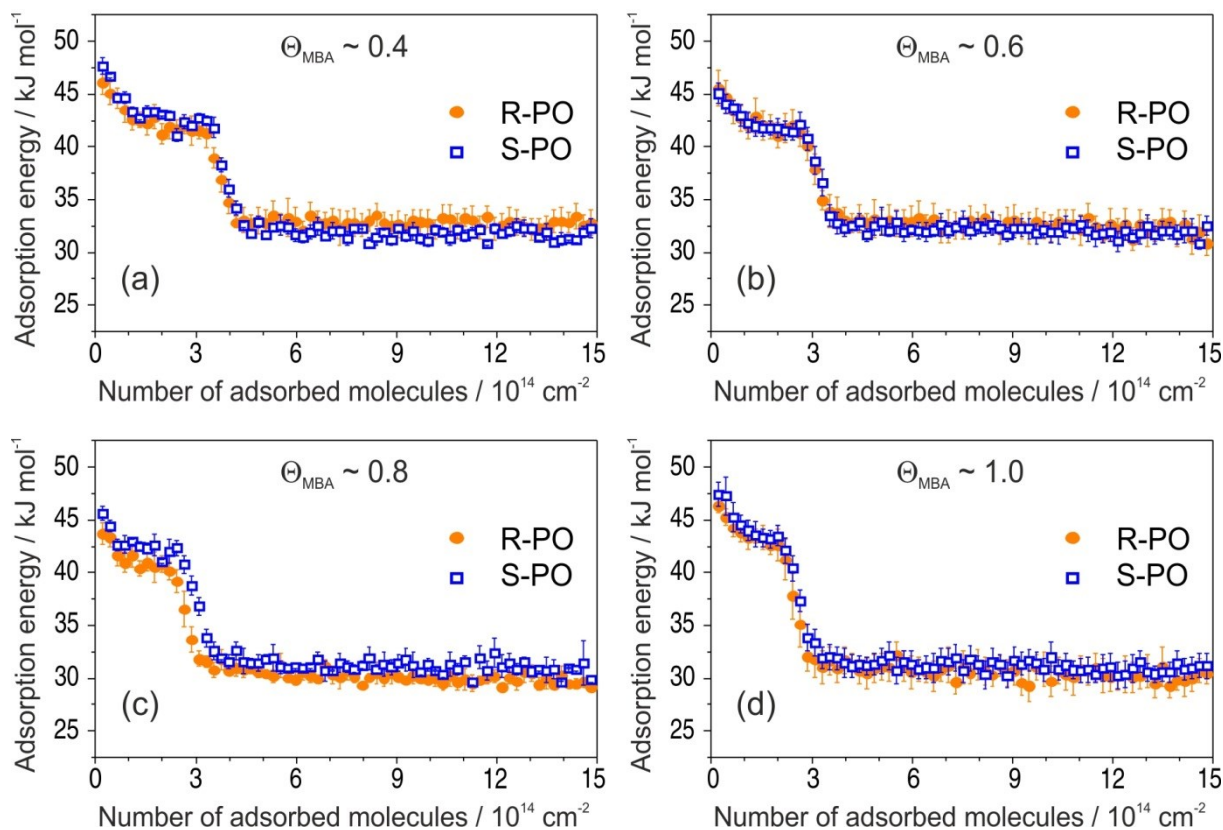


Figure 4.6 Adsorption energy of S- and R-PO as a function of the number of adsorbed molecules at 120 K on MBA-covered Pt(111) with the MBA relative coverage of: (a) 0.4; (b) 0.6; (c) 0.8; (d) 1. The data points are averages of 3–4 independent measurements. The error bars show the error of the mean.

interaction between the PO molecules and the chiral surface modifier, which is unable to noticeably change the energetic situation on the Pt surface if present in submonolayer amounts. Most likely, PO adsorbs on the free metal patches available between the MBA molecules without showing any strong intermolecular interaction with the chiral surface modifier.

This situation is in very sharp contrast to the case of NEA that was found to change the PO adsorption behavior even if present in the smallest surface concentrations. For comparison, we refer the reader to Fig. 4.3b, showing a strong change of the adsorption curve from a plateau-like on the bare Pt(111) to a strictly monotonically decaying when the smallest amount of NEA was deposited.

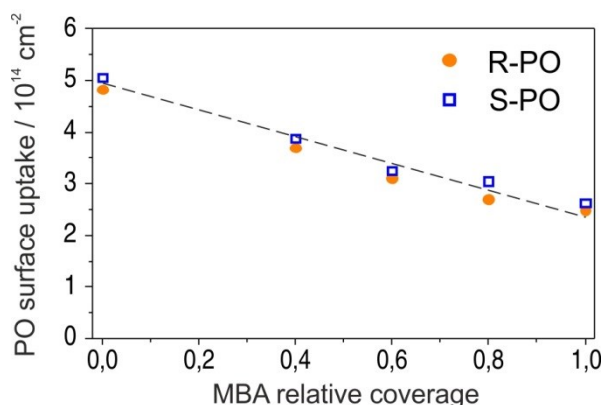


Figure 4.7 The number of PO molecules (S- and R-) adsorbed on one PO monolayer plotted as a function of the MBA relative coverage.

The initial and final adsorption energies were found to be approximately the same for all investigated surfaces. Only subtle differences in energy between the two enantiomers were observed for the intermediate PO coverage on 0.8 ML S-MBA/Pt(111) that might be indicative of a specific stereoselective interaction. Also the amounts of the adsorbed PO before the onset of the multilayer regime appear to be nearly identical for the two different enantiomers. In order to make a strict quantitative comparison of the amounts of PO adsorbed in one monolayer on different chirally-modified surfaces, we treated the experimental data as following: the intermediate regions of the adsorption curves were best fitted by the Boltzmann function, and as a measure of the transition from sub-monolayer to multilayer PO adsorption the inflection points were taken. The results of this evaluation are presented in Fig. 4.7 showing the S- and R-PO uptake onto the metal surface (the PO coverage at the inflection point) as a function of the deposited MBA amount. One can see the PO uptake onto the metal decreases almost linearly with the increasing MBA coverage. When the modifier coverage is close to a monolayer, PO uptake is still almost half of that on bare platinum. This observation suggests that a monolayer of MBA forms an extended supramolecular structure, which leaves enough free metal space to accommodate large quantities of PO. Most likely, this metal pockets are too

small for the modifier molecules themselves but large enough for the small probe molecules such as PO.

4.5 Discussion

Based on the results obtained for both investigated chiral surface modifiers – NEA and MBA – it can be concluded that they show very different surface-modifying effects. Already the smallest sub-monolayer amounts of NEA very strongly change the adsorption behavior of both S- and R-PO on Pt(111) from a plateau-type adsorption discussed above to a strictly monotonic decrease of PO binding energy with increasing PO coverage. In contrast, on the surfaces modified with MBA, PO exhibits the same plateau-type of adsorption behavior as on the clean Pt(111) surface. The increasing amount of MBA results solely in a decreasing adsorption capacity of the surface toward PO adsorption, i.e. in smaller absolute amounts of PO accumulated in a monolayer, but does not affect the shape of the adsorption curve.

Strong changes of the adsorption energy by NEA suggest a significant influence of the modifier molecules onto the incoming PO either directly, e.g. through dipole coupling or ensemble effects, or indirectly, e.g. through changing the electronic properties of the Pt surface. It is important to note that the PO binding energy on the pristine Pt(111) ($\sim 50 \pm 1$ kJ mol⁻¹) at the lowest PO coverage is comparable to that on the NEA-modified Pt(111) with the smallest investigated NEA coverage of 0.5 ML (50 ± 1.5 kJ mol⁻¹, see Fig. 4.4). However, despite these vanishingly small differences in the binding energies, the presence of NEA decisively affects the adsorption behavior of PO. These observations can be rationalized as follows. When PO adsorbs on the pristine Pt(111) surface, its binding energy reaches quite quickly the constant level (see the plateau shown in Fig. 4.3a), which occurs most likely due to the formation of PO islands. After some PO nuclei consisting of a few PO molecules are formed on the surface, the following incoming PO molecules would diffuse to the boundary of these nuclei, where they will adsorb with a constant binding energy. In this case, the energy would be constant because all incoming molecules experience a very similar environment, consisting of a saturated PO island on one side and the clean

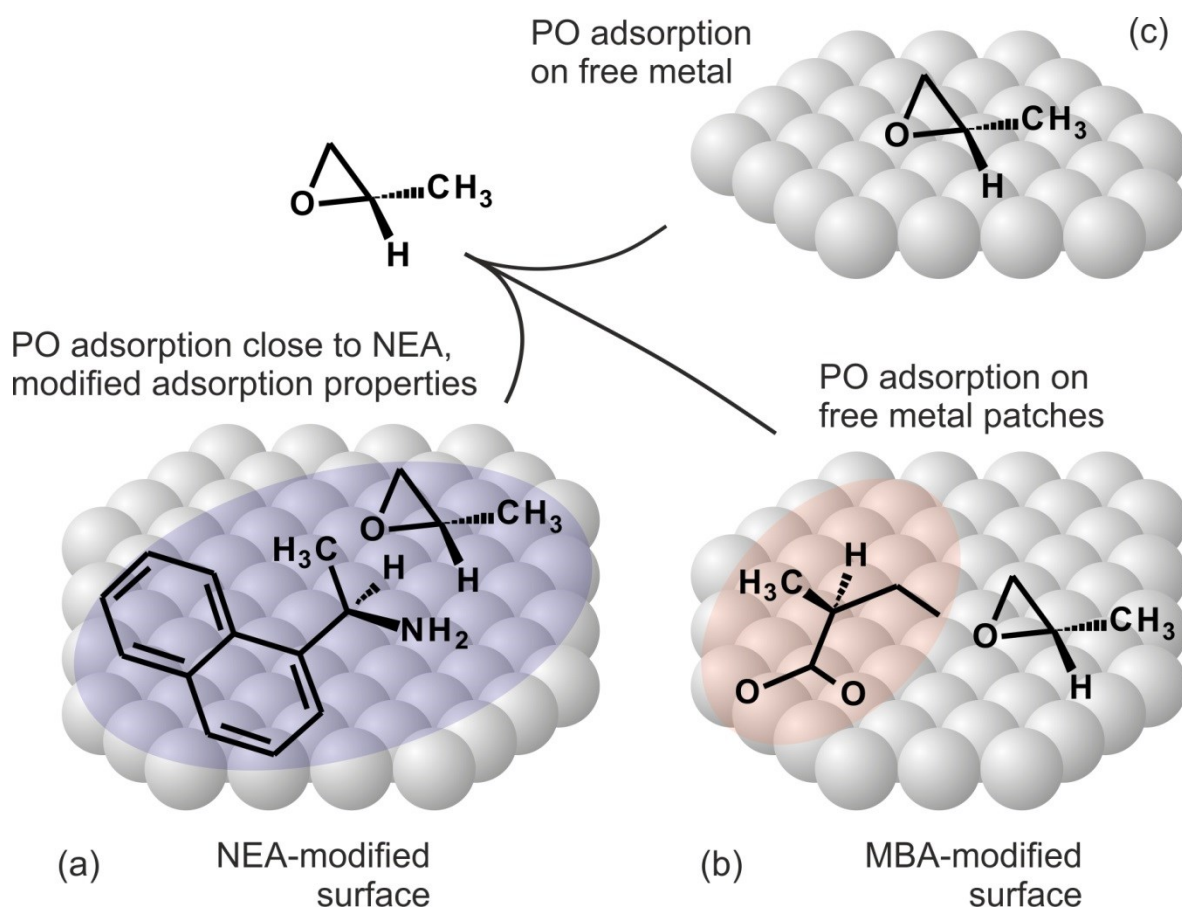


Figure 4.8 Adsorption model. (a) NEA noticeably modifies PO adsorption properties of Pt(111): PO forms a mixed layer with NEA modifier molecules; the PO binding energies are strongly affected. (b) MBA nearly does not affect the adsorption behavior of PO; PO adsorbs preferentially at the free metal patches on Pt(111) similarly to the adsorption on the clean Pt(111) surface (c).

Pt surface on the other side. Only after the PO surface coverage increases to such an extent that neighboring PO islands will start to coalesce, the binding energy of the lastly incoming PO molecules will decrease and approach the value characteristic for PO adsorption in the second layer.

When NEA is present on the surface, this plateau-like behavior vanishes even for the smallest NEA coverage, at which formally 50% of the surface exposes metal atoms. This observation suggests that PO island formation does not occur on this NEA-modified surface. Most likely, there is a preferred adsorption of PO in the vicinity of NEA, which prevents PO island formation on the still available metal patches. This type of adsorption behavior

suggests a preferred interaction between a PO molecule and the adsorbed NEA modifier, which might be indicative of the formation of 1:1 complex between these molecules. This type of enantiospecific interaction for this modifier/probe molecule pair was also put forward in the recent work of Zaera.^[44] However, based on our experimental data, we cannot rule out other possible scenarios. Further microscopic investigations on the structure of these adsorbates are required in order to confirm the formation of the modifier/probe molecule complex.

In contrast to the strong modification of the PO adsorption properties induced by NEA chiral modifiers, MBA almost does not affect the adsorption behavior of PO, neither in terms of energy nor in terms of the plateau-like character of the adsorption curve. Indeed, even at relatively high MBA coverage, the plateau-like character of PO adsorption is preserved, suggesting that PO preferentially adsorbs on the free metal patches still available on the MBA-modified surface. This observation suggests a relatively weak affinity of PO to MBA surface species. Interestingly enough, even at relatively high MBA coverages PO adsorption is not affected by the presence of MBA. This effect can be rationalized based on the assumption that adsorbed MBA forms compact patches on Pt(111) and leaves relatively large areas of Pt surface atoms free, at which PO adsorbs in the same way as on the free Pt(111) surface. These observations point to a rather low strength of interaction between the PO and MBA and inability of MBA to strongly modify the adsorption behavior of PO. In Fig. 4.8 shows a model capturing the main points of this discussion.

In the present study, both adsorption systems investigated by SCAC showed no enantioselective effects within our experimental accuracy either in terms of the adsorption energy or in terms of the absolute PO uptake. On the contrary, the same systems were previously reported to exhibit pronounced enantioselectivity in desorption studies: larger uptakes in homochiral probe-modifier pairs were reported with the enantiomeric ratios amounting to 2.3 and 1.24 for NEA and MBA, respectively.^[43, 44] The apparent discrepancy between our results and the reported data originates most likely from the differences in the applied experimental methods and

correspondingly in the underlying physicochemical processes. In a SCAC experiment, a direct adsorption process was investigated by measuring the adsorption energies. In addition, the absolute amounts of the adsorbed PO molecules were determined via sticking coefficient measurements. Both processes were addressed under isothermal and non-reactive adsorption conditions. The adsorption temperatures applied in this study (110–120 K) were too low to induce any further chemical transformation of PO on the chirally modified surface, so that only the adsorption process was probed. In contrast, in the above discussed experimental studies reporting enantiospecific effects the opposite process was probed – desorption of PO at elevated temperatures from chirally modified surfaces – by employing temperature programmed desorption. A number of accompanying surface processes can occur upon heating that might impart enantioselectivity to a surface process. For example, upon heating the surface modifier and/or the probe molecules and/or the modifier – probe molecule pair can decompose or undergo other structural transformations. These processes can in principle depend on the particular geometric orientation of the adsorbates with respect to the chiral modifier. Alternatively, the adsorbate and/or modifier overlayers can undergo thermal restructuring giving the adsorbates a possibility to find an energetically more favorable site for desorption (i.e. exhibiting lower activation barrier for desorption) prior to the onset of desorption. Indeed, as pointed out by Zaera and coworkers,^[43, 44] the TPD yield of PO, firstly, does not change much in the whole range of MBA surface coverage and, secondly, shows a pronounced deviation from the monotonic decay depending on NEA coverage. Both effects seem to be inconsistent with a simple co-adsorption mechanism and might be indicative of the rearrangement of the modifier species in a desorption process.

In the very general case, the desorption process might be a very complex surface reaction consisting of a number of elementary steps, e.g. competing desorption, decomposition and diffusion to a different surface site, from where it may desorb with a lower desorption barrier. In principle, each of these elementary and competing steps might induce enantioselectivity into the overall desorption process. Therefore caution is required when referring

the differences observed in a desorption experiment to the adsorption process. Both of the chiral modifiers investigated in this study show no greater adsorption capacity in homochiral modifier–adsorbate pairs as compared to heterochiral pairs as directly determined via sticking coefficient measurements. These observations are in sharp contrast to previous studies based on temperature programmed desorption reporting large variation in the amount of desorbing adsorbates for the particular chirality of the modifier and PO. Further atomistic level investigations on the observed differences between the adsorption and the desorption processes might shed some light on this problem.

4.6 Conclusions

Adsorption of S- and R-PO enantiomers onto pristine and chirally modified Pt(111) surfaces was investigated under isothermal conditions in a combined study including the direct calorimetric measurement of adsorption energies by single crystal adsorption calorimetry (SCAC) as well as measurements of sticking coefficients for determining the absolute amounts of adsorbed molecules. As chiral modifiers, NEA and MBA were employed. These chiral modifiers were chosen as potential proxies for two different mechanisms of imparting chirality to achiral metal surfaces: a templating mechanism (MBA) based on the formation of chiral overlayers and a docking mechanism (NEA) based on the formation of 1:1 complexes between the chiral modifier and the adsorbate molecules. Detailed quantitative information on adsorption energies as a function of PO coverage and the content of chiral modifiers was obtained for the first time using a direct calorimetric method for the measurement of adsorption energies on well-defined surfaces. On a pristine Pt(111) surface, S- and R-PO were found to adsorb with an initial adsorption energy of 50 ± 1 kJ mol⁻¹ and to exhibit a very specific adsorption behavior characterized by the presence of a plateau/small peak at a PO coverage lying in the range between 4 and $5 \cdot 10^{14}$ molecules cm⁻². This specific plateau-like behavior might be explained by PO island formation. In the presence of 0.5 ML of NEA, the initial PO adsorption energy of both enantiomers does not change but the dependence of the adsorption energy on the PO coverage

changes dramatically. NEA adsorbates result in the complete elimination of a plateau region in the adsorption curve and induce a strictly monotonic decrease of the PO binding energy with growing PO coverage. This observation suggests a high affinity of incoming PO molecules to adsorbed NEA, probably due to a strong attractive intermolecular interaction, which might be consistent with the formation of a 1:1 docking complex. In contrast to NEA, the interaction of S- and R-PO with the MBA-modified surfaces was found to be very similar to PO adsorption on the clean metal. Particularly, the specific plateau-like dependency of the adsorption energy on the PO coverage was observed to be preserved even at relatively high MBA coverage. PO appears to have a very low affinity for the co-adsorbed MBA and to prefer adsorption on the still available free metal sites/patches of free metal. With this, the MBA surface species seem to be rather incapable of strong intermolecular bonding with PO, at least at low PO coverages, and appear to only sterically affect adsorption on metal sites.

No significant difference was found in the adsorption of two different enantiomers of PO on both chirally-modified surfaces, either in terms of the adsorption energy or in terms of the absolute amount of PO being able to adsorb on the chiral surface of the same vs. the opposite chirality. With this, our findings turned out to be in sharp contrast to several literature studies reporting different adsorption energies and different adsorption capacities of chiral surfaces for adsorbates of different chirality. We attribute the observed discrepancy to the differences in the methodologies applied in the present and in the earlier studies: while direct methods of measurement of adsorption energies (SCAC) and the amounts of adsorbed PO (sticking coefficient measurement) were applied in this study, earlier studies were based on the investigation of the desorption processes from chirally-modified surfaces induced by heating. We discuss the possible reasons for this discrepancy.

§ 5 Water interaction with iron oxides[□]

5.1 Abstract

We present a mechanistic study on the interaction of water with a well-defined model $\text{Fe}_3\text{O}_4(111)$ surface that was investigated by a combination of direct calorimetric measurements of adsorption energies, infrared vibrational spectroscopy, and calculations based on density functional theory (DFT). We show that the adsorption energy of water (101 kJ mol^{-1}) is considerably higher than all previously reported values obtained by indirect desorption-based methods. By employing ^{18}O -labeled water molecules and an Fe_3O_4 substrate, we proved that the generally accepted simple model of water dissociation to form two individual OH groups per water molecule is not correct. DFT calculations suggest formation of a dimer, which consists of one water molecule dissociated into two OH groups and another non-dissociated water molecule creating a thermodynamically very stable dimer-like complex.

5.2 Introduction

Materials based on iron oxides are of crucial importance for many technological and environmental applications.^[175] Under natural humid conditions, they are exposed to water, which strongly affects their structure and reactivity in surface chemical processes.^[16, 120] Despite of the vast importance of the water/iron oxide(s) interaction, the atomistic-level understanding of this system is rather limited, mostly due to the fact that it has been commonly addressed by methods, such as for example, temperature programmed desorption (TPD) or photoelectron spectroscopy (PES), which are based on assumptions in order to extract information on adsorption energies and molecular speciation. Interaction of water with different types of oxides was previously investigated at the atomistic level on

[□] The following chapter is reprinted (adapted) from the publication by Petr Dementyev, Karl-Heinz Dostert, Francisco Ivars-Barcelo, Casey P. O'Brien, Francesca Mirabella, Svetlana Schauermaier, Xiaoke Li, Joachim Paier, Joachim Sauer, and Hans-Joachim Freund

Angew. Chem. Int. Ed., 2015, 54, 13942

model surfaces of TiO_2 ,^[100, 172, 176-178] ZnO ,^[179, 180] Fe_3O_4 ,^[48, 50, 146] Fe_2O_3 ,^[181] RuO_2 ,^[182] and some others. Despite the large amount of available data, mainly obtained by imaging techniques, the reliable spectroscopic identification of surface species formed on these oxides is rare and relates mostly to very high water coverages;^[180, 183] nearly no spectroscopic information is present on the initial stages of water interaction with oxides.

Particularly for magnetite (Fe_3O_4), there is a limited knowledge on the nature of the surface species formed upon water adsorption and dissociation. Even though infrared vibrational spectroscopy of adsorbed water on well-defined model Fe_3O_4 surfaces provides some evidences for the formation of hydroxyl groups, the spectra are rather complex^[48] and not fully understood. Specifically, it is not clear if the simplest model which suggests the formation of two individual hydroxyl groups upon dissociation of one water molecule^[48, 172] – usually discussed in the literature – is valid.

Previous TPD studies suggest a very low binding energy of water on Fe_3O_4 (ca. 65 kJ mol⁻¹),^[16, 48, 49] that is, close to adsorption energies typical of molecular adsorption on chemically inert surfaces (50 kJ mol⁻¹). This observation cannot be rationalized on the common chemical grounds as water is known to dissociate on Fe_3O_4 and form hydroxyl groups, as clearly evidenced by the corresponding spectroscopic signatures.^[48, 50, 141, 143] This apparent contradiction arises most likely from the limited applicability of TPD to complex dissociative processes and from the need for a kinetic modeling of the desorption process. A strategy to overcome these limitations is the direct calorimetric measurement of adsorption energies under isothermal conditions.^[27, 30]

Here, we report the first direct calorimetric measurement of the water interaction strength with a well-defined model $\text{Fe}_3\text{O}_4(111)$ surface grown on $\text{Pt}(111)$ under ultrahigh vacuum (UHV) conditions. So far $\text{Fe}_3\text{O}_4(111)$ has been studied to a lesser extent compared to the (100) surface, but the (111) orientation^[114, 184] is the natural growth facet making it more relevant for applications under ambient conditions. We apply a recently developed UHV single-crystal adsorption calorimeter^[30] (SCAC) based on molecular beam techniques to directly measure water adsorption and dissociation energies as

a very detailed function of surface coverage. Complementary, we employ infrared reflection absorption spectroscopy (IRAS) in combination with molecular beam techniques to identify the nature of the surface species formed upon water adsorption and to find detailed correlations between the structures of the adsorbates and the energies of their formation. We show that the water dissociation energy on $\text{Fe}_3\text{O}_4(111)$ is considerably higher than previously reported, based on indirect desorption methods. By employing IRAS on isotopically labeled water and Fe_3O_4 , we experimentally prove that the generally accepted simple model of water dissociation to form two individual OH groups is not valid. Previous computational studies on water adsorption at the $\text{Fe}_3\text{O}_4(111)$ surface^[146, 185, 186] could not provide a definite atomistic picture of this process. Combining experimental findings with calculations based on density functional theory (DFT), we show that surface OH groups formed upon water dissociation establish a very stable complex with molecular water. Conversely, formation of two individual spatially separated OH groups could be unambiguously ruled out. Calculated spectroscopic vibrational signatures as well as the formation energy of the corresponding OH–water complex agree with experimental observations.

5.3 Results and discussion

Figure 5.1a shows the differential adsorption energy of water measured at 120 K at three different surfaces – metallic Pt(111) and two thin iron oxide layers $\text{FeO}/\text{Pt}(111)$ and $\text{Fe}_3\text{O}_4(111)/\text{Pt}(111)$ – as a function of the number of adsorbed water molecules. The energy measurement was combined with a sticking coefficient measurement using the King-Wells method,^[187] allowing for a quantitative determination of the absolute number of adsorbed water molecules. On the first two surfaces, the initial adsorption energy amounts to about 47 kJ mol^{-1} and remains nearly constant while water is accumulated and finally forms water ice. Low adsorption energies measured on these surfaces are indicative of a molecular adsorption process. In contrast, the initial adsorption energy of water on the $\text{Fe}_3\text{O}_4/\text{Pt}(111)$ surface reaches 87 kJ mol^{-1} , pointing to a strong chemical interaction, that is, dissociation. The adsorption energy strongly decreases with increasing water

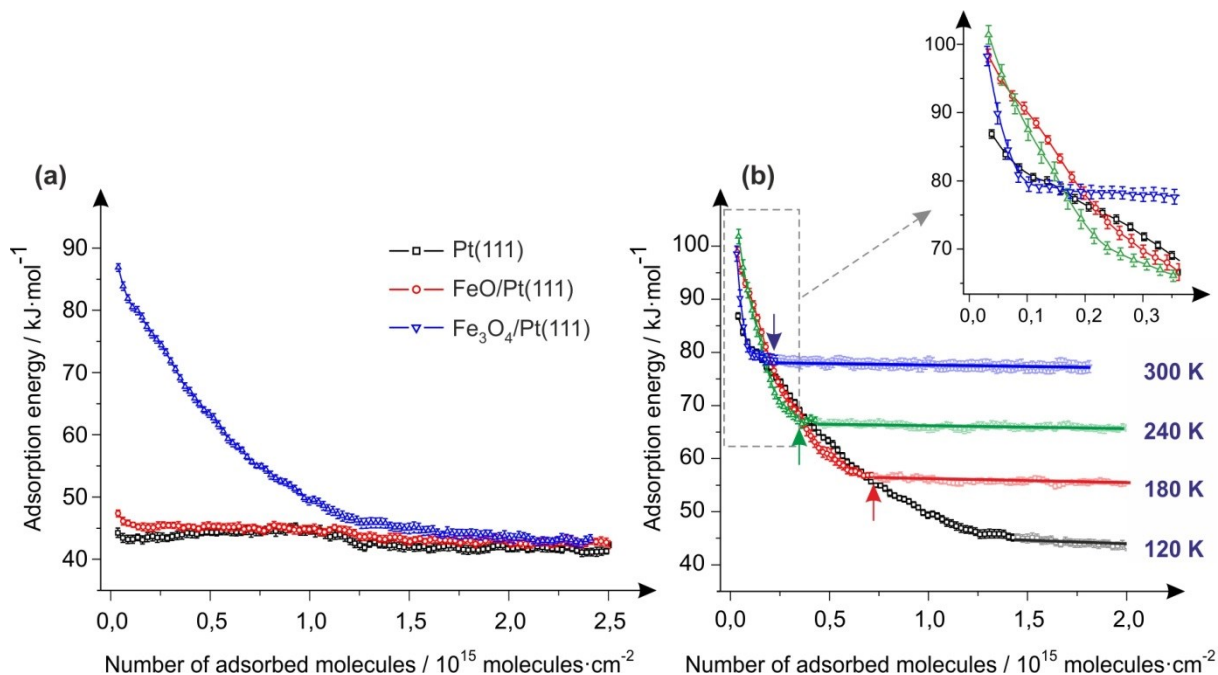


Figure 5.1 a) Differential adsorption energy measured at 120 K plotted as a function of the number of adsorbed D_2O molecules for $Pt(111)$, $FeO(111)/Pt(111)$, and $Fe_3O_4(111)/Pt(111)$. b) Differential adsorption energy of D_2O on $Fe_3O_4(111)/Pt(111)$ as a function of the number of adsorbed D_2O molecules measured at different temperatures.

coverage, which might be due to interatomic repulsion of neighboring adsorbates and/or increasing competition for the electrons of the Fe_3O_4 substrate to participate in the bonding. The measured energy levels off after adsorption of about $1.25 \cdot 10^{15}$ water molecules per square centimeter.

The differential adsorption energies of water interacting with the Fe_3O_4 substrate at four different surface temperatures (120, 180, 240, and 300 K) are shown in Figure 5.1b. While water adsorption at 120 K starts from 87 kJ mol⁻¹ and results in water ice formation at high coverage, the initial adsorption energy at higher temperatures reaches 101 ± 2 kJ mol⁻¹ and no multilayer ice is formed, in agreement with previous observations.^[49] An increase of the initial binding energy from 87 kJ mol⁻¹ at 120 K to 101 kJ mol⁻¹ at temperatures above 180 K is most likely related to a kinetic hindrance of water dissociation at 120 K. Since the initial adsorption energy remains constant for all temperatures above 180 K, this value can be considered as the true thermodynamic value that is not affected by slow

kinetics of water dissociation. Qualitatively, the coverage dependence of the water adsorption energy remains similar to 120 K, however, saturation is reached at lower absolute water coverage. After reaching saturation, the adsorption system runs into a dynamic adsorption–desorption equilibrium (indicated as solid lines at the end of each adsorption curve), in which adsorption during the molecular beam pulse is compensated by desorption between two pulses. Water adsorption energies previously measured by TPD are 30–35 kJ mol⁻¹ lower than the value of 101 kJ mol⁻¹ obtained in the present study,^[142] which we attribute to the kinetic nature of the TPD experiment and the often crude assumptions for pre-exponentials.

To obtain more insight into the atomistic details of water adsorption and dissociation on magnetite surfaces, we monitored the formation of different surface species by IRAS in a temperature range between 120 and 500 K. Figure 5.2a shows the IR spectra obtained after water adsorption on Fe₃O₄(111) at 300 K. The uppermost trace was recorded for D₂O molecules adsorbed on regular Fe₃O₄(111). This spectrum exhibits two distinct vibrational bands at 2720 and 2695 cm⁻¹, which were also observed for all other investigated temperatures at lowest water coverage. At 300 K, there are no coverage-dependent changes of the spectra, except of the absolute intensity of the bands. At lower temperatures new vibrational features appear with increasing coverage. In a previous study, vibrational bands in a similar frequency range were observed at low water coverage and were assigned to two individual hydroxyl groups.^[48] It was suggested that one of the OD groups binds to an iron atom, while D binds to a surface oxygen to form a second type of an OD group. To verify or falsify this assignment, we prepared an isotopically labeled Fe₃¹⁸O₄(111) film and recorded IR spectra of D₂O. The expected shift of the vibrational band at 2695 cm⁻¹ (previously assigned to an OD group involving lattice oxygen) was not observed (blue spectrum in Figure 5.2a). In contrast, when double isotopically labeled water (D₂¹⁸O) was adsorbed on regular Fe₃O₄, both vibrational peaks shifted to lower frequencies by 16 and 18 cm⁻¹, correspondingly (green spectrum in Figure 5.2a). These observations clearly prove that the low-frequency vibrational band (2695 cm⁻¹) does not originate from D adsorption on the

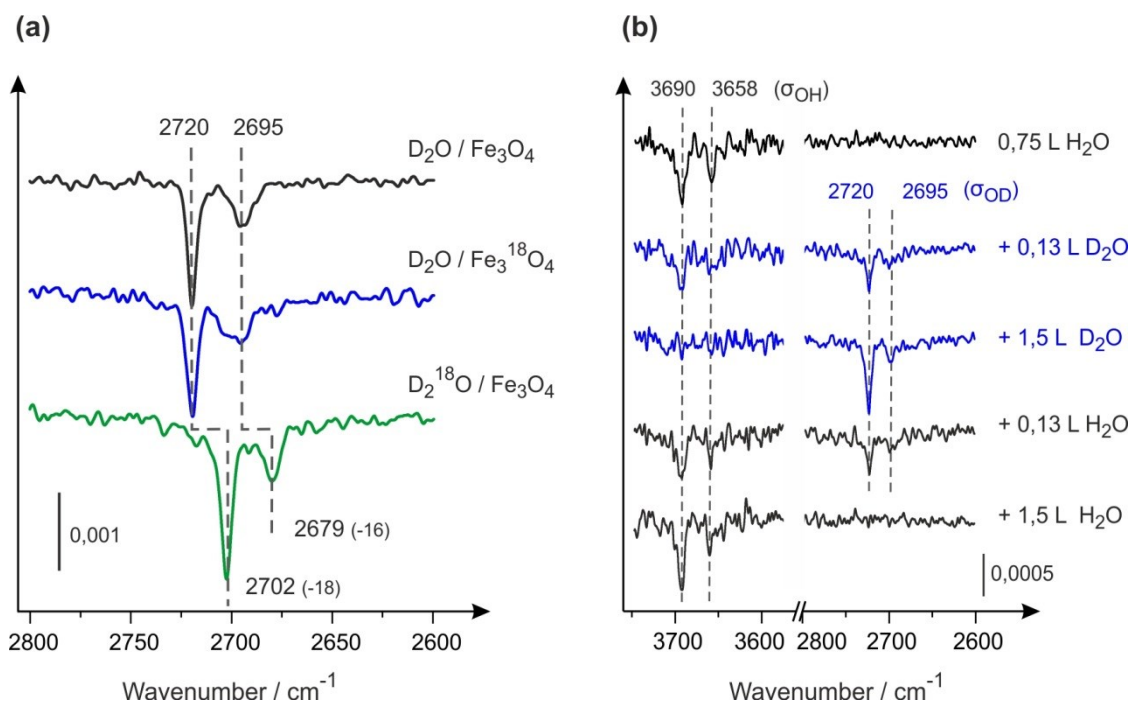


Figure 5.2 a) IRAS spectra obtained at 300 K on $\text{Fe}_3\text{O}_4(111)$ surfaces saturated with water for normal and isotopically labeled water and Fe_3O_4 . b) IRAS spectra obtained at 300 K on $\text{Fe}_3\text{O}_4(111)$ surfaces in an isotope-exchange experiment.

surface oxygen as previously assumed. Instead, both OD vibrations involve an O-atom originating from gas-phase dosed water. This observation provides clear experimental evidence, that these vibrational features cannot be explained in a simple way by two individual OD groups created upon dissociation of a single water molecule and that the previously discussed model is incorrect.

The series of spectra shown in Figure 5.2b demonstrates that adsorption of the surface species is fully reversible. The surface was saturated first with H_2O (uppermost spectrum) and subsequently was exposed to D_2O via a second molecular beam. After about 1.5 L (1 L = 10^{-6} Torr s) D_2O exposure, full replacement of H_2O -related species (3690 and 3658 cm^{-1}) by the D_2O -related species (2720 and 2695 cm^{-1}) was detected (blue spectra in Figure 5.2b). Vice versa, by exposing the D_2O covered surface to an H_2O molecular beam, a complete exchange of D_2O -related species by H_2O -related species was observed. Importantly, the intensity of both vibrational bands was

decreasing (increasing) simultaneously with the same characteristic time constant, that is, there was no pronouncedly faster vanishing of one of the bands as compared to the other. These observations – alongside with results of the isotopic labeling experiments – indicate that the observed surface species are very likely coupled rather than fully spatially separated on the surface as in the latter case exchange kinetics with different characteristic time constants are to be expected.

To obtain detailed atomistic insight into the interaction of water with the magnetite surface, we accomplished a DFT study using the PBE+U approach. Figure 5.3 shows the optimized structures of one and two water molecules adsorbed on the octahedrally ($\text{Fe}_{\text{oct}2}$, Figure 5.3a and b) and tetrahedrally ($\text{Fe}_{\text{tet}1}$, Figure 5.3c and d) terminated $\text{Fe}_3\text{O}_4(111)$ surfaces as well as the respective adsorption enthalpies. According to our data and previously published studies on the stabilities of bulk terminated $\text{Fe}_3\text{O}_4(111)$ surfaces, the $\text{Fe}_{\text{oct}2}$ and $\text{Fe}_{\text{tet}1}$ terminations are 1) comparably stable in surface energy, and 2) they are the most stable ones for a broad range of oxygen chemical potentials.^[188] Vibrational frequencies computed for all experimentally investigated isotopically labeled configurations of either water or the iron oxide surface are summarized in Table 5.1.

Adsorption of a single D_2O molecule on the $\text{Fe}_{\text{oct}2}$ terminated surface, which corresponds to a coverage of $3.2 \cdot 10^{14} \text{ cm}^{-2}$, results in water dissociation and formation of two individual OD groups with the corresponding formation enthalpy of -133 kJ mol^{-1} (Figure 5.3a). While the calculated frequency of the OD group coordinated to the Fe cation (2754 cm^{-1}) agrees well with the experimentally observed range $2720\text{--}2695 \text{ cm}^{-1}$; the frequency of an OD vibration involving a 3-fold coordinated surface oxygen atom – indicated in the literature as “bridging OH”^[172] – was found to be considerably lower (2439 cm^{-1}). Experimentally, no vibrational band was observed for such a low frequency range. In addition, calculated frequency shifts for the various isotopically labeled structures do not agree with observed values.

In contrast to the $\text{Fe}_{\text{oct}2}$ terminated surface, water adsorbs non-dissociatively on the $\text{Fe}_{\text{tet}1}$ terminated surface with the corresponding

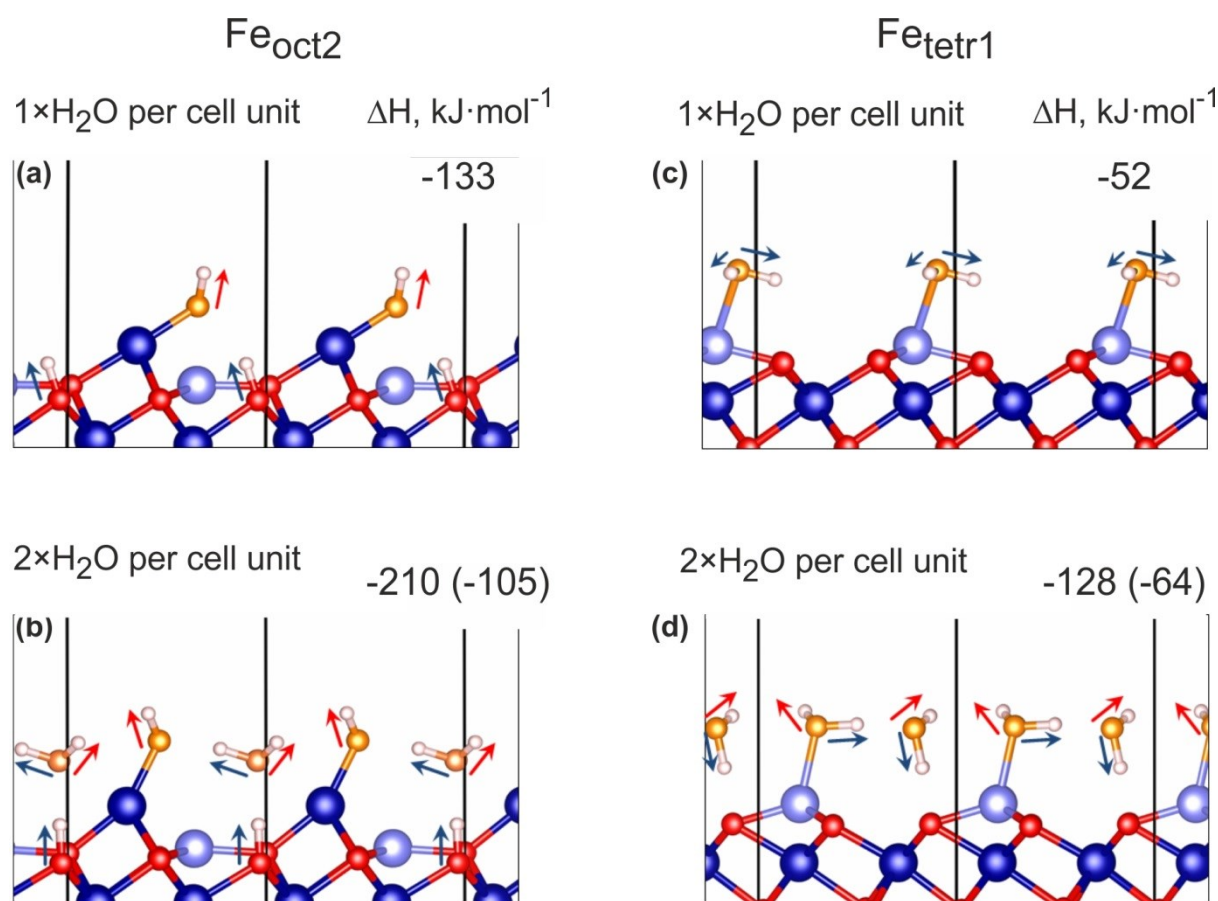


Figure 5.3 Calculated PBE+U adsorption structures of one and two water molecules on the a,b) $\text{Fe}_{\text{oct}2}$ - and c,d) $\text{Fe}_{\text{tet}1}$ -terminated $\text{Fe}_3\text{O}_4(111)$ surface. The reaction enthalpy at 0 K in kJ mol^{-1} is given in the upper right of individual graphs. For dimer formation, the reaction enthalpy per molecule is given in parentheses. Octahedrally coordinated Fe atoms are dark blue, tetrahedrally coordinated Fe atoms light blue, lattice oxygen is red, oxygen in water is orange, and hydrogen is white.

formation enthalpy of -52 kJ mol^{-1} (Figure 5.3c). Computed vibrational frequencies (2687 and 2569 cm^{-1}) and isotopic shifts of this molecular water adsorbate are in strong disagreement with experimentally measured IR spectra. As a result for the adsorption of a single water molecule on both investigated terminations, neither calculated adsorption enthalpies nor vibrational frequencies nor frequency shifts upon isotopic labeling were found to match the experimentally measured values. This observation agrees well with the above discussed experimental IR data, implying that both observed vibrational peaks involve an oxygen atom from gaseous water

molecules and proving that the formation of two individual hydroxyl groups is inconsistent with the experiment. Thus, based on both theoretical and experimental results, formation of two individual and spatially separated OD groups out of a single water molecule can be safely ruled out.

Next, we examined the formation of a possible dimer-like structure upon adsorption of two water molecules per unit cell (corresponding to formal water coverage $6.4 \cdot 10^{14} \text{ cm}^{-2}$) for both surface terminations. On the $\text{Fe}_{\text{oct}2}$ terminated surface, the first water molecule undergoes dissociation and forms two individual OD groups. According to the calculations, the second water molecule does not dissociate and forms a complex with the hydroxyl groups instead. Figure 5.3b shows the optimized, most stable structure of this dimer complex, in which two hydrogen bonds are created. The adsorption enthalpy of this dimer is -210 kJ mol^{-1} , or -105 kJ mol^{-1} per water molecule, which is very close to the measured value of 101 kJ mol^{-1} . This dimer complex involves stretching modes of the terminal OH (OD) groups (red arrows in Figure 5.3b) as well as modes assigned to H-bonded hydroxyl groups or water species (blue arrows). The two calculated frequencies of the terminal OD vibrations (2740 and 2710 cm^{-1} , see Table 5.1) as well as the difference between these vibrational frequencies ($\Delta\nu_{\text{theor}} = 30 \text{ cm}^{-1}$) are in very good agreement with the experimental data (2720 and 2695 cm^{-1} , $\Delta\nu_{\text{exp}} = 25 \text{ cm}^{-1}$). The vibrational frequencies related to the H-bonded normal modes of this complex are 2270 and 2020 cm^{-1} . For this particular range, no vibrations were experimentally observed, most likely due to band broadening caused by H bonding and due to the metal surface selection rule. The latter explanation can be corroborated by a normal mode analysis, which shows that the surface OD group and the D atom of the intact water molecule (blue arrows in Figure 5.3b) couple to a single vibrational mode with a pronounced parallel component to the metallic magnetite surface. Therefore, they cannot be compared with the experiment. The computed shifts upon isotopic labeling are also in agreement with the observations. Labeling of the Fe_3O_4 surface with ^{18}O did not result in any frequency shift of the terminal OD groups, while labeling of the water with ^{18}O shifts both terminal OD peaks by 17 and 18 cm^{-1} .

Table 5.1 *Computed vibrational frequencies in cm^{-1} compared with experiment. Shifts induced upon ^{18}O labeling of either water or Fe_3O_4 are given in parenthesis. Terminal, bridging, and hydrogen-bonded OH groups are labeled with t, b, and h, in square brackets, respectively. Harmonic scaled frequencies obtained using the PBE+U approach with $U=3.8$ eV and a scaling factor of 0.9935.*

	Experiment	$\text{D}_2\text{O}/\text{Fe}_{\text{oct}2}$	$(\text{D}_2\text{O})_2/\text{Fe}_{\text{oct}2}$	$\text{D}_2\text{O}/\text{Fe}_{\text{tet}1}$	$(\text{D}_2\text{O})_2/\text{Fe}_{\text{tet}1}$
$(\text{D}_2\text{O})_n/\text{Fe}_3\text{O}_4$	2720 2695	2754 [t] 2439 [b]	2740 [t] 2710 [t] 2270 [b] 2020 [h]	2687 2569	2707 [t] 2692 [t] 1832 [h] 1638 [h]
$(\text{D}_2\text{O})_n/\text{Fe}_3^{18}\text{O}_4$	2720 2695	2754 (0) 2423	2740 (0) 2710 (0) 2255 2020	2687 2569	2707 (0) 2692 (0) 1832 1638
$(\text{D}_2^{18}\text{O})_n/\text{Fe}_3\text{O}_4$	2702 (-18) 2679 (-16)	2737 (-17) 2439	2723 (-17) 2692 (-18) 2270 2006	2667 2558	2690 (-17) 2675 (-17) 1818 1625

In total, the computationally characterized dimer complex consisting of one dissociated and one intact water molecule in the $\text{Fe}_{\text{oct}2}$ terminated $\text{Fe}_3\text{O}_4(111)$ surface was found to match all experimental observations.

On the $\text{Fe}_{\text{tet}1}$ -terminated surface both water molecules adsorb molecularly. Two non-dissociated molecules form a complex with an adsorption enthalpy of -64 kJ mol^{-1} per water molecule (see Figure 5.3d), which is about two thirds of the measured value (101 kJ mol^{-1}). The two highest frequencies computed for this dimer – 2707 and 2692 cm^{-1} – lie close to the experimentally observed values (2695 and 2720 cm^{-1}). However, the remaining frequencies are predicted to be within $1630\text{--}1830 \text{ cm}^{-1}$, where no bands were observed. While the vibrational frequencies and their shifts upon isotopic labeling of the water dimer on the $\text{Fe}_{\text{tet}1}$ -terminated surface are in relatively good agreement with experimental observations, its calculated formation enthalpy markedly disagrees with the measured energies. Overall, the calculated properties of only one structure – the hydroxyl–water complex adsorbed on the $\text{Fe}_{\text{oct}2}$ -terminated $\text{Fe}_3\text{O}_4(111)$ – are fully consistent with all available experimental observations.

Previously, formation of long-range ordered dimer-like superstructures of water was reported for ZnO, in which half of the water molecules on the fully covered on ZnO(10-10) surface self-dissociate resulting in a well-defined (2×1) superlattice.^[179] Spectroscopically, two vibrational peaks and a shoulder were observed for this structure, which were assigned to two individual OH groups and molecular water. However, no isotopic labeling of water and ZnO were performed in this study that would make possible the unambiguous assignment of these peaks to water and lattice oxygen-related species. It remained also unclear if the dimer-like structures could be formed at low water coverages or their stabilization by H bonding in the long-range superlattice is required. Other vibrational studies carried out on TiO₂^[178] and Fe₃O₄^[48] suggest dissociation of a water molecule to two individual OH groups.

5.4 Conclusions

In summary, the interaction of water with a well-defined model Fe₃O₄(111) surface was investigated for the first time using highly accurate direct calorimetric measurements under UHV conditions. Complementary, spectroscopic identification of the surface species was performed by IRAS. We showed that the adsorption energy of water on Fe₃O₄(111) is considerably higher than all previously reported values obtained by indirect desorption-based methods. By employing isotopically labeled water and Fe₃O₄ substrate, we experimentally proved that the generally accepted simple model of water dissociation to form two individual OH groups per water molecule is not correct. DFT calculations suggest formation of a dimer, which consists of one water molecule dissociated into two OH groups and another non-dissociated water molecule creating a thermodynamically very stable dimer-like complex. Calculated vibrational frequencies, their shift upon selective isotopic labeling of either water or the substrate with ¹⁸O as well as the formation energy of an OH–water complex on the Fe_{oct}2-terminated Fe₃O₄(111) surface are in agreement with corresponding experimental data. Less agreement was found for water adsorption on the Fe_{tet}1-terminated surface.

§ 6 Surface chemistry of water on magnetite: a mechanistic study[□]

6.1 Abstract

We present a mechanistic study on the interaction of water with a well-defined model $\text{Fe}_3\text{O}_4(111)$ surface that was investigated by a combination of infrared vibrational spectroscopy and direct calorimetric measurements of adsorption energies. This process was studied for the first time in a broad range of temperature and coverage conditions and direct correlations between the water adsorption energy and the specific surface species identified spectroscopically were established. For the lowest coverage limit, water was shown to form dimer-like hydroxyl-water complexes and not two individual OH groups as it was assumed in the previous dissociative adsorption model. We also demonstrate that water adsorption energy at low coverages, amounting to 101 kJ mol^{-1} , substantially exceeds all previously reported values obtained by indirect desorption based methods. With increasing total water coverage, strongly decreasing binding energies were measured, indicating strong interaction in this system. Spectroscopic data point to formation of tri- and further oligomer species with increasing water coverage. We report highly accurate energy values as a detailed function of surface temperature, water coverage and the chemical structure of the adsorbates that can serve as high quality benchmarks for theoretical calculations.

6.2 Introduction

Interaction of water with oxide surfaces is of tremendous scientific and practical importance due to the ubiquity of these interfaces in the natural environment and a widespread use in modern technological applications such as heterogeneous catalysis, photo- and electrochemistry, renewable

[□] The following chapter has been submitted for publication to the Journal of Physical Chemistry C by Petr Dementyev, Casey P. O'Brien, Karl-Heinz Dostert, Francisco Ivars-Barceló, Francesca Mirabella, Jan Seifert, Svetlana Schauer mann, and Hans-Joachim Freund

energy production and storage. Particularly important is interaction of water with one of the most abundant class of oxides – iron oxides, which are central components to a multitude of modern technological processes.^[189] Being a multivalent element, iron can form oxides with different stoichiometry and different surface terminations^[16, 120] allowing to finely tune the physical and chemical properties of the final material by an appropriate preparation procedure or by choosing suitable operation conditions. Presence of water may have a great impact on this process as it can strongly interact with an oxide surface, form hydroxyls and stabilize or destabilize particular surface structures or terminations.

Interaction of water with different types of oxides was previously investigated at the atomistic level on model surfaces of TiO_2 ,^[100, 172, 177, 178, 190] ZnO ,^[191, 192] Fe_3O_4 ^[48-50, 146], Fe_2O_3 ^[181], RuO_2 ^[193] and some others. While these studies – mainly employing imaging techniques – provided some important insight into water interaction with oxides, the detailed atomistic picture of this process is still under debate. Particularly the reliable spectroscopic identification of surface species formed on the oxides is rare and is mainly related to high water coverages, while the initial stages of water adsorption and dissociation remain largely unexplored. Also consistent information on the interaction energy of water with oxide surfaces is hardly available, mostly due to the fact that it has been commonly addressed by desorption-based methods such as e.g. temperature programmed desorption (TPD) and equilibrium adsorption isotherm measurements (EAI), having very limited applicability to the complex non-reversible processes and relying on assumptions about the details of the desorption process, which might lead to strong deviations of the deduced energy values.

Particularly for magnetite (Fe_3O_4), there is limited understanding of the nature of the surface species formed upon water adsorption and dissociation. Previous spectroscopic studies suggest formation of two surface hydroxyl groups at low coverages.^[48, 49] Recently, by applying a combination of molecular beam techniques, infrared spectroscopy and density functional theory, we have shown that this well-accepted model is incorrect and water adsorbs on $\text{Fe}_3\text{O}_4(111)$ surface as a dimer-like water-hydroxyl complex even

at the lowest water coverages.^[194] Limited applicability of TPD to highly complex dissociative processes, which might be additionally accompanied by some irreversible steps such as e.g. building water-hydroxyls complexes, restructuring of the uppermost oxide layers etc, results in rather contradictory information on the energetics of water-magnetite interaction. A strategy to overcome these limitations is a direct calorimetric measurement of adsorption and dissociation energies under isothermal conditions.^[195, 196]

In this report, we present a comprehensive atomistic picture of water interaction with a well-defined magnetite $\text{Fe}_3\text{O}_4(111)$ surface in a broad range of temperature and coverage conditions. We employ for the first time a combination of direct calorimetric technique (single crystal adsorption calorimetry, SCAC), molecular beams and *in-situ* infrared spectroscopy (IRAS) to obtain detailed microscopic information on the surface species formed upon water interaction with this surface and determine the binding energies associated with a particular species.

In contrast to the previously assumed model, we show that water does not form two individual hydroxyls upon dissociation in the low coverage limit, but a dimer-like hydroxyl-water complex is formed. The adsorption energy associated with this process was measured to amount 100 kJ mol^{-1} , which is significantly higher than all previous values obtained by indirect desorption-based methods.

In the higher coverage limit, which was reached by increasing water exposure and lowering the surface temperature, water was found to build more complex surface species that can be related to trimers and higher oligomers. The formation energies of these higher hydroxyl-water complexes are reported. For all investigated temperatures, a very strong dependence of water adsorption energy on the water coverage was detected that is likely originates from the long-range coupling of the adsorbates via the Fe_3O_4 . The obtained highly accurate energy values and chemical composition of the corresponding water-related surface species can serve as high quality benchmarks for theoretical calculations.

6.3 Results and Discussion

6.3.1 Energy Measurement at 120 K

Adsorption of water was first probed by SCAC at 120 K on three different model surfaces: pristine Pt(111) and two model thin oxide layers FeO(111)/Pt(111) and Fe₃O₄(111)/Pt(111). Figure 6.1 shows a comparison of differential adsorption energies of water on these surfaces measured as a function of the number of adsorbed water molecules per cm² (shown on the x-axis). In these experiments, the particular surface was exposed to 266 ms long pulses of water molecules produced by a modulated molecular beam. Each pulse carried $\sim 5 \cdot 10^{12}$ water molecules; The repetition rate of the pulses was of 0.5 Hz. Water adsorption results in a small temperature rise (ca 3-4 mK) that is measured by a sensitive pyroelectric detector, which is brought in contact with the back side of the crystal. The absolute energy value is calculated based on an independent energy laser calibration. The energy measurement is combined with a sticking coefficient measurement via the King-Wells method,^[187] allowing a quantitative determination of the absolute number of adsorbed water molecules. Further details on the measurement procedure can be found elsewhere.^[196]

On Pt(111) and FeO(111), the initial adsorption energy amounts to 44.3 ± 0.8 and 47.3 ± 0.5 kJ mol⁻¹ and remains nearly constant while water is accumulated and finally forms water ice. The low adsorption energies measured on these two surfaces are indicative of a physisorption process. In contrast, the initial adsorption energy of water on Fe₃O₄/Pt(111) surface reaches a very high value of 86.9 ± 0.6 kJ mol⁻¹ at 120 K, pointing to a strong chemical interaction, i.e. dissociation. On this surface, the differential adsorption energy shows very strong coverage dependence and continuously decreases with increasing water coverage until it reaches the value of 43.2 ± 2.0 kJ mol⁻¹ characteristic for ice formation. Two reasons can in principle account for the decreasing adsorption energy with increasing water coverage: lateral repulsion of neighboring adsorbates and long range interaction of the adsorbates via the support, i.e. via increasing competition for the electrons of the Fe₃O₄ substrate participating in the bonding. The

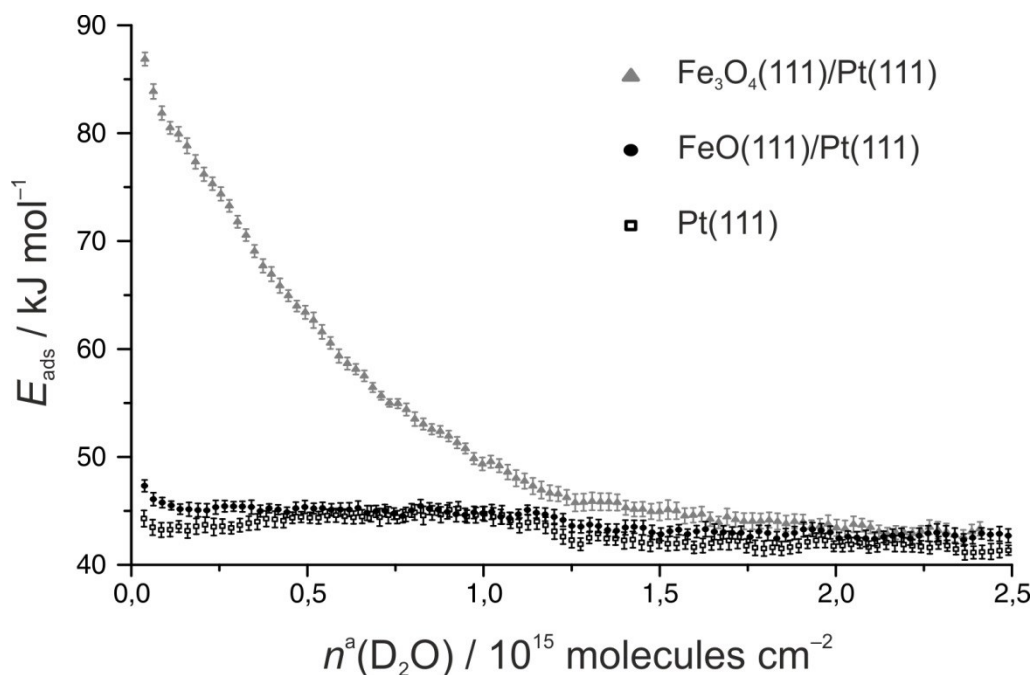


Figure 6.1 Adsorption energy of water as a function of the number of adsorbed molecules measured on three types of surfaces at 120 K. The data points are averages of about 10 independent measurements; the error bars are the average of the mean.

measured energy levels off after adsorption of about $1.25 \cdot 10^{15}$ water molecules per cm^2 at the value of $46 \pm 0.7 \text{ kJ mol}^{-1}$.

Previously, the energetics of water adsorption on Pt(111) was measured by Campbell and coworkers as a function of temperature.^[197] At 120 K, the adsorption energy of $51.3 \pm 1.6 \text{ kJ mol}^{-1}$ was reported for 0.5 ML coverage and $47.2 \pm 1.4 \text{ kJ mol}^{-1}$ for coverages higher than 1.0 ML. This value is in an agreement with our experimental data $41.8 \pm 1.9 \text{ kJ mol}^{-1}$, $42.8 \pm 1.8 \text{ kJ mol}^{-1}$ and $43.2 \pm 2.0 \text{ kJ mol}^{-1}$ measured on Pt, FeO and Fe₃O₄ surfaces, correspondingly, in the multilayer adsorption regime.

Interestingly, initial water adsorption energy on magnetite equals to $86.9 \pm 0.6 \text{ kJ mol}^{-1}$ and is about twice higher as on FeO(111) and Pt(111), which indicates strong chemical interaction that is consistent with previously suggested dissociative adsorption. With increasing coverage, adsorption energy decreases gradually and rather steeply without showing any clear transition from chemisorption to physisorption. The initial value of water adsorption energy measured in our study is higher than all previously

reported values in the literature. Early TPD studies suggest very low binding energy of water on Fe_3O_4 ($50 \pm 10 \text{ kJ mol}^{-1}$),^[49] which was found to be close to a water physisorption energy on chemically inert FeO (52 kJ mol^{-1}). More reliable isosteric heat of adsorption reported in the same study amounts to $60\text{--}73 \text{ kJ mol}^{-1}$.^[49] It is noteworthy that our calorimetric data show that adsorption energy on Fe_3O_4 continues to slightly decrease even at coverages formally corresponding to the adsorption in the second layer as compared to adsorption on Pt and FeO . The constant value of adsorption energy establishes only after the number of adsorbed water molecules exceeds $2 \cdot 10^{15} \text{ molecules} \cdot \text{cm}^{-2}$. This observation can indicate that water adsorption in the second layer is still sensitive to the presence of the underlying substrate and does not correspond to water adsorption on water ice.

To ensure that the $\text{Fe}_3\text{O}_4(111)$ surface discussed in this study is structurally the same as the surfaces investigated in previous studies, we performed TPD measurements using D_2O . The obtained TPD traces shown in Figure 6.2 are similar to those measured by Joseph et al. with H_2O ^[49] and Leist et al. with D_2O ^[48]. At lower coverages water desorbs between 200 and 300 K, which was previously assigned to physisorbed and chemisorbed species. The peak centered at around 170 K is related to multilayer desorption and in our experiments it appears at exposures $> 4 \text{ L}$. The high-temperature peaks in all TPD studies are relatively broad, so that meaningful distinguishing between different adsorption states is hardly possible. In our experiment, deposition of water was performed by using a molecular beam allowing very precise quantification of the absolute adsorbed amounts of water. The insert in Figure 6.2 shows the measured amounts of desorbed D_2O in each TPD run as a function of the number of deposited molecules, showing the expected linear dependence. By comparing our TPD results with the previously reported ones, we concluded that Leist et al. may have underestimated the coverages reported for their infrared spectra based on TPD analysis,^[48] while Joseph et al. using TPD calibration ascribed too low saturation surface concentration for their γ -species.^[49]

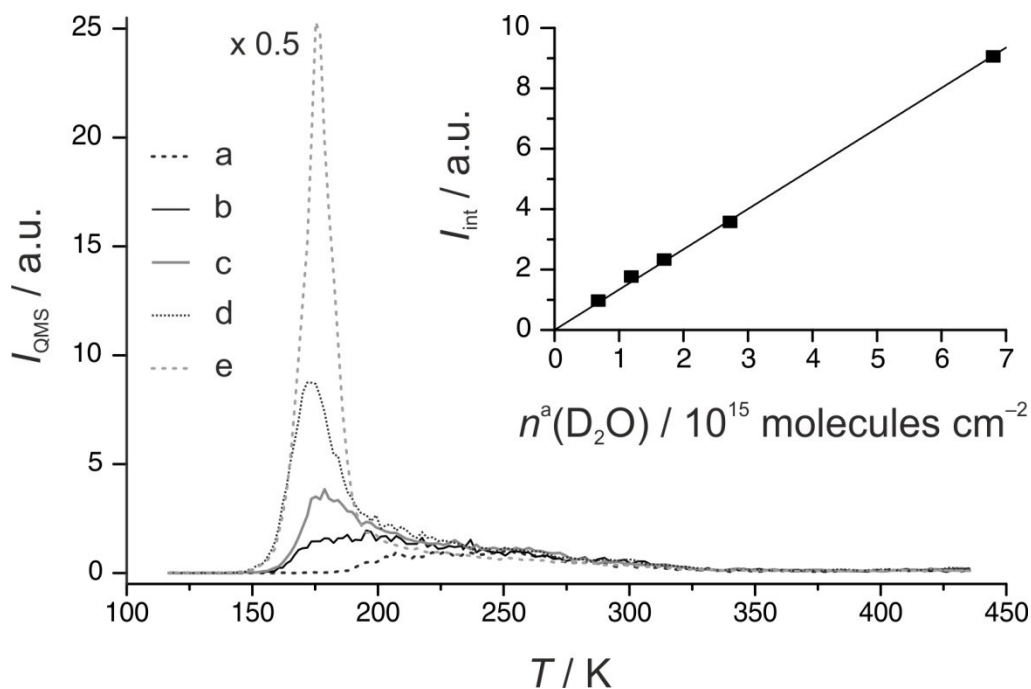


Figure 6.2 TPD spectra of D_2O adsorbed on $\text{Fe}_3\text{O}_4(111)$ upon exposure: a) 1.5 L, b) 2.63 L, c) 3.76 L, d) 6.02, e) 15.04 L. QMS signal $m/z=20$ was monitored, heating rate was $\sim 4 \text{ K s}^{-1}$. Integrated areas under the TPD traces are plotted in the insert versus the number of adsorbed D_2O molecules calculated with a unity sticking coefficient.

6.3.2 Energy Measurement at 180-300 K

The energetics of water interaction with Fe_3O_4 substrate at the surface temperatures 120, 180, 240, and 300 K are shown in Figure 6.3. At 120, the water adsorption energy starts from $\sim 87 \text{ kJ mol}^{-1}$ and results in water ice formation at high coverages with the adsorption energy of $43.2 \pm 2.0 \text{ kJ mol}^{-1}$. At all higher temperatures, the initial adsorption energy at higher temperatures reaches $101 \pm 2 \text{ kJ mol}^{-1}$ and no multilayer ice is formed, in agreement with previous reports showing that under UHV conditions (10^{-10} mbar) no ice multilayers are formed at temperatures above 160 K.^[49] This increase of the binding energy from 87 kJ mol^{-1} at 120 K to $101 \pm 2 \text{ kJ mol}^{-1}$ at the temperatures above 180 K is most likely related to a kinetic hindrance of water dissociation at 120 K, which is lifted at higher temperatures. Since the initial adsorption energy remains constant for all other investigated temperatures, this value can be considered as the true thermodynamic value

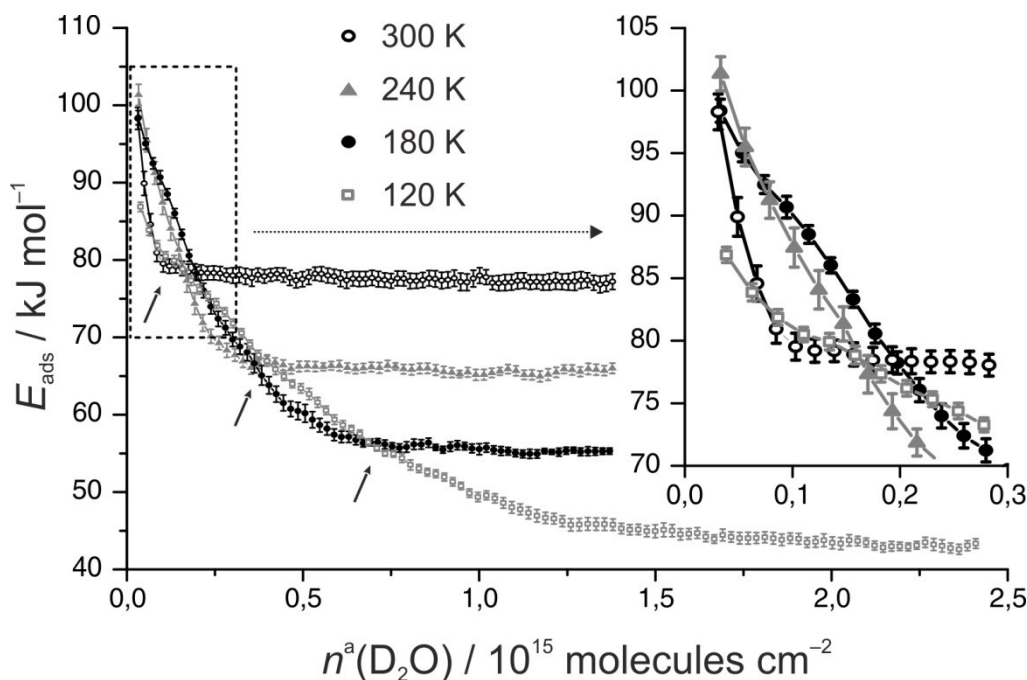


Figure 6.3 Adsorption energy of water on $\text{Fe}_3\text{O}_4(111)$ measured at different temperatures. The data points are averages of about 10 independent measurements; the error bars are the average of the mean.

that is not affected by slow kinetics of water dissociation. Qualitatively, the coverage dependence of water adsorption energy is close to that one observed at 120 K, however, the saturation is reached at lower absolute coverage values (indicated with arrows), that are summarized in Table 6.1. After reaching the saturation, the adsorption system runs into a dynamic adsorption-desorption equilibrium, in which adsorption during the molecular beam pulse is compensated by desorption between two pulses. This regime corresponds to the flat part of the energy curve at high exposures. We found that in the range 180-300 K the sticking coefficient of water on $\text{Fe}_3\text{O}_4(111)$ almost does not depend on the surface coverage and slowly decreases with temperature (see supporting information).

The different saturation coverages and corresponding energies reached at different temperatures resemble differences in the chemical composition of the surface in saturation. While water ice is formed at the lowest temperature, the surface composition at the higher temperatures rather contains a mixture of molecular water and OH groups in different stoichiometry, which depends on the surface temperature. The energy

Table 6.1 *Saturation water coverages on magnetite (111) as a function of T*

Temperature, K	Number of adsorbed molecules in saturation, 10^{15} molecules \cdot cm $^{-2}$
180	0.75 \pm 0.04
240	0.39 \pm 0.05
300	0.13 \pm 0.01

measured in quasi-saturation regime relates to the adsorption process of newly incoming water molecules on the surface with the specific H₂O:OH chemical composition dictated by the surface temperature. The structure of the forming surface species as determined by IRAS will be discussed in the following chapters.

6.3.3 Infrared Spectroscopy at 300 and 240 K

To obtain more atomistic insights into the processes occurring upon water adsorption and dissociation on magnetite surface, we monitored formation of different surface species as a function of water coverage by IRAS in the temperature range between 120 and 500 K. We employed molecular beams to accurately dose water with a high coverage resolution, which allowed us to for the first time spectroscopically monitor very early stages of water interaction with Fe₃O₄.

Figure 6.4 shows two sets of infrared spectra recorded at 300 and 240 K upon increasing exposure of D₂O. The demonstrated wavenumber range includes those characteristic for stretching vibrations of free-standing OD bonds i.e. when D atoms are not directly involved into hydrogen-bonding.^[194] At 300 K two bands centered around 2720 and 2695 cm⁻¹ evolve starting from the lowest coverages. The same features are also seen at 240 K, though the ratio between them changes and the low-frequency band appears rather as a shoulder. At both temperatures, the intensity ratio between the bands changes significantly with increasing surface coverage. Upon saturation at

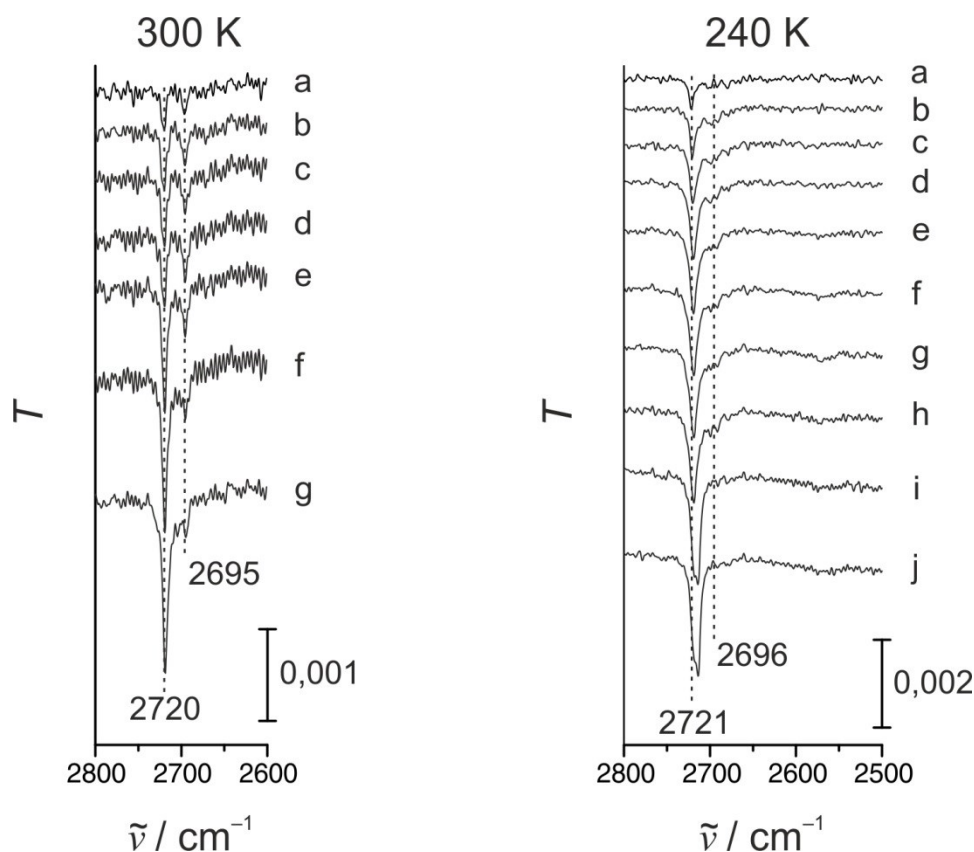


Figure 6.4 Infrared spectra of surface species on $\text{Fe}_3\text{O}_4(111)$ measured at 300 K (on the left) and 240 K (on the right). The spectra are designated as following: at 300 K the spectra a-d were recorded after D_2O exposure of 0.13, 0.25, 0.38, and 0.50 L correspondingly; the spectra e-g were collected under running molecular beam with the flux of $1.1 \cdot 10^{13}$, $5.7 \cdot 10^{13}$ and $5.7 \cdot 10^{14}$ molecules $\text{cm}^{-2} \text{s}^{-1}$ respectively. Similarly, at 240 K the spectra a-h correspond to D_2O exposure of 0.13, 0.25, 0.38, 0.50, 0.63, 0.75, 0.88, and 1.00 L; the spectra i and j were in turn measured upon continuous exposing with the flux of $1.1 \cdot 10^{13}$ and $5.7 \cdot 10^{13}$ molecules $\text{cm}^{-2} \text{s}^{-1}$.

At 240 K they even overlap giving a broad band with a maximum at 2713 cm^{-1} , most likely due to strong coupling between the two modes.

According to the model previously generally accepted in the literature, a water molecule forms two individual surface OH groups with one hydroxyl group bound to a cation site and the other proton occupying an oxygen anion in the oxide lattice. These two different types of hydroxyls were assumed to give rise to two vibrational bands discussed above. In our recent

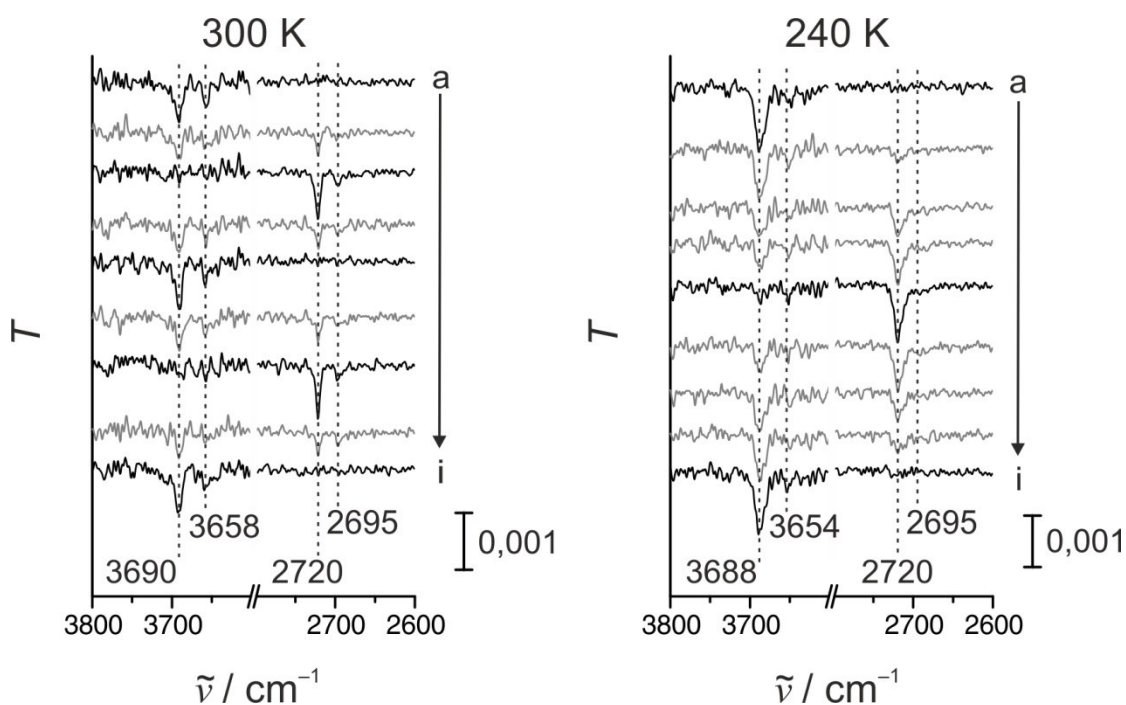


Figure 6.5 Infrared spectra in the regions of terminal OH and OD stretching vibrations at 300 K (on the left) and 240 K (on the right). The spectra a-i at 300 were recorded after successive exposing the sample to 0.75 L H₂O, 0.13 L D₂O, 1.5 L D₂O, 0.13 L H₂O, 1.5 L H₂O, 0.13 L D₂O, 1.5 L D₂O, 0.13 L H₂O, and 1.5 L H₂O. At 240 K 1.5 L H₂O, 0.13 L D₂O, 0.25 L D₂O, 0.25 L D₂O, 1.0 L D₂O, 0.13 L H₂O, 0.25 L H₂O, 0.25 L H₂O, and 1.5 L H₂O were consequentially dosed onto the surface and after each exposure the corresponding spectra a-i were taken.

SCAC/IRAS study combined with density functional theory calculations we have shown that this generally accepted picture is not correct.^[194] Figures 6.5 and 6.6 show the main experimental evidences for this conclusion.

Figure 6.5 shows two series of IRAS spectra obtained upon water adsorption on Fe₃O₄(111) at 300 and 240 K. For 300 K, the surface was saturated first with H₂O; the corresponding vibrational bands were observed at 3690 and 3658 cm⁻¹ (the uppermost spectrum). After that the H₂O molecular beam was closed and the surface was exposed to D₂O via another molecular beam and the IR spectra were collected. Following 1.6 L D₂O dose, full replacement of H₂O-related species by D₂O-related ones was detected, as indicated by the appearance of the bands at 2720 and 2695 cm⁻¹ and

complete vanishing of the bands in the OH-stretching region. Vice versa, by exposing the D₂O-covered surface to an H₂O molecular beam, a complete exchange of D₂O-related species via H₂O-related species was observed. Identical experiments were also conducted at 240 K, at which the exchange of different water species was found to be also fully reversible. As it can be seen in Fig. 6.5, it was possible to perform multiple replacements of regular water by heavy water and the other way around.

Interestingly, the intensity of both vibrational bands was decreasing (increasing) simultaneously with the same characteristic time constant, i.e. there was no pronouncedly faster vanishing of one of the bands as compared to the other. This trend can be particularly pronouncedly seen for 300 K. These observation indicates that the observed surface species are very likely coupled rather than are fully spatially separated on the surface as in the latter case exchange kinetics with different characteristic time constants should be expected.

To further clarify the nature of the surface species formed we performed isotopic labeling experiments by using ¹⁸O-labelled water and Fe₃O₄ substrate. Figure 6.6 shows the IR spectra obtained after water adsorption on regular Fe₃O₄(111) at 300 and 240 K. The uppermost traces were recorded for D₂O molecules adsorbed on a regular Fe₃O₄(111) surface. At 300 K the spectrum exhibit two distinct vibrational bands at 2720 and 2695 cm⁻¹. In earlier reports, vibrational bands in similar frequency range (2712 and 2691 cm⁻¹) were assigned to two individual hydroxy-groups formed from one water molecule.^[48] It was speculated that one of the OD groups binds to an iron atom, while D interacts with a neighboring basic oxygen atom of the oxide lattice and forms a second type of OD groups. To check for the feasibility of this hypothesis, we prepared an isotopically labeled Fe₃¹⁸O₄(111) film by using ¹⁸O₂ as an oxidizing agent and recorded IR spectra of D₂O under identical conditions. Surprisingly, an expected shift of the vibrational band at 2695 cm⁻¹, which was previously assigned to an OD-group involving lattice oxygen, was not observed (spectrum b in Figure 6.6). In contrast, when double isotopically labelled water (D₂¹⁸O) was adsorbed on the regular Fe₃O₄(111) surface, both vibrational peaks shifted to the lower

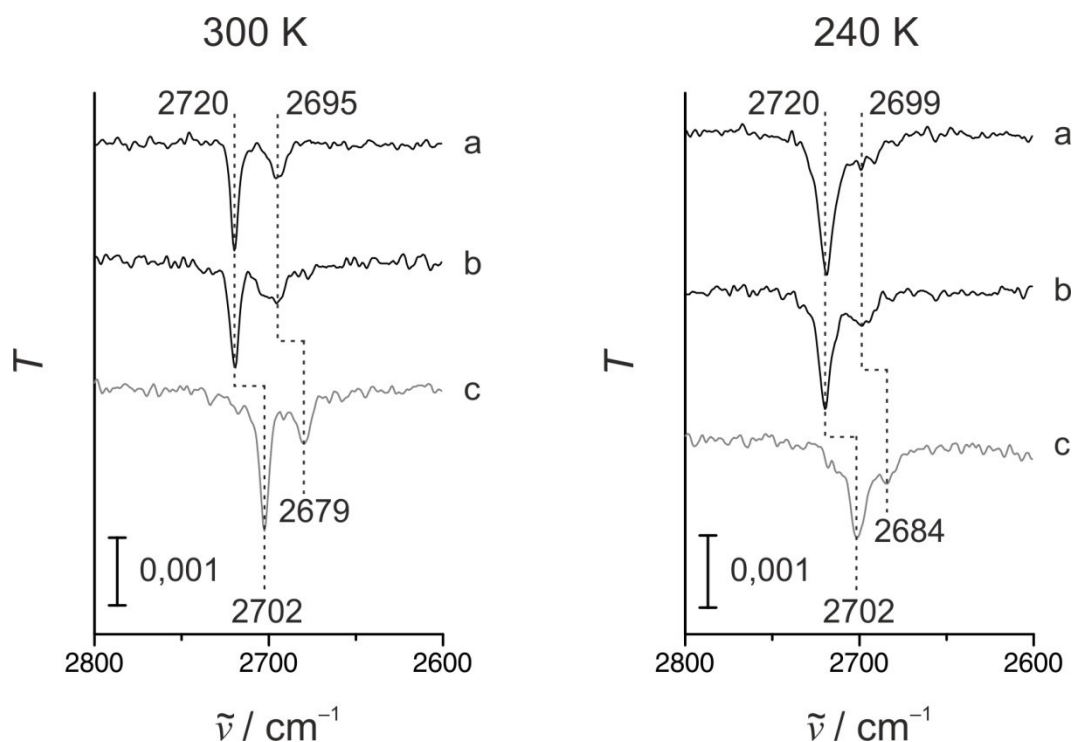


Figure 6.6 Infrared spectra upon isotopic labeling at 300 K and 240 K: a) D_2O on Fe_3O_4 , b) D_2O on $Fe_3^{18}O_4$, c) $D_2^{18}O$ on Fe_3O_4 . In both cases the spectra at saturation are shown.

frequencies by 16 and 18 cm^{-1} , correspondingly (spectrum c in Figure 6.6). These results clearly prove that the low-frequency vibrational band (2695 cm^{-1} at 300 K) does not originate from D adsorption on the lattice oxygen as previously assumed. Instead, both OD-vibrations involve an O-atom originating from the gas phase water. With this we obtained a clear experimental proof that these vibrational features cannot be explained in a simple way by two individual OD groups and the more complex atomistic picture has to be responsible for the observed spectral signature.

Density functional calculations carried out by the group of J. Sauer on this surface suggest formation of a hydroxyl-water dimer-like complex, which consist of one water molecule dissociated to two OH groups and one non-dissociated water molecule (Figure 6.7).^[194] Calculated spectroscopic vibrational signatures, their shifts upon isotopic labeling of either water or the substrate as well as formation energy of an OH-water complex on octahedrally-terminated $Fe_3O_4(111)$ surface were found to be in an excellent

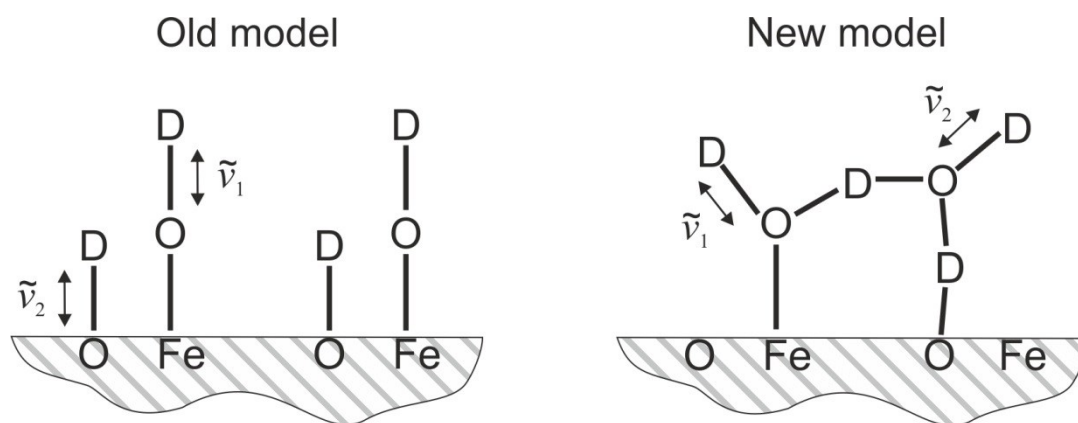


Figure 6.7 Comparison of two models for water adsorption on $\text{Fe}_3\text{O}_4(111)$.

agreement with the corresponding experimental data. Formation of this complex on octahedrally-terminated $\text{Fe}_3\text{O}_4(111)$ surface was also supported by calculated thermodynamic stabilities of different water-related surface species.

The proposed structure of the dimer-like hydroxyl-water complexes can also explain large deviations in the intensity ratio between different peaks observed with growing coverages and changing temperatures. An obviously non-rigid structure of this complex might slightly change upon variation of coverage or temperature so that the orientation of the corresponding dynamic dipole moments with respect to the surface can vary substantially. Since due to the metal surface selection rule the intensity of the IR band is determined only by the projection of the dynamic dipole moment onto the surface normal, even moderate changes in the relative orientation of the vibrating dipoles can result in substantial changes of the intensity ratio, which was experimentally observed in our study.

Saturation surface coverages listed in Table 6.1 represent an absolute amount of water molecules accumulated on the surface. Taking into account the stoichiometry of the dimer-like complexes, one can estimate their surface concentration. At 300 K, $0.6 \cdot 10^{14} \text{ cm}^{-2}$ such complexes are adsorbed at saturation coverage and at 240 K - $2 \cdot 10^{14} \text{ cm}^{-2}$. In comparison with the density of surface unit cells ($\sim 3.2 \cdot 10^{14} \text{ cm}^{-2}$) these numbers are relatively high, which implies that formation of these structures cannot be related only to some surface defects but rather occurs on the regular surface sites.

Additionally, by employing IRAS we monitored the surface composition at the temperatures up to 500 K. Interestingly, the dimer-like complexes can be still seen at 400 K (see supporting information) and even at 500 K, but for the latter temperature the surface has to be continuously exposed to a high flux molecular beam of water. These observations point to an exceptionally high stability of the dimer-like complexes.

6.3.4 Infrared Spectroscopy at 180 and 120 K

According to the previous reports, water adsorbs in multilayers as ice below 170 K and can be present in submonolayer quantities up to 350 K. The IRAS spectra obtained in earlier studies at 110 K reveal rather high complexity and were interpreted based on a number of assumptions. In order to obtain deeper insights into high-coverage water structures, we performed IRAS measurements at 120 and 180 K.

Figure 6.8 shows the IR spectra measured as a function of water exposure at 180 K. The last three spectra were acquired while molecular beam was running; while the rest of the spectra were recorded under UHV conditions after a specific amount of water was deposited via the molecular beam.

At the lowest coverages (Fig. 6.8, a-e), the evolution of the peaks is quite similar to the spectra obtained at 240 K: the major band appears at 2722 cm^{-1} and has a shoulder at $\sim 2695 \text{ cm}^{-1}$, which is, however, even less pronounced than at 240 K. As discussed above, these changes might be related to the conformational changes of the hydroxyl-water complex or be caused by dipole coupling effects between the neighboring complexes and the other water-related surface species. Additionally, a band at 2570 cm^{-1} appears in the spectra in the intermediate coverage regime (Figure 6.8, spectra d-f). The intensity of this band varies with coverage and the band significantly broadens at the higher exposures showing a concomitant decrease of the intensity. Vibrations in this frequency range are typically assigned to hydrogen bonded OD bonds. Upon isotopic labeling of water with ^{18}O , this band was observed to behave in the same way as the other bands, i.e. it exhibits a red-shift by $\sim 10 \text{ cm}^{-1}$. This observation proves that O in this

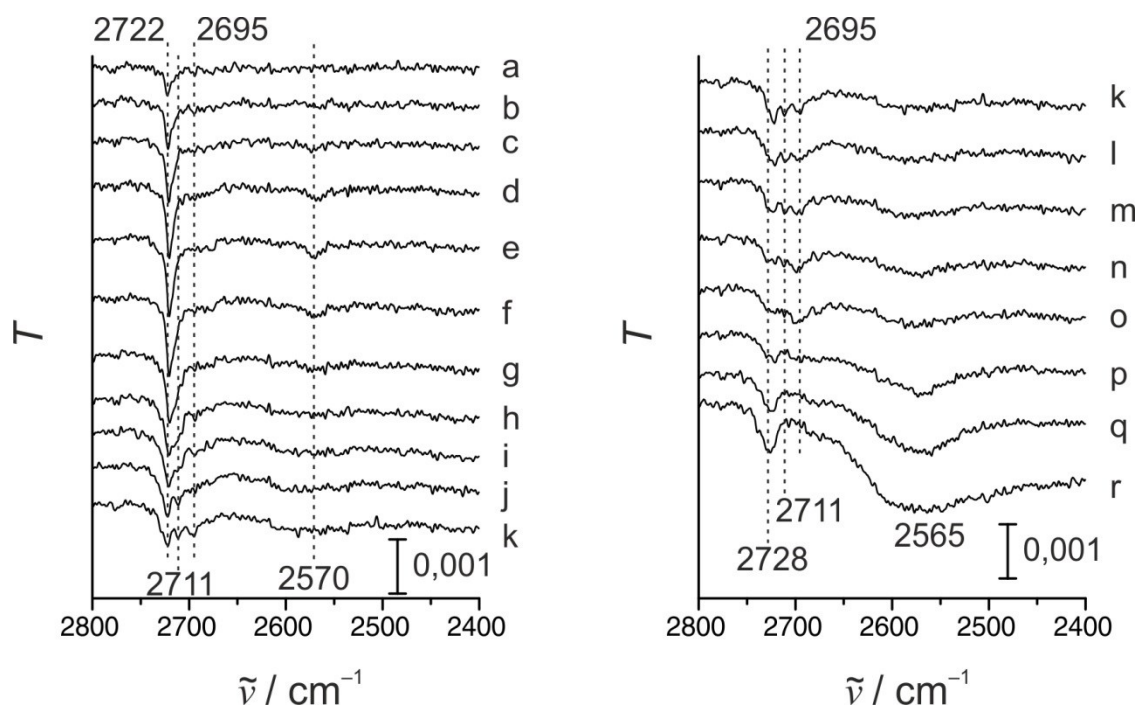


Figure 6.8 Infrared spectra of surface species on $\text{Fe}_3\text{O}_4(111)$ recorded at 180 K after dosing: a) 0.13 L, b) 0.25 L, c) 0.38 L, d) 0.50 L, e) 0.63 L, f) 0.75 L, g) 0.88 L, h) 1.00 L, i) 1.13 L, j) 1.25 L, k) 1.38 L, l) 1.50 L, m) 1.63 L, n) 1.75 L and o) 1.88 L of D_2O . Spectra p, q and r were taken under running molecular beam with the flux of $1.1 \cdot 10^{13}$, $5.7 \cdot 10^{13}$ and $5.7 \cdot 10^{14}$ molecules $\text{cm}^{-2} \text{s}^{-1}$ respectively.

bond originates from gas phase water and not from the lattice. Strong broadening of this band at higher coverages is also consistent with the hypothesis that this bond is involved in hydrogen bonding, which normally results in substantial band broadening.

Starting from the exposure of 1 L (spectrum h), the third vibrational band at 2711 cm^{-1} starts to evolve in the range of terminal hydroxyls. It appears first as a shoulder and develops to a well-resolved peak in the spectra from j to m. Appearance of this band can point to the formation of small water clusters, such as e.g. a hydroxyl-water trimer. Indeed, for a cluster consisting of a hydroxyl group and two water molecules, one can expect three vibrational bands in the range of terminal hydroxyls. Clearly, formation of complexes containing larger numbers of water-related species has to be assumed to explain the appearance of the third band in the vibrational range

of terminal hydroxyls. This hypothesis is also in a good quantitative agreement with the measured number of adsorbed water molecules in saturation. If all adsorbed water would be present on the surface only in form of dimer-like hydroxyl-water complexes, about $6.4 \cdot 10^{14} \text{ cm}^{-2}$ water molecules must be involved in this water layer. The experimentally measured saturation coverage at 180 K amounts to $7.5 \cdot 10^{14} \text{ cm}^{-2}$, which is by ca 20% exceeds the amount of water that can be accumulated in form of dimers. This excess of water must be involved into more complex structures such as e.g. trimer complexes.

Under continuous molecular beam exposure, when the pressure above the surface reaches 10^{-6} mbar, a very broad band at 2570 cm^{-1} grows in intensity and simultaneously a band at 2729 cm^{-1} appears and dominates in the vibrational range of terminal OH groups. Previously, the combination of these two bands was assigned to adsorption of molecular water in multilayers. Our spectra obtained at lower temperatures, at which water ice was formed, allow us to draw the same conclusion since these two bands become dominant and continuously grow in intensity. The vibrational band at 2729 cm^{-1} was previously assigned to sticking-out hydroxyl groups (dangling bonds), while the broad band around 2570 cm^{-1} relates to molecular water involved in a multilayer/ice structure. Therefore we interpret the appearance of these two bands as formation of water ice. It is important to note that the band at 2729 cm^{-1} related to the dangling bonds is not the same as the band at 2720 cm^{-1} appearing at the lowest exposure and assigned to a dimer-like hydroxyl-water complexes.

Very similar adsorption behavior was also observed at 120 K (Figure 6.9), at which first two vibrations characteristic for the dimer formation evolve (spectra a-c in Figure 6.9), then a third band at 2711 cm^{-1} appear in the range of terminal hydroxyl groups, pointing to trimer-like species (spectra g-l in the Fig. 6.9) and, finally, two pronounced bands at 2729 and 2570 cm^{-1} appear and continuously grow in intensity, indicating formation of water ice (spectra m-q, Figure 6.9).

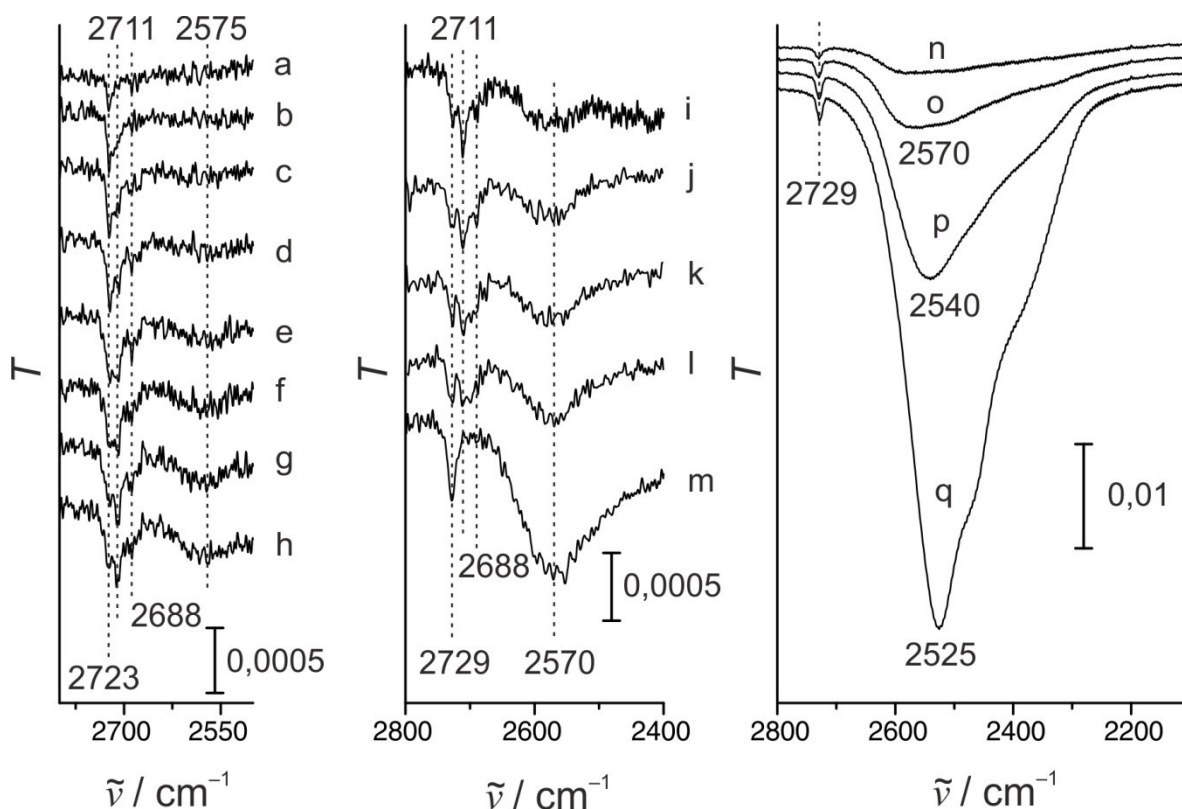


Figure 6.9 Infrared spectra of surface species on $\text{Fe}_3\text{O}_4(111)$ recorded at 120 K. after dosing: a) 0.13 L, b) 0.25 L, c) 0.38 L, d) 0.50 L, e) 0.63 L, f) 0.75 L, g) 0.88 L, h) 1.00 L, i) 1.13 L, j) 1.25 L, k) 1.38 L, l) 1.50 L, m) 2.50 L, n) 4.00 L, o) 7.00 L, p) 14.50 L and q) 30.0 L of D_2O .

The detailed coverage dependence of IR spectra achieved in this study allows us to revisit some of the assignments made previously. Thus, Leist et al.^[48] observed in their study three vibrational bands (2730, 2712, 2691 cm^{-1}) even at their lowest achieved exposure of 0.7 L. Obviously, this situation must be related to already high water coverages, that correspond to the spectra h-i in the Figure 6.9 obtained in the present study. Leist et al. assigned the features at 2712 and 2691 cm^{-1} to two types of surface hydroxyls whereas the third high-frequency peak was attributed to a water molecule bridging these two OH bonds. The infrared spectra were interpreted within the framework of the three-stage adsorption model proposed by Joseph et al.: first, surface hydroxyls are formed (γ -species); then intact water physisorbs (β -species) between them followed by the multilayer

condensation (α -species). In view of the above discussion, this spectral assignment turns out to be incorrect. Based on our isotope experiments, the sequential population of γ - and β -states can be unambiguously ruled out.

It should be noted that - according to SCAC data - the initial adsorption energy of water at 120 K is by $10 \text{ kJ}\cdot\text{mol}^{-1}$ lower than at 180, 240 and 300 K. This discrepancy arises most likely from the kinetic hindrance for water dissociation at 120 K, which results in the situation that both dimer-like hydroxyl-water complexes are formed and also some water adsorbs in a molecular form and is not involved in a dimer-complex. We cannot prove or disprove this hypothesis based on our spectroscopic information as the effect in terms of energy is rather small and the fraction of non-dissociated water is probably too low to not give rise to a prominent vibration in the spectra. It should be kept in mind, however, that this additional non-dissociate water might be present on the surface.

Fig. 6.9 also shows that onset of the peaks in the vibrational range of terminal hydroxyls is accompanied by a broad absorption band in the hydrogen-bonding range (close to 2570 cm^{-1}). This band is somewhat more pronounced than at 180 K, also with respect to the bands of the terminal hydroxyls. The changes in the intensity ratio between the hydrogen-bonded OD bonds (2575 cm^{-1}) and terminal OD bonds (2723 cm^{-1}) is indicative of more complex structures formed at 120 K. One of the possible scenarios might be formation of water clusters (tri-, tetramers or higher), having considerably more O-H bonds involved in hydrogen bonding. Clearly, further theoretical calculations need to be carried out to prove or disprove this hypothesis. It should be also kept in mind that a clear distinguishing between mono- and multilayer adsorption is hardly possible. It is very likely that there is some layer(s) of water between these two states that might exhibit rather complex vibrational signatures as well as have a specific heat of formation. Some experimental indications for the latter hypothesis were discussed above.

6.3.5 Correlation between adsorption energy and spectroscopic information on surface species

The combination of energy measurements by SCAC and spectroscopic identification by IRAS allows us to find direct correlations between surface species and adsorption energy. Figure 6.10 shows an example of such a unique combination at 240 K. Both graphs show strong dependence of the adsorption energy on the coverage and on the abundance of different surface species. Interestingly, the steepest decay of adsorption energy is observed for low coverages considerably lesser than a half monolayer. This observation likely indicates that this strong decay is related not that much to a pure lateral repulsion between the neighboring dimers but rather to a long-range interaction via the underlying oxide.

This hypothesis is also in agreement with strong temperature-dependent conformational rearrangements observed by IRAS even at low coverages. Strong coupling with the substrate is also supported by DFT calculations showing that the density of states of adsorbed water complexes strongly overlaps with that of the substrate. Based on this behaviour, we conclude that water interaction with $\text{Fe}_3\text{O}_4(111)$ should be considered as a strongly interacting system, where one cannot formally separate adsorbent and adsorbate subsystems. This fact supports our previous discussion about very limited applicability of TPD for studying interaction of water with magnetite as the TPD analysis is based on the separation of two subsystems. Additionally, very strong dependence of the binding energy on the coverage can result in complicated dynamics of the desorption process, when the desorption traces reflect to a greater extent the details of the desorption process itself and not the true binding energies of the corresponding species. The very broad distribution of the water binding energies obtained in different desorption-based studies and some obvious contradictions in the magnitude of the binding energies are likely related to these phenomena.

Table 6.2 summarizes the obtained water adsorption energies for different temperatures and selected coverages. The data are reported as differential adsorption energies as referred to the absolute number of adsorbed water molecules. Surface coverage is represented as a ratio of the number of

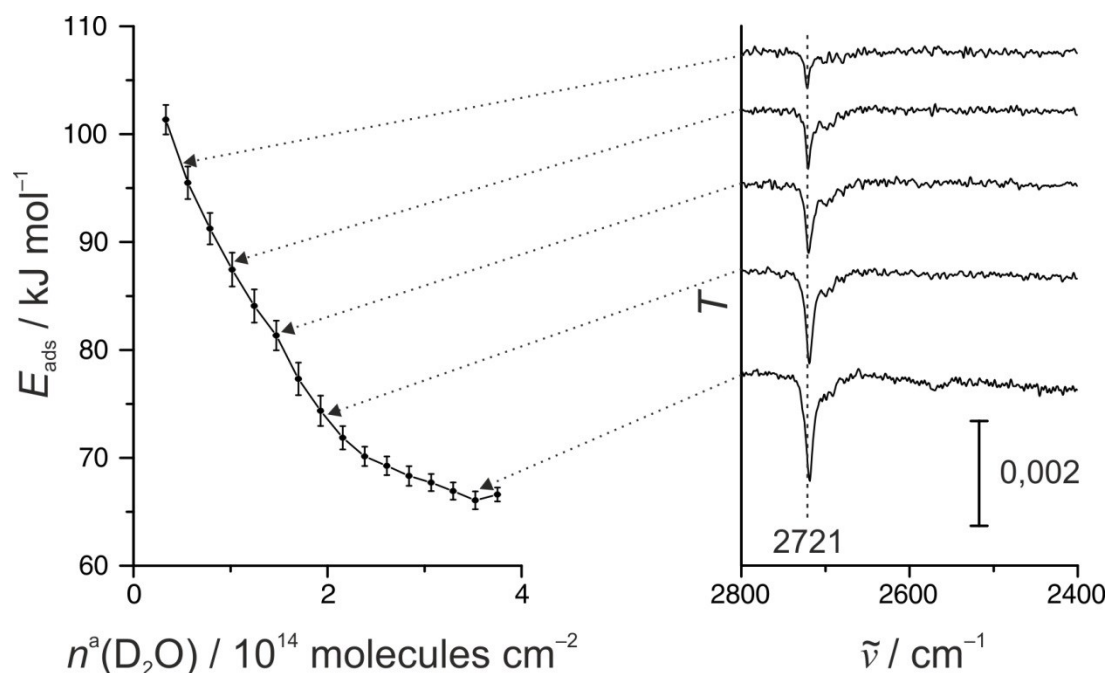


Figure 6.10 Adsorption energy of water measured at 240 K in combination with infrared spectra obtained upon adsorption of indicated amounts of molecules.

adsorbed water molecules to $1.25 \cdot 10^{15} \text{ cm}^{-2}$ (the number of water molecules in a monolayer). At $\Theta < 0.05$ ML the adsorption energy was found to be almost the same for all three temperatures and can be therefore considered as a zero coverage limit; it amounts to 100 kJ mol^{-1} or 200 kJ mol^{-1} per hydroxyl-water complex.

It is interesting to note that the exchange of H_2O dimers by D_2O dimers monitored by IRAS (Figure 6.5) might be indicative of a concerted dissociation process to form a hydroxyl-water complex. Principally, there might be two feasible pathways to form a hydroxyl-water dimer: (i) dissociation of water to form hydroxyl followed by formation a hydroxyl-water complex; (ii) formation of a complex of two water molecules followed by dissociation of one them to form hydroxyl-water complex. If the first scenario would be true, in the intermediate stages of the isotope exchange (when both H_2O and D_2O -related species are still present) we could expect to have on the surface four combinations of complexes: $\text{OH-H}_2\text{O}$, $\text{OD-D}_2\text{O}$, $\text{OH-D}_2\text{O}$ and $\text{OD-H}_2\text{O}$. These combinations should result in the splitting of the

Table 6.2 Adsorption energy of water on $\text{Fe}_3\text{O}_4(111)$ as a function of temperature and surface coverage

Θ , ML T, K	0.05	0.1	0.2	0.4	0.6	1.0
120	84	80	74	63	55	46
180	94	87	73	60	56	--
240	94	84	70	--	--	--
300	86	--	--	--	--	--

corresponding pairs of vibrational bands (2720 and 2695 cm^{-1} for OD region and 3690 and 3658 cm^{-1} for OH region) to two quadruplets, which was not observed experimentally. In contrast, the second scenario implies that only OD- D_2O and OH- H_2O complexes can be formed, which should give rise to two doublets of the IR bands – which perfectly fits the experimental observations (see spectrum b in the Figure 6.5). It should be kept in mind, however, that if the splitting of the vibrational bands in the first scenario would not be large enough to be detected, we could not differentiate between these different pathways. Further theoretical work is clearly needed to resolve this question.

6.4 Conclusions

Interaction of water with single crystalline model $\text{Fe}_3\text{O}_4(111)$ was investigated under UHV conditions using a combination of single crystal adsorption calorimetry and infrared spectroscopy. The energetics of water adsorption and dissociation on this surface was for the first time addressed by a highly accurate direct calorimetric technique under isothermal conditions. Complementary, the spectroscopic identification of the surface species formed upon water adsorption was performed by IRAS within a broad range of temperature and coverage conditions.

In the lowest coverage regime, the water adsorption energy was measured to amount to 100 kJ mol⁻¹, which is significantly higher than all previous values obtained by indirect desorption-based methods. By employing isotopically labeled water and Fe₃O₄ substrate in IRAS experiments, we experimentally prove that the generally accepted simple model of water dissociation to form two individual OH groups is not correct. The two vibrational bands, which were previously attributed to a terminal OH-group steaming from gaseous water and an OH group involving lattice oxygen, were shown to originate exclusively from gaseous water dosed on the surface. With the help of theoretical calculations, these vibrational bands could be explained by formation of a dimer-like structure consisting of one water molecule dissociated to two OH groups and one non-dissociated water molecule. Evolution of two vibrational bands indicative of dimer formation was observed at the initial stages of water interaction with Fe₃O₄(111) at all investigated temperatures; however, the relative ratio of the band intensities substantially varies with temperature, pointing to possibility of temperature-dependent conformational changes of a hydroxyl-water complex.

In the higher coverage limit, which was reached by increasing water exposure and lowering the surface temperature, water was found to build more complex surface species that can be related to trimers and higher oligomers. Finally, at even higher coverages (i.e. lower temperatures), water forms mono- and multilayer of non-dissociated molecules, exhibiting specific well-known patterns in IR spectra. It can be speculated that formation of trimer-like species is associated with the adsorption energy less than ca. 65 kJ mol⁻¹. In total, we found very strong dependence of water adsorption energy on the water coverage, even at very low coverages. This result can hardly be related solely to the repulsive lateral interaction between water dimers. Most likely, long-range coupling of the adsorbates via the Fe₃O₄ support is responsible for the observed strong dependence of water binding energy on the coverage, particularly in the low coverage limit.

With this, we for the first time resolved the microscopic structure of the water-related species formed on magnetite in the lowest coverage limit and obtained comprehensive spectroscopic information on the different water-

related species formed in a broad range of coverage and temperature conditions. Complementary, we obtained highly accurate energy values for this process under isothermal conditions that can serve as high quality benchmarks for theoretical calculations.

6.5 Experimental section

All experiments were performed at the Fritz-Haber-Institut of the Max-Planck-Society in Berlin, Germany. The adsorption experiments were done in an ultrahigh vacuum (UHV) single crystal adsorption calorimetry (SCAC) apparatus based on molecular beam techniques described in detail elsewhere.^[196] An effusive doubly differentially pumped multi-channel array source was employed to produce water beam (Deuterium oxide “100”, min. 99.96 atom. % D, Sigma-Aldrich) at the intensity $1.0 \cdot 10^{14}$ molecules $\text{cm}^{-2} \text{ s}^{-1}$ ($\sim 5 \cdot 10^{-7}$ mbar on the sample surface). The beam was cut into pulses of 266 ms length by a remote-controlled chopper, after that the gas impinged on a sample prepared on an ultrathin (1 μm) single crystal (Pt(111), FeO(111) grown on Pt(111) or Fe₃O₄(111) grown on Pt(111)). The small change in the temperature of the sample caused by adsorption of water was measured by a heat detector, consisting of a 9 μm -thick β -polyvinylidene fluoride (β -PVDF) pyroelectric ribbon coated with Au on both sides. The energy calibration was performed by applying pulses of laser light (HeNe, Linos, wavelength 632.8 nm, 5mW), which passes through the same path as the molecular beam and is chopped in a way identical to the molecular flux. Simultaneously, the fraction of the molecules adsorbed in a single beam pulse (i.e., the sticking coefficient) was measured by the modified King-Wells method with a quadrupole mass spectrometer (QMS Hiden, HAL 301/3F) in a non-line-of-sight geometry.

The IRAS data were acquired in the molecular beam/IRAS UHV apparatus described in detail elsewhere.^[151] A vacuum Fourier-Transform Infrared (FT-IR) spectrometer (Bruker IFS 66v/S) with a spectral resolution of 2 cm^{-1} was used with a mid-infrared (MIR) polarizer to select the p-component of the IR light. Water (Deuterium oxide “100”, min. 99.96 atom. % D, Sigma-Aldrich; Deuterium oxide ¹⁸O, 95 atom. ¹⁸O, 99 atom. D, Sigma-

Aldrich; ultrapure water, deionized and distilled H₂O) was supplied via an effusive doubly differentially pumped molecular beam to exactly control the exposure. Water were adsorbed in the temperature range between 120 and 500 K, acquisition of the spectra was performed at the dosing temperature.

The Fe₃O₄/Pt(111) model catalyst was prepared by growing a thin (~50 Å) Fe₃O₄(111) film on a Pt(111) single crystal by repeated cycles of Fe (99.995%, Alfa Aesar) physical vapor deposition at a substrate temperature of ~120 K and subsequent oxidation at 875 K (see [198] for details). The evaporation rate of Fe (~1 Å/min) was calibrated by a quartz-crystal microbalance (QCM, Sigma instruments). The quality of the oxide film was checked by LEED. An ultrathin FeO(111) film was also grown on a Pt substrate by depositing 1 ML Fe at room temperature and annealing in 5·10⁻⁷ mbar O₂ atmosphere at 1000 K. The Pt(111) single crystal was cleaned prior to use by repeated cycles of Ar⁺ ion bombardment at room temperature, annealing at 1200 K and oxidation in 1·10⁻⁶ mbar O₂ at 1000 K.

Adsorption energy is defined as a measured heat release at a certain sample temperature minus contribution of the gas cooling from the temperature in the molecular beam to the sample temperature. Constant-volume heat capacity of water in the temperature range 120-300 was assumed to be constant.

6.6 Supporting information

6.6.1 Sticking coefficients

Two types of a sticking coefficient are determined in the experiment. The short-time sticking coefficient is derived over the time scale of molecular beam pulses and is used to calculate molar adsorption energy. The long-time sticking coefficient is in turn integrated over the whole time period between two neighboring pulses and serves as a measure for obtaining the surface coverage.

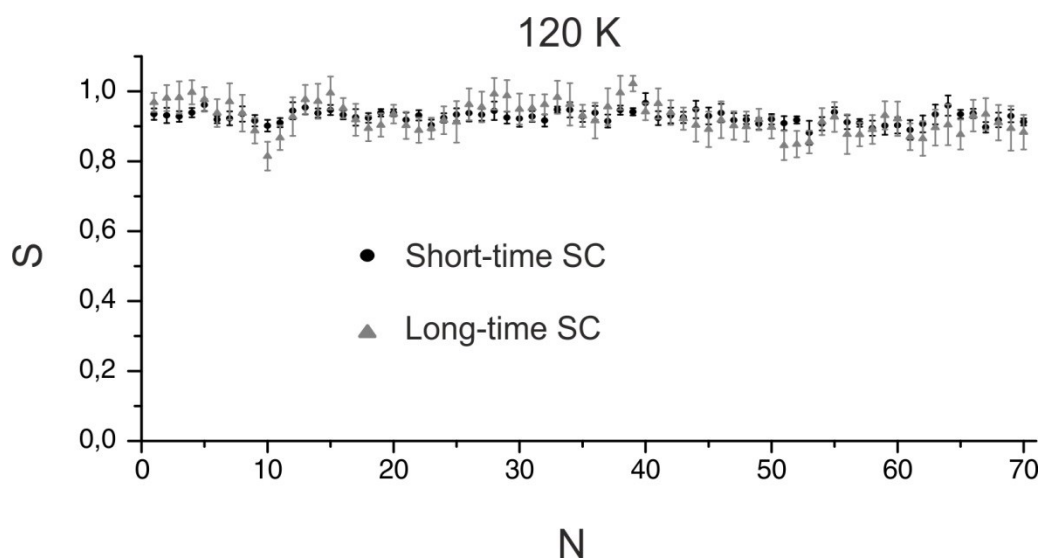


Figure 6.11 Short- and long-time sticking coefficients of water on $\text{Fe}_3\text{O}_4(111)$ as a function of the pulse number at 120 K. The data points are averages of about 10 independent measurements; the error bars are the average of the mean.

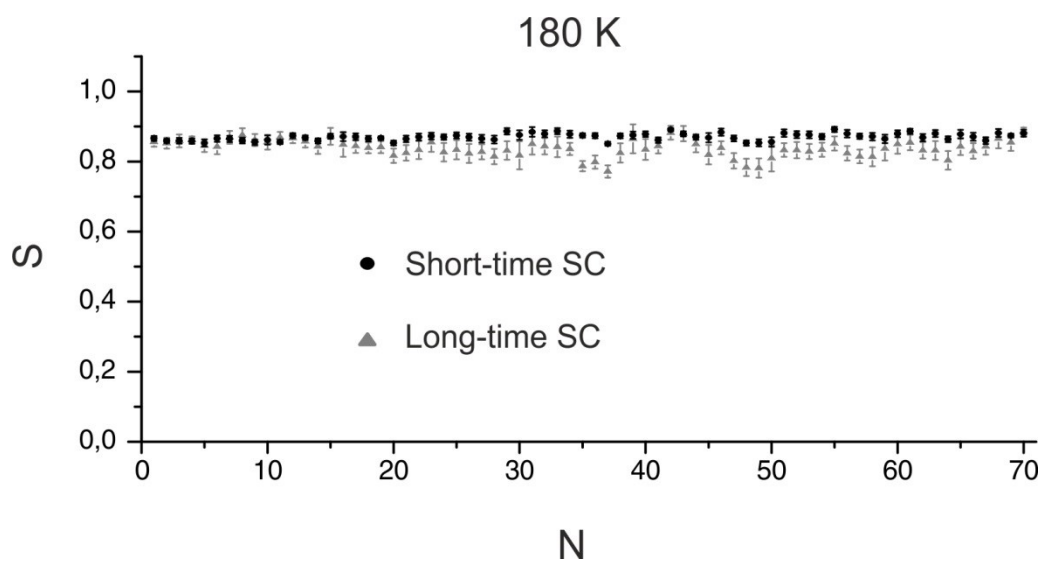


Figure 6.12 Short- and long-time sticking coefficients of water on $\text{Fe}_3\text{O}_4(111)$ as a function of the pulse number at 180 K. The data points are averages of about 10 independent measurements; the error bars are the average of the mean.

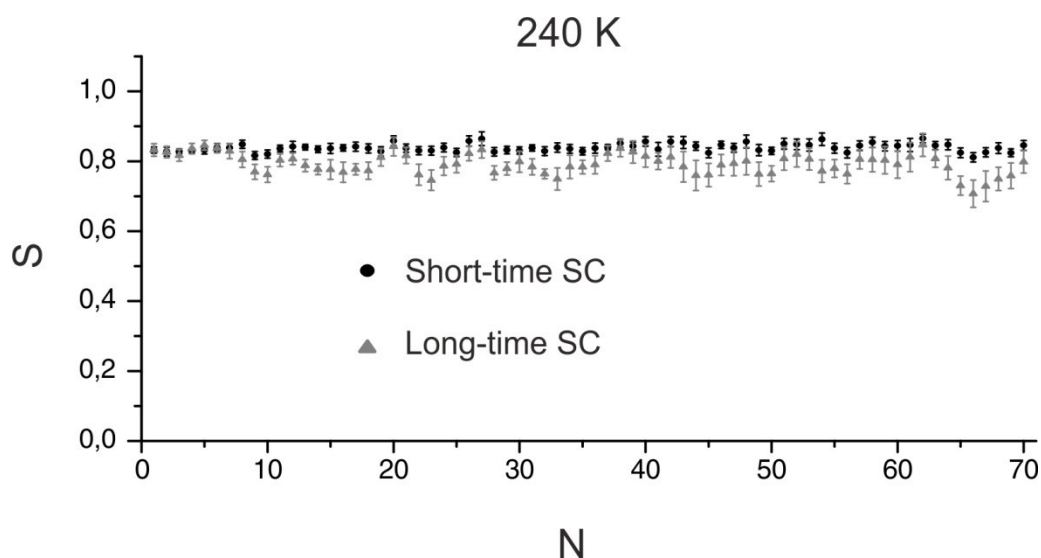


Figure 6.13 Short- and long-time sticking coefficients of water on $\text{Fe}_3\text{O}_4(111)$ as a function of the pulse number at 240 K. The data points are averages of about 10 independent measurements; the error bars are the average of the mean.

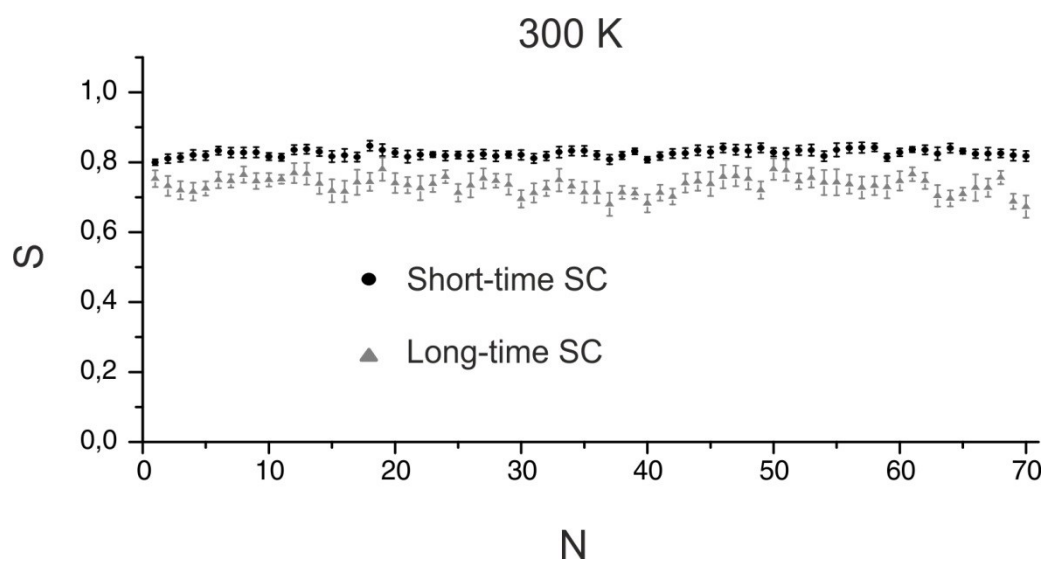


Figure 6.14 Short- and long-time sticking coefficients of water on $\text{Fe}_3\text{O}_4(111)$ as a function of the pulse number at 300 K. The data points are averages of about 10 independent measurements; the error bars are the average of the mean.

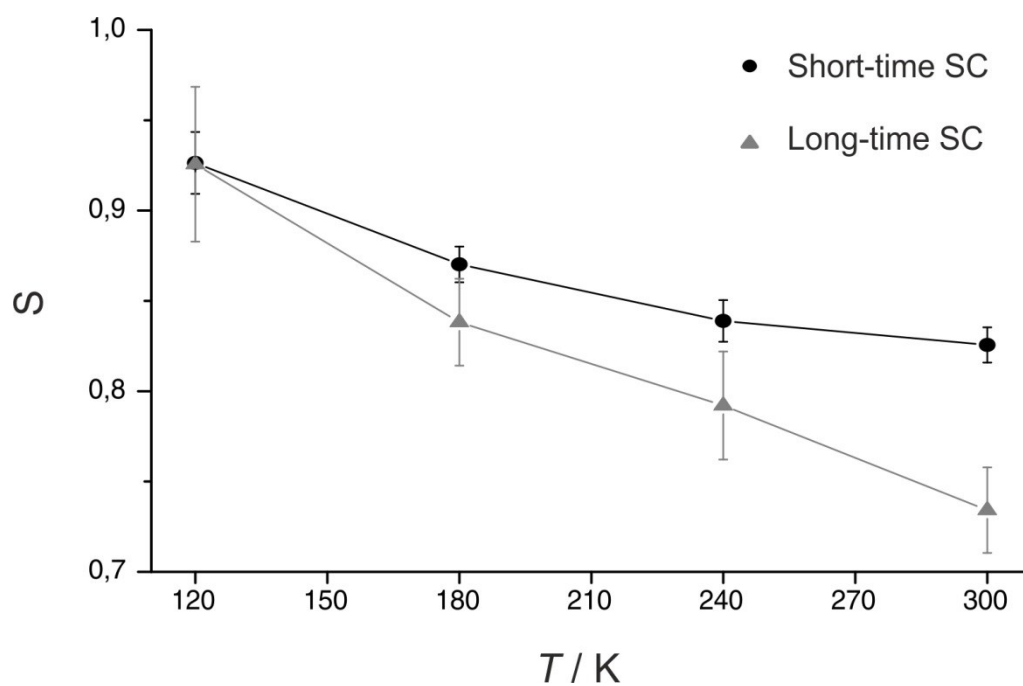


Figure 6.15 Average short- and long-time sticking coefficients of water on $Fe_3O_4(111)$ as a function temperature.

6.6.2 Infrared spectra

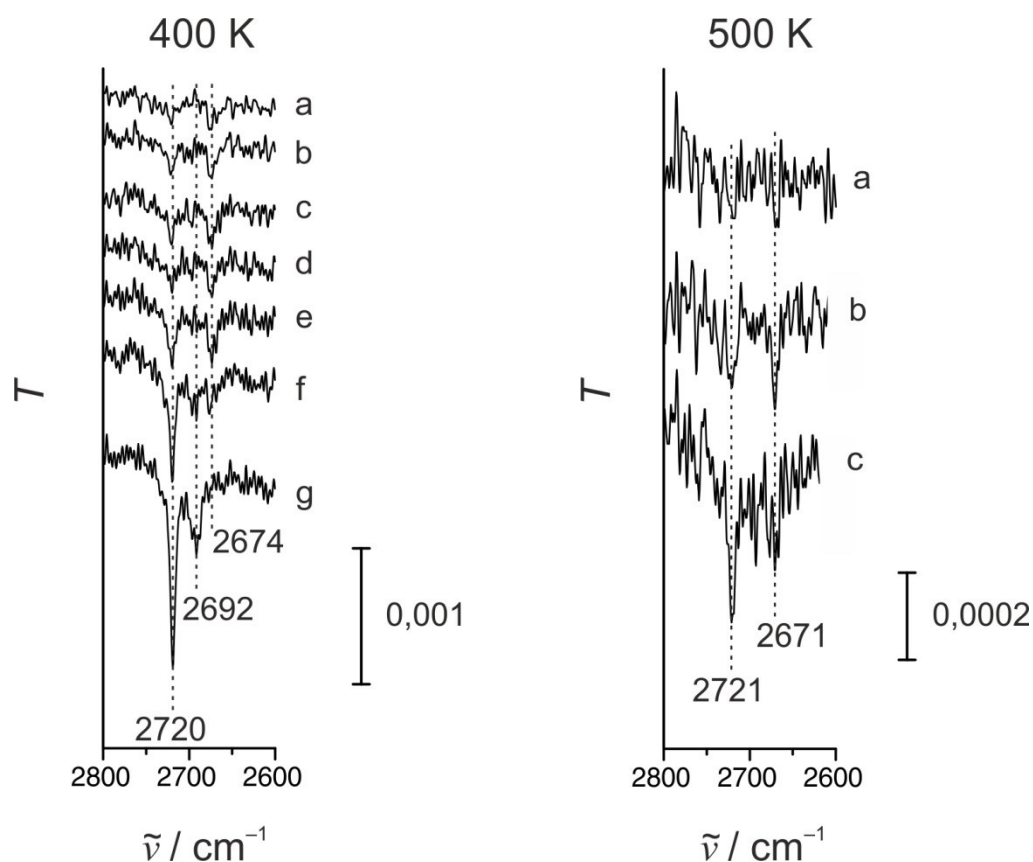


Figure 6.16 Infrared spectra of surface species on $\text{Fe}_3\text{O}_4(111)$ measured at 400 K (on the left) and 500 K (on the right). The spectra are designated as following: at 400 K the spectra a-d were recorded after D_2O exposure of 0.13, 0.25, 0.38, and 0.50 L correspondingly; the spectra e-g were collected under running molecular beam with the flux of $1.1 \cdot 10^{13}$, $5.7 \cdot 10^{13}$ and $5.7 \cdot 10^{14}$ molecules $\text{cm}^{-2} \text{s}^{-1}$ respectively. On the contrary, at 500 K all the spectra a-c were measured upon continuous exposing with the flux of $1.1 \cdot 10^{13}$, $5.7 \cdot 10^{13}$ and $5.7 \cdot 10^{14}$ molecules $\text{cm}^{-2} \text{s}^{-1}$.

§ 7 Adsorption energy of water on Fe₃O₄(100) by microcalorimetry[□]

7.1 Abstract

We employ single-crystal adsorption calorimetry to characterize interaction of water with a well-defined epitaxial Fe₃O₄(100)/Pt(100) substrate. At 120 K, initial adsorption energy amounts to 65±1 kJ mol⁻¹ and is about 30% lower compared to the corresponding value on Fe₃O₄(111) reported before. Also temperature-dependent measurements of the trapping probability indicate that (100) surface of magnetite is less reactive than (111) one. We discuss the structure-activity relationship obtained in terms of Lewis acid properties of the coordinatively unsaturated cation sites present at the oxide surfaces.

7.2 Introduction

Surface properties of magnetite Fe₃O₄ have attracted considerable interest both in catalysis and materials science research.^[199-201] Particularly, this naturally occurring oxide was proved to be reactive towards many chemicals and consequently has a potential of being utilized as a cheap heterogeneous catalyst.^[117, 145, 148, 202, 203] In fact, iron oxide-based catalysts are already used in production of styrene and hydrogen via the water-gas shift reaction (WGSR).^[46, 204] The latter process is of special technological significance since it necessarily accompanies such paramount large-scale industries as ammonia and methanol synthesis and is furthermore needed for fuel cells applications.^[47, 205] Two main reaction mechanisms are considered to underlie the heterogeneously catalyzed WGSR.^[46, 47] In the associative mechanism, adsorbed water and carbon monoxide form intermediate surface complexes basically following the Langmuir–Hinshelwood kinetics. In contrast, the so called redox mechanism refers to the Mars–van Krevelen reaction type, where oxide surface is alternatively reduced and oxidized back by CO and H₂O respectively. For both pathways, adsorption of water

[□] The following chapter is due for submission to Chemical Physics Letters by Petr Dementyev, Stephanie Hemmingson, Jan Seifert, Swetlana Schauer mann, and Hans-Joachim Freund

represents one of the most important elementary steps, and it is commonly believed that the WGSR is driven by surface hydroxyl groups.^[206]

Although interaction of water with the most abundant (111) and (100) magnetite surfaces has been extensively addressed by various surface sensitive techniques, the data available are somewhat contradictory, particularly in terms of relative reactivity of the two terminations. Photoelectron spectroscopy measurements with natural Fe_3O_4 crystals indicated that hydroxylation of both (111) and (100) surfaces is accelerated by increasing water coverage leading to sharp pressure dependence.^[50, 51, 141] Concurrently, UHV studies with epitaxial $\text{Fe}_3\text{O}_4(111)$ films revealed instant water dissociation on regular surface sites followed by molecular adsorption upon monolayer completion.^[48, 143] These findings have been recently revised by our molecular beam experiments supported by DFT calculations.^[194] Specifically, surface chemistry of water on $\text{Fe}_3\text{O}_4(111)$ was shown to be rather facile and yield peculiar dimer species. Also for the $\text{Fe}_3\text{O}_4(100)$ surface, there are multiple evidences of water chemisorption under UHV conditions with both thin film and bulk samples.^[139, 148] Accordingly, comparative investigation of the two magnetite surfaces using the same experimental approach seems to be highly worthwhile.

In this letter, we present single-crystal adsorption calorimetry (SCAC) measurements of water adsorption on an epitaxial $\text{Fe}_3\text{O}_4(100)$ substrate and correlate the results with those reported for $\text{Fe}_3\text{O}_4(111)$. As compared to bare Pt(100), water was found to chemisorb on $\text{Fe}_3\text{O}_4(100)$ at 120 K exhibiting 20 kJ mol^{-1} higher adsorption energy. Similar to $\text{Fe}_3\text{O}_4(111)$, adsorption energy in the monolayer decreases gradually with surface coverage. However, adsorption behavior on the two magnetite surfaces is quantitatively very different. A trapping probability on $\text{Fe}_3\text{O}_4(100)$ rapidly diminishes with temperature, while it remains high on $\text{Fe}_3\text{O}_4(111)$. Thus, the (100) surface of magnetite has lesser affinity to water than the (111) one. This structure-reactivity relation is rationalized on the basis of existing surface models, including the recently upgraded structure of $\text{Fe}_3\text{O}_4(100)$.^[131]

7.3 Experimental details

The SCAC measurements were performed in a two-chamber UHV instrument at the Fritz Haber Institute in Berlin, Germany.^[30] Fe₃O₄(100) films were prepared by physical vapor deposition on ultrathin Pt(100) samples according to the adapted recipe by Davis *et al.*^[140] The Pt(100) single crystal was preliminary cleaned by cycles of Ar⁺ sputtering (1 keV) and UHV annealing at 1200 K (5 min). At room temperature, a 3 nm Fe (99.995%, Alfa Aesar) buffer layer was deposited under UHV at a deposition rate of $\sim 1 \text{ \AA min}^{-1}$ followed by oxide growth in O₂ ambient with a partial pressure of $1 \cdot 10^{-6}$ mbar for 30 min. Afterwards, three successive annealing steps were carried out (20 min in UHV at 880 K; 20 min in UHV at 1080 K; 5 min in $5 \cdot 10^{-7}$ mbar O₂) until a $(\sqrt{2} \times \sqrt{2})R45^\circ$ reconstruction was seen by LEED. Adsorption experiments were performed by means of a pyroelectric heat detector and a quadrupole mass-spectrometer in the temperature range 120 – 300 K. 266 ms long molecular beam pulses of D₂O (Deuterium oxide “100”, min. 99.96 atom. % D, Sigma-Aldrich) with a repetition rate of 0.5 Hz were created via an effusive multi-channel array source kept at room temperature. In the course of the paper, the heat release measured at certain calorimeter temperature is represented as adsorption energy which does not include the heat associated with a temperature difference between incoming gas-phase molecules and adsorbed surface species. The trapping probability was determined from the sticking coefficient measurements by accounting the fraction of scattered molecules within the first 290 ms.

7.4 Results and Discussion

Under UHV conditions (pressure $\sim 10^{-10}$ mbar) water vapor is known to readily precipitate to ice films when cooled down below 130 K.^[207] We performed SCAC experiments at 120 K in order to observe the heat of multilayer condensation and thereby discriminate completion of a monolayer. Figure 7.1 shows the adsorption energy of water on a Fe₃O₄(100) substrate in comparison with that on pristine Pt(100). Here, the x-axis refers to the absolute number of adsorbed water molecules per surface area. This

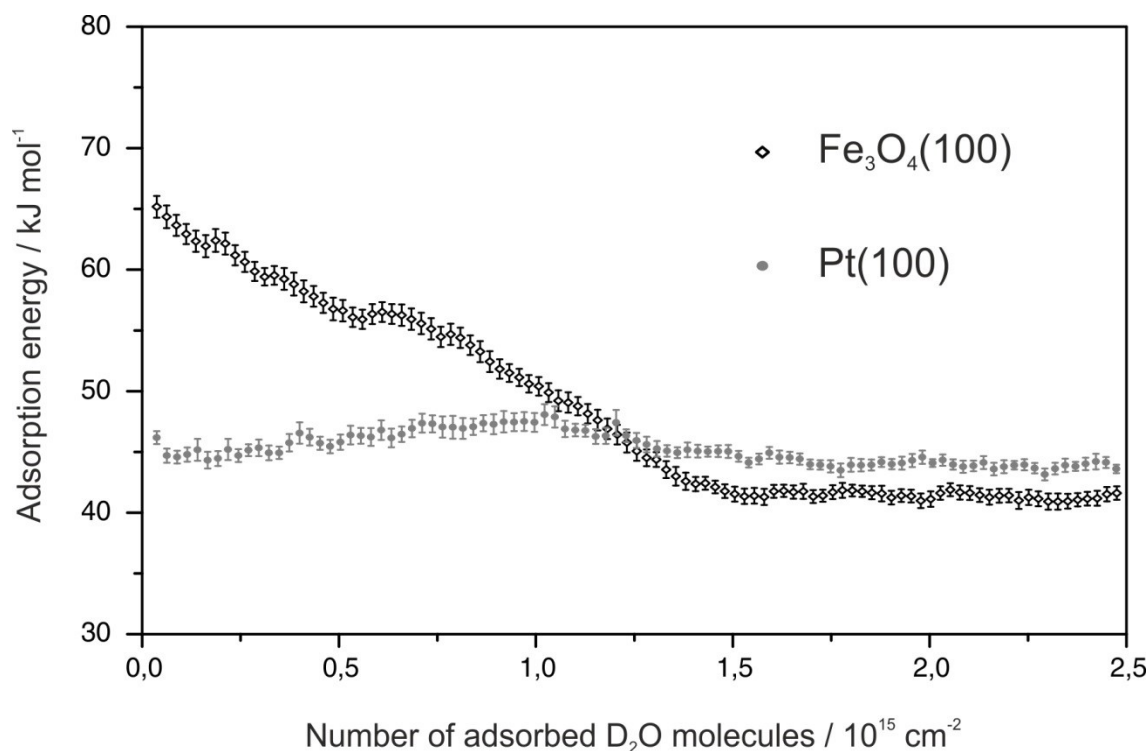


Figure 7.1 Adsorption energy of D_2O as a function of the number of adsorbed molecules on bare $Pt(100)$ and $Fe_3O_4(100)/Pt(100)$ measured at 120 K. The data points are averages of 12–14 independent measurements; the error bars show the error of the mean.

quantity allows for comparison of different surfaces regardless of their particular atomic structure and can be easily converted to the surface coverage provided the densities of surface atoms are known.

Similar to the previous SCAC experiments with $Pt(111)$, adsorption energy of water on bare $Pt(100)$ exhibits a weak dependence on the number of adsorbed molecules which is consistent with the physisorption mechanism.^[194, 197] In contrast, adsorption energy on $Fe_3O_4(100)$ shows two pronounced regimes clearly separating monolayer and multilayer adsorption. The constant adsorption energy of $\sim 42 \text{ kJ mol}^{-1}$ observed at coverages exceeding $1.5 \cdot 10^{15} \text{ molecules cm}^{-2}$ corresponds to the adsorption in the second and subsequent layers, i.e. when no oxide surface is accessible for the incoming water molecules. At high coverage, the same situation is also reached on the $Pt(100)$ substrate, though the transition from monolayer to multilayer is hardly distinguishable. The small discrepancy in the heat of

multilayer condensation obtained on the two kinds of surfaces is caused by an error in the substrate reflectivity which is measured *in situ* and strongly depends on the film thickness.

In the zero-coverage limit, the adsorption energy on the iron oxide amounts to 65 ± 1 kJ mol⁻¹, and in the whole range of the number of adsorbed molecules it is appreciably higher than on the metal. In agreement with previous studies, this observation indicates a chemical reaction taking place upon interaction of water with the magnetite surface. Indeed, early TPD experiments with water on epitaxial Fe₃O₄(100) films showed three adsorption states in the first layer with approximately equal concentrations at saturation and desorption maxima appearing at 225, 280, and 300 K.^[147] Recently, adsorption of water on a Fe₃O₄(100)/Mo(100) substrate was studied with HREELS, LEED, and UPS.^[139] At low temperature, two coexisting loss peaks at 456 and 420 meV were found which correspond to the terminal OH bonds and hydrogen-bonded water, respectively. The latter vibrational band disappears upon heating which indicates desorption of the molecularly adsorbed species. As shown in the STM and LEIS study by Diebold and co-workers, only adsorbed H atoms exist on Fe₃O₄(100) after water exposure at 300 K.^[148] These species represent a specific type of surface hydroxyl groups which involve lattice oxygen atoms. No associated OH groups arising from water molecules were found, what is indicative of their efficient removal at room temperature in UHV. The authors concluded that chemisorption of water on Fe₃O₄(100) includes formation of surface hydroxyl groups which can further react with each other and/or with the oxide lattice.

Surface reactions of OH groups on Fe₃O₄(100) are likely to be kinetically suppressed at such low temperatures as 120 K. As shown in Figure 7.1, the monolayer is saturated at approximately the same coverage as on Pt, therefore easily desorbing products are unlikely formed. According to the HREELS data, water dissociation on the oxide is also to some extent hindered, i.e. hydroxyl species are most likely accommodated together with intact molecules.^[139] This is confirmed by higher adsorption energy observed at elevated temperatures, namely, at 180 K the initial adsorption energy

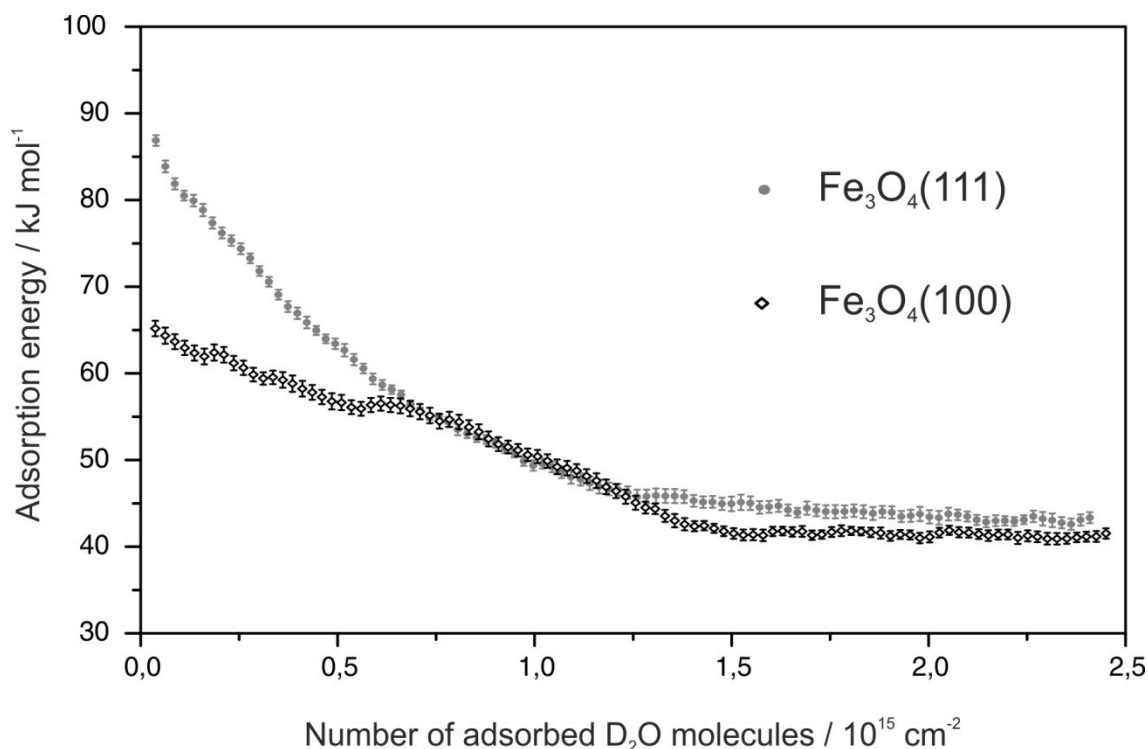


Figure 7.2 Comparison of the differential adsorption energy of D₂O on Fe₃O₄(100) and Fe₃O₄(111) at 120 K.

equals to 73 ± 2 kJ mol⁻¹. A similar effect was found recently on the Fe₃O₄(111) substrate, where the surface reaction of water is partially inhibited at 120 K and its adsorption energy increases by almost 10 kJ mol⁻¹ for higher temperatures.^[194] On Fe₃O₄(111), water was shown to react bimolecularly, yielding stable dimer-like species which have two anchoring points to the surface. Figure 7.2 illustrates quantitative comparison of the interaction of water with the two magnetite surfaces. The SCAC data reveal clearly that Fe₃O₄(100) has lower affinity to water than Fe₃O₄(111): initial adsorption energy on the bare surfaces differs by ca. 20 kJ mol⁻¹. In order to understand this activity trend we refer to the atomic structure of the Fe₃O₄ surfaces of interest.

Fe₃O₄ has an inverse spinel structure, in which oxygen atoms are packed into a fcc sublattice with the interstitial sites being occupied by iron; the tetrahedral positions contain Fe³⁺, while the octahedral sites are populated by equal amounts of Fe³⁺ and Fe²⁺.^[175] Theoretically, multiple terminations are possible for both (111) and (100) surfaces.^[208] In our previous work on Fe₃O₄(111), only one structure describes satisfactorily the observed

properties of adsorbed water – the so called $\text{Fe}_{\text{oct}2}$ termination.^[194] For the $\text{Fe}_3\text{O}_4(100)$, an equilibrium structural model has been recently proposed in a combined IV-LEED, STM and DFT study by Bliem *et al.*^[131] The $(\sqrt{2}\times\sqrt{2})\text{R}45^\circ$ reconstructed B termination was shown to be stabilized by an ordered array of subsurface cation vacancies (SCV), where two octahedrally coordinated iron cations are missing in the third layer, while one iron atom appears as an interstitial in the second layer. The $\text{Fe}_{\text{oct}2}$ -terminated $\text{Fe}_3\text{O}_4(111)$ and SCV-terminated $\text{Fe}_3\text{O}_4(100)$ structures are depicted schematically in Figure 7.3. Both surfaces expose all possible types of the oxide constituents. However, these adsorption sites are not equivalent from the chemical point of view, particularly in terms of their acid-base properties. In principle, the ions existing in the magnetite crystal structure can work both as Brønsted bases (O^{2-} anions) and Lewis acids (Fe^{2+} and Fe^{3+} cations). Since water has a pronounced amphoteric character, its interaction with the iron oxides can be considered as an acid-base reaction. While the proton affinity of the oxygen in metal oxides is always very high,^[209] the electron-acceptor strength of the iron surface sites seems to be strongly dependent on the neighboring atomic arrangement.

The $\text{Fe}_{\text{oct}2}$ termination is a relaxed bulk truncation along the $[111]$ direction by the so called mix-trigonal layer. It exposes $\frac{1}{4}$ ML of Fe^{3+} in the tetrahedral positions and $\frac{1}{4}$ ML of the octahedral cations over a closed-packed hexagonal array of oxygen atoms whose density defines 1 ML ($\sim 1.3 \cdot 10^{15} \text{ cm}^{-2}$). Both types of iron atoms also form hexagonal periodic structures with the same $\sim 6 \text{ \AA}$ unit cell which gives rise to a macroscopic surface concentration of $\sim 3.3 \cdot 10^{14} \text{ cm}^{-2}$. Correspondingly, the $\text{Fe}_3\text{O}_4(111)$ unit cell contains two different cation sites and four anion sites, one of which is not equivalent to the other three (Fig. 7.3). On this surface, water was shown to form a single dimer-like species per unit cell. According to the quantum chemical calculations, one molecule is dissociated into an OH group bound to the octahedral iron and a proton on the neighboring oxygen site (the one which is more distant from the cation). The second water molecule has no direct contact with the oxide surface and is only hydrogen-bonded with the first one. Thus, water reaction with $\text{Fe}_3\text{O}_4(111)$ does include

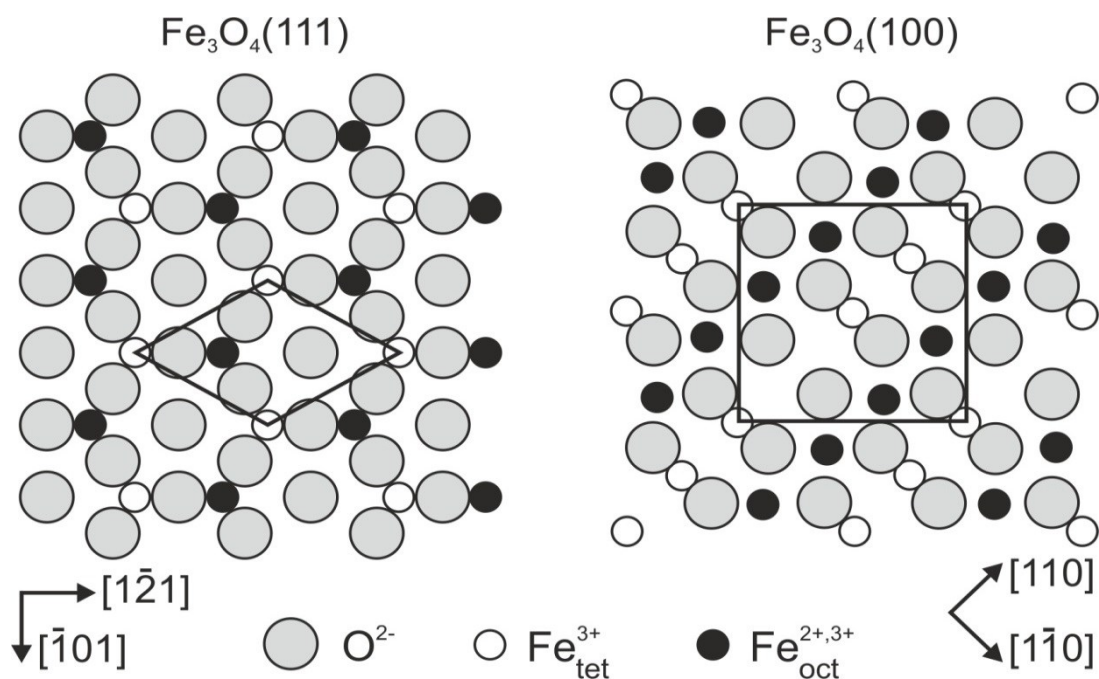


Figure 7.3 Top views of the $Fe_{oct2}-Fe_3O_4(111)$ and SCV- $Fe_3O_4(100)$ structural models. The depicted are (1×1) hexagonal $Fe_3O_4(111)$ and $(\sqrt{2} \times \sqrt{2})R45^\circ$ $Fe_3O_4(100)$ surface unit cells.

the interaction with undercoordinated cation sites. The coordination number of the exposed octahedral iron is 3, i.e. it is threefold coordinatively unsaturated. The iron atoms in the tetrahedral positions are only singly undercoordinated and do not participate in the reaction at low coverage.

As mentioned above, the newly elaborated SCV model of the $Fe_3O_4(100)$ surface properly describes the well-established $(\sqrt{2} \times \sqrt{2})R45^\circ$ reconstruction and other characteristics of the oxide surface, e.g. high stability of deposited metal adatoms. In the SCV structure, the topmost atomic array is based on the so-called B layer perpendicular to the $[100]$ bulk direction with the modified A layer underneath. The B layer consists of oxygen and the octahedral iron atoms forming distorted rows in the $[110]$ direction (Fig. 7.3). The reconstruction was proved to be caused by cation vacancies in the third layer and interstitial iron atoms appearing in the second layer.^[131] This A layer is composed only of the tetrahedrally coordinated cations, and the interstitials lower its fourfold bulk symmetry producing the $(\sqrt{2} \times \sqrt{2})R45^\circ$ periodicity. The reconstructed unit mesh is $8.4 \times 8.4 \text{ \AA}^2$ in size and exposes 8 oxygen atoms and 4 octahedral iron atoms with 3 coordinatively saturated

tetrahedral cations beneath (including the interstitial). Similar to $\text{Fe}_3\text{O}_4(111)$, initial water reaction with $\text{Fe}_3\text{O}_4(100)$ was proposed to involve the iron in the octahedral positions.^[148] However, the coordination number of the octahedral cations on the $\text{Fe}_3\text{O}_4(100)$ surface equals to 5, i.e. these sites are less undercoordinated compared to $\text{Fe}_3\text{O}_4(111)$. Due to the screening effect, the iron sites on the two magnetite surfaces should possess different electron affinity obeying the order $\text{Fe}_3\text{O}_4(100) < \text{Fe}_3\text{O}_4(111)$. In other words, $\text{Fe}_3\text{O}_4(100)$ surface should have weaker Lewis acidic character than $\text{Fe}_3\text{O}_4(111)$, which is in line with the measured characteristics of their interaction with strong electron-donor species – the forming hydroxides.

Despite the simplicity of such acid-base approach, the importance of the electrophilic properties of the surface cation sites is further supported by the trapping probability data. Figure 7.4 shows the average trapping probability of water on both magnetite substrates as a function of temperature. Since the trapping probability weakly changes with surface coverage, it indicates precursor-mediated adsorption and can be considered as a probability of water molecules to be trapped by the reactive iron sites. The trapping probability clearly differs for $\text{Fe}_3\text{O}_4(100)$ and $\text{Fe}_3\text{O}_4(111)$, amounting, for instance, at room temperature to 0.48 and 0.83, respectively. In contrast to the SCAC measurements which deal with energetic effects of the overall chemical reactions, the trapping probability probes only the primary adsorption process. Thus, the observed temperature dependence directly reflects the difference in water affinity between the surface iron sites on $\text{Fe}_3\text{O}_4(100)$ and $\text{Fe}_3\text{O}_4(111)$. Detailed mechanistic understanding of the water chemisorption on $\text{Fe}_3\text{O}_4(100)$ as well as reactivity relationships between the two surfaces need further spectroscopic and theoretical investigations.

7.5 Conclusions

SCAC was for the first time employed for a comparative chemisorption study on different surface planes of an oxide material. Differential adsorption energy of water was measured on the well-defined thin $\text{Fe}_3\text{O}_4(100)$ film as well as on the pristine $\text{Pt}(100)$ surface. At 120 K, initial adsorption energy on the oxide and the metal amounts to 65 ± 1 and 46 ± 1 kJ mol⁻¹, respectively. In

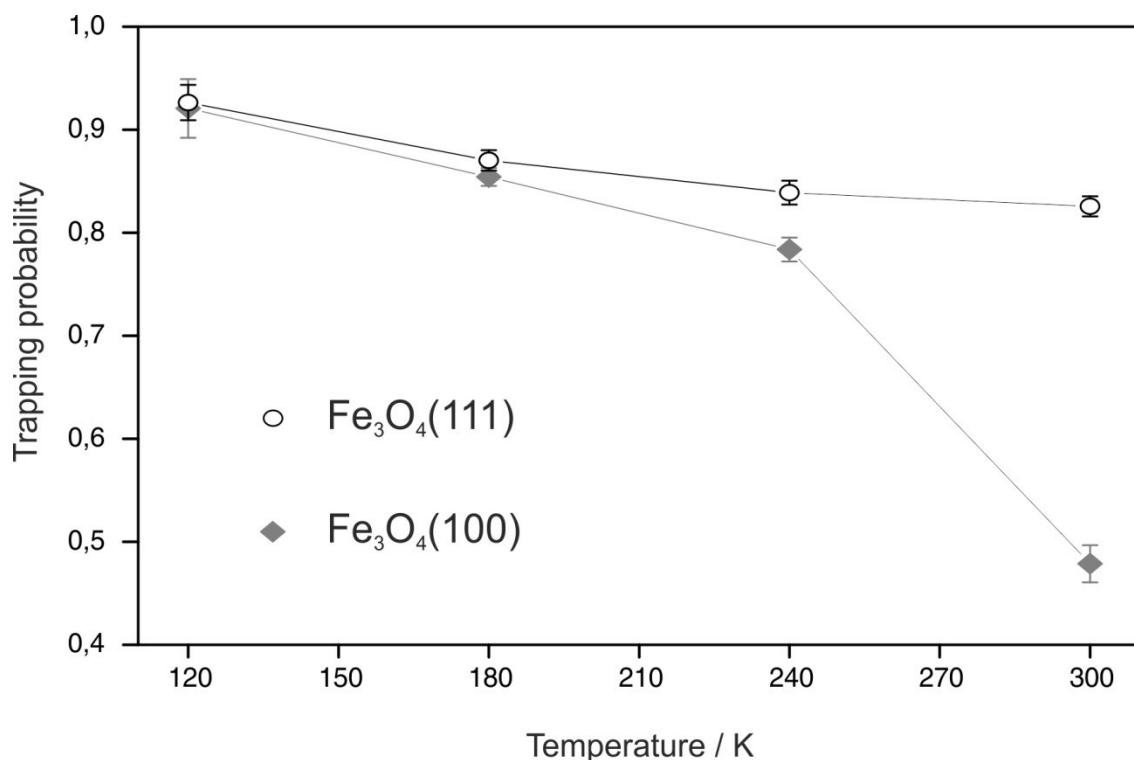


Figure 7.4 Trapping probability of D_2O on $Fe_3O_4(100)$ and $Fe_3O_4(111)$ as a function of temperature. The data points are averages over 10–15 experiments consisting of multiple pulse measurements.

contrast, water was previously shown to interact with the $Fe_3O_4(111)$ substrate with the adsorption energy of $87 \pm 1 \text{ kJ mol}^{-1}$. The present work unambiguously evidences that water chemistry on the iron oxide crucially depends on a particular surface plane exposed. The results obtained demonstrate that adsorption of water on $Fe_3O_4(100)$ is less favorable than on $Fe_3O_4(111)$.

We rationalize the lower affinity to water observed on $Fe_3O_4(100)$ in terms of weaker Lewis acidity of its surface cation sites which is caused by a lesser degree of the coordination unsaturation. It is noteworthy that on both oxide surfaces adsorption energy of water gradually changes with the surface coverage. Such effects are as a rule too underestimated in traditional desorption-based experiments and may misrepresent the strength of gas-surface interactions. Hence, direct calorimetric data have a potential to advance heterogeneous chemistry and catalysis research.

§ 8 Final conclusions and outlook

In this work, single-crystal adsorption calorimetry (SCAC) was employed to investigate energetic effects emerging upon interaction of gaseous species with catalytically active solid surfaces. The combination of the precise quantitative technique with well-defined model substrates enabled comparative studies to be conducted and structure-activity relationships to be established. Two independent problems highly relevant for modern heterogeneous catalysis have been thoroughly examined with the help of the molecular beam approach. The first part of the thesis explores adsorption of chiral organic compounds on chirally-modified metal surfaces, while surface chemistry on thin metal oxide films constitutes the second part of the study.

Two model modifiers R-1-(1-naphthyl)ethylamine (NEA) and S-2-methylbutanoic acid (MBA) were employed to impart chirality to Pt(111), and stereospecificity of the substrates obtained was tested by adsorption of enantiopure propylene oxide (PO). Differential adsorption energy of both PO enantiomers was measured as a function of the modifiers coverage. On NEA modified surfaces, adsorption energy was found to be strongly altered compared to bare Pt(111), indicating high affinity of the incoming PO molecules to NEA species. Such a behavior agrees with the one-to-one mechanism of chirality induction, i.e. when modifier molecules form docking complexes with prochiral and chiral adsorbates. In contrast, MBA species were shown to only sterically affect PO adsorption, consistent with the templating mechanism of chirality induction. Low-temperature SCAC data revealed no enantioselectivity in adsorption of R- and S-PO on both chirally-modified surfaces either in terms of the interaction strength or in terms of the absolute number of the accommodated probe adsorbates. These findings complement previously reported TPD titration experiments and point to the kinetic nature of the stereodifferentiation effects observed before.

Two epitaxially prepared $\text{Fe}_3\text{O}_4(111)$ and $\text{Fe}_3\text{O}_4(100)$ films were investigated towards adsorption of water. As opposed to pristine Pt surfaces, the differential adsorption energy measured clearly indicated chemical transformations occurring on both magnetite substrates. Vibrational

spectroscopy measurements in combination with quantum chemical calculations allowed for disclosing the reaction mechanism. On $\text{Fe}_3\text{O}_4(111)$, water was shown to form stable dimer-like species existent even at low surface coverages and high temperatures. Hence, the previously accepted adsorption model involving the formation of individual hydroxyl groups was unambiguously disproved in the present work. Despite interaction of water with magnetite was proved to be fully reversible, SCAC data substantially differ from those deduced in early adsorption-desorption experiments. Adsorption energy of water on the oxide surfaces was demonstrated to be strongly coverage-dependent which explains the failure of the TPD and EAI evaluations. Furthermore, adsorption of water on $\text{Fe}_3\text{O}_4(111)$ was found to be more favorable than on $\text{Fe}_3\text{O}_4(100)$. As quantified by SCAC, the interaction strength on the former surface exceeds that on the latter one by almost 30 %. This structure-activity relationship was rationalized on the basis of Lewis acid properties of the surface cation sites which have different degree of unsaturation on the two magnetite substrates.

Thus, the adsorbate-surface systems probed in the present study range from weakly interacting, i.e. molecular adsorption on chiral surfaces, to strongly interacting ones, i.e. water surface chemistry on the iron oxide. In both cases, isothermal SCAC measurements carried out were able to yield adsorption energy and absolute surface uptakes for different adsorption states. When comparing similar adsorbates or adsorbents, one could easily detect energy differences as subtle as 5 kJ mol^{-1} . On the contrary, adsorption energetics obtained earlier by indirect techniques turns out to be far away from the absolute calorimetric values. Accordingly, adsorption calorimetry on two-dimensional substrates seems to be a very promising tool in studying heterogeneous reactions, especially when coupled with facilities for preparation of well-defined model catalysts. For instance, surface chemistry of such important reagents as hydrogen, water, carbon dioxide, methane, etc. can be potentially addressed on a variety of thin metal oxide films. Quantitative information on the gas-solid interaction strength can be helpful in pursuing the rational catalyst design.

Appendix

The given dissertation is primarily based on the experimental work performed at the SCAC machine. In principle, this versatile instrument can be applied to a variety of adsorbing gaseous species as well as diverse solid surfaces. Several projects have been worked out during my PhD stay apart from the results presented above. First of all, I have extensively attempted to exploit the calorimeter for catalytic activity tests and so probed different model substrates spanning bare oxides, supported metal nanoparticles, and inverse oxide/metal model catalysts. The latter are especially attractive models, where reactant can access defect sites on the oxide particles, regular metal sites, as well as the metal oxide interface.^[210] Thus, monolayer-thick FeO islands grown on Pt(111) were previously shown to be active in catalyzing water splitting, carbon monoxide oxidation, and even the water-gas shift reaction under UHV conditions.^[211-214] However, room-temperature SCAC experiments did not reveal any appreciable affinity of 0.3, 0.45, and 0.6 ML FeO/Pt(111) to water, as opposed to the magnetite surfaces discussed above. This is most likely due to the size of the FeO islands which is known to strongly depend on preparation conditions and could not be properly reproduced without morphology characterization. On the other hand, CO was shown not to affect water adsorption on Fe₃O₄(111) when present at the background pressure of $5 \cdot 10^{-7}$ mbar. No water-gas shift conversion was also found on Pd nanoparticles supported by magnetite at room temperature. Operation of the pyroelectric ribbon is unfortunately limited by its thermal stability therefore high-temperature measurements are hardly feasible.

Further, I performed experiments on surface chemistry of carbon dioxide on magnetite. Nowadays, CO₂ is widely considered to be a promising carbon feedstock. Since CO₂ molecules are very stable, their initial activation seems to be the most important step in the chemical transformation.^[215] Practically, heterogeneous catalysis could be an effective route, and hence CO₂ adsorption on solid surfaces represents a rather intriguing issue.^[216] Unlike alkali and alkaline earth metal oxides which form thermodynamically very

stable carbonates, catalytically useful activation would mean formation of rather labile surface adducts. Inspired by facile water chemistry on iron oxides, I tried to adsorb CO_2 on a $\text{Fe}_3\text{O}_4(111)$ film. As shown in the present thesis, magnetite substrates possess highly electrophilic surface cations which can act as Lewis acid sites towards lone electron pairs of oxygen atoms. Indeed, it turned out that carbon dioxide interacts with the iron oxide under UHV conditions. Specifically, low-temperature SCAC measurements revealed that carbon dioxide transiently adsorbs on magnetite, whereas no energy release was observed on reference FeO and Pt surfaces. Despite the interaction is rather weak, there is quite rich chemistry occurring, as shown by infrared spectroscopy experiments. CO_2 chemisorption on $\text{Fe}_3\text{O}_4(111)$ seems to be strongly kinetically controlled, and its sticking coefficient decreases rapidly from ~ 0.87 at 120 K to 0 at 240 K. Additionally, the sticking coefficient vanishes, when the surface is preliminary exposed to water which indicates competitive adsorption on cation sites. On the contrary, water readily adsorbs on a CO_2 pre-covered substrate, consistent with their relative adsorption energies. This activity has evolved into a separate study being currently conducted in the Molecular Beam group. Similarly, carbon dioxide was shown to adsorb on $\text{Fe}_3\text{O}_4(100)$, albeit this substrate is again less reactive compared to $\text{Fe}_3\text{O}_4(111)$. In 2014, I was involved in a beamtime project at the BESSY synchrotron, where I probed CO_2 adsorption on $\text{Fe}_3\text{O}_4(100)$ by surface-sensitive X-ray photoelectron spectroscopy. As revealed by carbon core level spectra, there are multiple adsorption states coexisting on the timescale of minutes. It means CO_2 transformations are very slow under given conditions, so that only the very first interaction step can be detected by calorimetry. Water was also shown to easily replace carbon dioxide adsorbates from $\text{Fe}_3\text{O}_4(100)$. Perhaps, studying surface chemistry of CO_2 on magnetite would yield some catalytically important findings and eventually give rise to a scientific publication.

List of publications

- *Adsorption energy of water on Fe₃O₄(100) by microcalorimetry*

P. Dementyev, S. Hemmingson, J. Seifert, S. Schauermann, and H.-J. Freund

Chem. Phys. Lett., to be submitted

- *Surface chemistry of water on magnetite: a mechanistic study*

P. Dementyev, C. P. O'Brien, K.-H. Dostert, F. Ivars-Barceló, F. Mirabella, J. Seifert, S. Schauermann, and H.-J. Freund

J. Phys. Chem. C, submitted

- *Water Interaction with Iron Oxides*

P. Dementyev, K.-H. Dostert, F. Ivars-Barceló, C. P. O'Brien, F. Mirabella, S. Schauermann, X. Li, J. Paier, J. Sauer, H.-J. Freund

Angew. Chem. Int. Ed., (2015) vol. 54 pp. 13642-13946

DOI 10.1002/anie.201506439

- *Chirally-modified metal surfaces: energetics of interaction with chiral molecules*

P. Dementyev, M. Peter, S. Adamovsky, S. Schauermann

Phys. Chem. Chem. Phys., (2015) vol. 17 pp. 22726-22735

DOI 10.1039/c5cp03627e

- *Carbon dioxide activation by magnetite*

F. Ivars-Barceló, F. Mirabella, **P. Dementyev**, J. Seifert, S. Schauermann, and H.-J. Freund

in preparation

Conference presentations

- 31st European Conference on Surface Science (ECOSS31)
August 30–September 4, 2015, **Barcelona**, Spain
Surface chemistry of water on magnetite thin films
- 114th General Assembly of the German Bunsen Society for Physical Chemistry (Bunsentagung 2015)
May 14-16, 2015, **Bochum**, Germany
Adsorption of water on magnetite: mechanism and energetics
- DPG Spring Meeting (DPG-Frühjahrstagung 2015)
March 15-20, 2015, **Berlin**, Germany
Adsorption of carbon dioxide onto an iron oxide
- 16th Netherlands' Catalysis and Chemistry Conference
March 2-4, 2015, **Noordwijkerhout**, The Netherlands
Carbon dioxide activation on magnetite: a surface science study
- European Symposium on Surface Science 1st edition
November 26-28, 2014, **Rome**, Italy
Surface chemistry of water on iron oxide: an UHV study
- 30th European Conference on Surface Science (ECOSS30)
August 31 – September 5, 2014, **Antalya**, Turkey
Adsorption Energy of D₂O on Fe₃O₄(111) by Microcalorimetry
- 16th Nordic Symposium on Catalysis
June 15-17, 2014, **Oslo**, Norway
Adsorption Energy of Propylene Oxide Enantiomers on Chirally Modified Platinum Measured with Single-Crystal Adsorption Calorimetry

Acknowledgments

I express my deepest gratitude to Prof. Hans-Joachim Freund and Dr. Svetlana Schauermann for giving me the opportunity to do my doctoral research in so excellent professional environment as the Chemical Physics Department of the Fritz Haber Institute. I especially appreciate the high degree of discretion in studies which was granted to me from the very beginning.

I thank Prof. Reinhard Schomäcker for being my official supervisor and reviewing my thesis and Prof. Arne Thomas for taking the chair of the examination committee.

I'm grateful to Dr. Sergey Adamovsky and Dr. Matthias Peter who introduced me into the UHV methodology. Many thanks to all members of the Molecular Beam Group, especially to Dr. Casey P. O'Brien, Dr. Karl-Heinz Dostert, Dr. Francisco Ivars-Barceló and Francesca Mirabella for assisting in surface spectroscopy experiments. I also appreciate contribution from Stephanie Hemmingson and Dr. Jan Seifert. Additionally, I thank Dr. Evan Spadafora for proofreading my thesis.

Furthermore, I would like to thank the group of Prof. Joachim Sauer at the HU Berlin, particularly Dr. Joachim Paier and Xiaoke Li, for very fruitful collaboration.

I gratefully acknowledge financial support from the Max Planck Society and the International Max Planck Research School "Functional Interfaces in Physics and Chemistry".

Special thanks to my family – my dearest Vova and Polia.

Abbreviations

AES	Auger Electron Spectroscopy
DFT	Density Functional Theory
EAI	Equilibrium Adsorption Isotherms/Isobars
GCA	Glass Capillary Array
HREELS	High Resolution Electron Energy Loss Spectroscopy
IRAS	Infrared Reflection-Absorption Spectroscopy
LEED	Low-Energy Electron Diffraction
LEIS	Low-Energy Ion Scattering
MBA	2-Methylbutanoic Acid
ML	Monolayer
NEA	1-(1-naphthyl)ethylamine
NEXAFS	Near Edge X-ray Absorption Fine Structure
PO	Propylene Oxide
PVD	Physical Vapor Deposition
PVDF	Polyvinylidene Difluoride
QCM	Quartz Crystal Microbalance
QMS	Quadrupole Mass Spectrometer
SCAC	Single-Crystal Adsorption Calorimetry
SCV	Subsurface Cation Vacancies
STM	Scanning Tunneling Microscopy
TPD	Temperature-Programmed Desorption
UHV	Ultrahigh Vacuum
UPS	Ultraviolet Photoelectron Spectroscopy
WGSr	Water-Gas Shift Reaction
XAS	X-ray Absorption Spectroscopy
XPS	X-ray Photoelectron Spectroscopy

References

- [1] Eurostat, <http://ec.europa.eu/eurostat/web/main>, European Comission: (2016).
- [2] Knözinger, H.; Kochloefl, K., *Heterogeneous Catalysis and Solid Catalysts*, Wiley-VCH Verlag GmbH & Co. KGaA: Weinheim, (2005).
- [3] Thomas, J. M., *Chemsuschem*, (2014) **7**, 1801.
- [4] Norskov, J. K.; Bligaard, T.; Hvolbaek, B.; Abild-Pedersen, F.; Chorkendorff, I.; Christensen, C. H., *Chem Soc Rev*, (2008) **37**, 2163.
- [5] Rouquerol, F.; Rouquerol, J.; Sing, K. S. W.; Llewellyn, P.; Maurin, G., *Adsorption by Powders and Porous Solids: Principles, Methodology and Applications*, Academic Press: (2014).
- [6] Wrabetz, S.; Yang, X. B.; Tzolova-Muller, G.; Schlögl, R.; Jentoft, F. C., *J Catal*, (2010) **269**, 351.
- [7] Goodman, D. W., *Chem Rev*, (1995) **95**, 523.
- [8] Freund, H. J., *Catal Today*, (2005) **100**, 3.
- [9] Ertl, G., *Catal Rev*, (1980) **21**, 201.
- [10] Baumer, M.; Freund, H. J., *Prog Surf Sci*, (1999) **61**, 127.
- [11] Campbell, C. T., *Surf Sci Rep*, (1997) **27**, 1.
- [12] Henry, C. R., *Surf Sci Rep*, (1998) **31**, 235.
- [13] Freund, H. J.; Kühlenbeck, H.; Staemmler, V., *Rep Prog Phys*, (1996) **59**, 283.
- [14] Libuda, J.; Schalow, T.; Brandt, B.; Laurin, M.; Schauermaann, S., *Microchimica Acta*, (2007) **156**, 9.
- [15] Libuda, J.; Freund, H. J., *Surf Sci Rep*, (2005) **57**, 157.
- [16] Weiss, W.; Ranke, W., *Prog Surf Sci*, (2002) **70**, 1.
- [17] Cerny, S., *Surf Sci Rep*, (1996) **26**, 3.
- [18] Roberts, J. K., *Proc R Soc Lon Ser-A*, (1935) **152**, 445.
- [19] Couper, A.; John, C. S., *J Chem Soc Farad T 1*, (1977) **73**, 950.
- [20] Beeck, O., *Rev Mod Phys*, (1945) **17**, 61.
- [21] Beeck, O.; Cole, W. A.; Wheeler, A., *Discuss Faraday Soc*, (1950), 314.
- [22] Wedler, G., *Zeitschrift für Physikalische Chemie*, (1960) **24**, 73.
- [23] Borroni-Bird, C. E.; Alsarraf, N.; Andersson, S.; King, D. A., *Chem Phys Lett*, (1991) **183**, 516.
- [24] Borroni-Bird, C. E.; King, D. A., *Rev Sci Instrum*, (1991) **62**, 2177.
- [25] Brown, W. A.; Kose, R.; King, D. A., *Chem Rev*, (1998) **98**, 797.
- [26] Stuckless, J. T.; Frei, N. A.; Campbell, C. T., *Rev Sci Instrum*, (1998) **69**, 2427.
- [27] Ajo, H. M.; Ihm, H.; Moilanen, D. E.; Campbell, C. T., *Rev Sci Instrum*, (2004) **75**, 4471.
- [28] Lew, W.; Lytken, O.; Farmer, J. A.; Crowe, M. C.; Campbell, C. T., *Rev Sci Instrum*, (2010) **81**,
- [29] Crowe, M. C.; Campbell, C. T., *Annu Rev Anal Chem*, (2011) **4**, 41.
- [30] Fischer-Wolfarth, J. H.; Hartmann, J.; Farmer, J. A.; Flores-Camacho, J. M.; Campbell, C. T.; Schauermaann, S.; Freund, H. J., *Rev Sci Instrum*, (2011) **82**,
- [31] Hartz, P.; Schafer, R., *Rev Sci Instrum*, (2014) **85**,
- [32] Etzel, K. D.; Bickel, K. R.; Schuster, R., *Rev Sci Instrum*, (2010) **81**,
- [33] Ge, Q. F.; Kose, R.; King, D. A., *Adv Catal*, (2000) **45**, 207.

- [34] Liao, K.; Fiorin, V.; Jenkins, S. J.; King, D. A., *Phys Chem Chem Phys*, (2012) **14**, 7528.
- [35] Liao, K.; Fiorin, V.; Gunn, D. S. D.; Jenkins, S. J.; King, D. A., *Phys Chem Chem Phys*, (2013) **15**, 4059.
- [36] Schauermann, S.; Silbaugh, T. L.; Campbell, C. T., *Chem Rec*, (2014) **14**, 759.
- [37] Fischer-Wolfarth, J. H.; Farmer, J. A.; Flores-Camacho, J. M.; Genest, A.; Yudanov, I. V.; Rosch, N.; Campbell, C. T.; Schauermann, S.; Freund, H. J., *Phys Rev B*, (2010) **81**,
- [38] Peter, M.; Adamovsky, S.; Camacho, J. M. F.; Schauermann, S., *Faraday Discuss*, (2013) **162**, 341.
- [39] Peter, M.; Camacho, J. M. F.; Adamovski, S.; Ono, L. K.; Dostert, K. H.; O'Brien, C. P.; Cuenya, B. R.; Schauermann, S.; Freund, H. J., *Angew Chem Int Edit*, (2013) **52**, 5175.
- [40] Heitbaum, M.; Glorius, F.; Escher, I., *Angew Chem Int Edit*, (2006) **45**, 4732.
- [41] Mallat, T.; Orglmeister, E.; Baiker, A., *Chem Rev*, (2007) **107**, 4863.
- [42] Gellman, A. J.; Tysoe, W. T.; Zaera, F., *Catal Lett*, (2015) **145**, 220.
- [43] Lee, I.; Zaera, F., *J Am Chem Soc*, (2006) **128**, 8890.
- [44] Lee, I.; Ma, Z.; Kaneko, S.; Zaera, F., *J Am Chem Soc*, (2008) **130**, 14597.
- [45] Jackson, S. D.; Hargreaves, J. S. J. Eds., *Metal Oxide Catalysis*, WILEY-VCH Verlag GmbH & Co. KGaA: Weinheim, (2009); Vol. 2.
- [46] Lee, D. W.; Lee, M. S.; Lee, J. Y.; Kim, S.; Eom, H. J.; Moon, D. J.; Lee, K. Y., *Catal Today*, (2013) **210**, 2.
- [47] Ratnasamy, C.; Wagner, J. P., *Catal Rev*, (2009) **51**, 325.
- [48] Leist, U.; Ranke, W.; Al-Shamery, K., *Phys Chem Chem Phys*, (2003) **5**, 2435.
- [49] Joseph, Y.; Ranke, W.; Weiss, W., *J Phys Chem B*, (2000) **104**, 3224.
- [50] Kendelewicz, T.; Liu, P.; Doyle, C. S.; Brown, G. E.; Nelson, E. J.; Chambers, S. A., *Surf Sci*, (2000) **453**, 32.
- [51] Kendelewicz, T.; Kaya, S.; Newberg, J. T.; Bluhm, H.; Mulakaluri, N.; Moritz, W.; Scheffler, M.; Nilsson, A.; Pentcheva, R.; Brown, G. E., *J Phys Chem C*, (2013) **117**, 2719.
- [52] Meemken, F.; Maeda, N.; Hungerbuhler, K.; Baiker, A., *Angew Chem Int Edit*, (2012) **51**, 8212.
- [53] Meemken, F.; Hungerbuhler, K.; Baiker, A., *Angew Chem Int Edit*, (2014) **53**, 8640.
- [54] Meemken, F.; Baiker, A.; Schenker, S.; Hungerbuhler, K., *Chem-Eur J*, (2014) **20**, 1298.
- [55] Tan, S.; Williams, C. T., *J Phys Chem C*, (2013) **117**, 18043.
- [56] Trant, A. G.; Baddeley, C. J., *J Phys Chem C*, (2011) **115**, 1025.
- [57] Baddeley, C. J.; Jones, T. E.; Trant, A. G.; Wilson, K. E., *Top Catal*, (2011) **54**, 1348.
- [58] Ernst, K. H., *Surf Sci*, (2013) **613**, 1.
- [59] McFadden, C. F.; Cremer, P. S.; Gellman, A. J., *Langmuir*, (1996) **12**, 2483.
- [60] Gellman, A. J.; Horvath, J. D.; Buelow, M. T., *J Mol Catal a-Chem*, (2001) **167**, 3.

- [61] Horvath, J. D.; Gellman, A. J., *J Am Chem Soc*, (2001) **123**, 7953.
- [62] Horvath, J. D.; Gellman, A. J., *J Am Chem Soc*, (2002) **124**, 2384.
- [63] Yun, Y. J.; Gellman, A. J., *Angew Chem Int Edit*, (2013) **52**, 3394.
- [64] Huang, Y.; Gellman, A. J., *Top Catal*, (2011) **54**, 1403.
- [65] Cheong, W. Y.; Gellman, A. J., *J Phys Chem C*, (2011) **115**, 1031.
- [66] Cheong, W. Y.; Huang, Y.; Dangaria, N.; Gellman, A. J., *Langmuir*, (2010) **26**, 16412.
- [67] Cheong, W. Y.; Gellman, A. J., *Langmuir*, (2012) **28**, 15251.
- [68] Lawton, T. J.; Pushkarev, V.; Wei, D.; Lucci, F. R.; Sholl, D. S.; Gellman, A. J.; Sykes, E. C. H., *J Phys Chem C*, (2013) **117**, 22290.
- [69] Bonello, J. M.; Lambert, R. M.; Kunzle, N.; Baiker, A., *J Am Chem Soc*, (2000) **122**, 9864.
- [70] Castonguay, M.; Roy, J. R.; Rochefort, A.; McBreen, P. H., *J Am Chem Soc*, (2000) **122**, 518.
- [71] Wilson, K. E.; Trant, A. G.; Baddeley, C. J., *J Phys Chem C*, (2012) **116**, 1092.
- [72] Seljamae-Green, R. T.; Simpson, G. J.; Grillo, F.; Greenwood, J.; Francis, S. M.; Schaub, R.; Lacovig, P.; Baddeley, C. J., *Langmuir*, (2014) **30**, 3495.
- [73] Burkholder, L.; Tysoe, W. T., *J Phys Chem C*, (2009) **113**, 15298.
- [74] Hong, J. H.; Lee, I.; Zaera, F., *Top Catal*, (2011) **54**, 1340.
- [75] Demers-Carpentier, V.; Goubert, G.; Masini, F.; Lafleur-Lambert, R.; Dong, Y.; Lavoie, S.; Mahieu, G.; Boukouvalas, J.; Gao, H. L.; Rasmussen, A. M. H.; Ferrighi, L.; Pan, Y. X.; Hammer, B.; McBreen, P. H., *Science*, (2011) **334**, 776.
- [76] Stacchiola, D.; Burkholder, L.; Tysoe, W. T., *J Am Chem Soc*, (2002) **124**, 8984.
- [77] Stacchiola, D.; Burkholder, L.; Zheng, T.; Weinert, M.; Tysoe, W. T., *J Phys Chem B*, (2005) **109**, 851.
- [78] Gao, F.; Wang, Y. L.; Burkholder, L.; Tysoe, W. T., *J Am Chem Soc*, (2007) **129**, 15240.
- [79] Gao, F.; Wang, Y. L.; Burkholder, L.; Hirschmugl, C.; Saldin, D. K.; Poon, H. C.; Sholl, D.; James, J.; Tysoe, W. T., *Surf Sci*, (2008) **602**, 2264.
- [80] Gao, F.; Wang, Y. L.; Tysoe, W. T., *J Phys Chem C*, (2008) **112**, 6145.
- [81] Burkholder, L.; Stacchiola, D.; Boscoboinik, J. A.; Tysoe, W. T., *J Phys Chem C*, (2009) **113**, 13877.
- [82] Lee, I.; Zaera, F., *J Phys Chem B*, (2005) **109**, 12920.
- [83] Mahapatra, M.; Burkholder, L.; Bai, Y.; Garvey, M.; Boscoboinik, J. A.; Hirschmugl, C.; Tysoe, W. T., *J Phys Chem C*, (2014) **118**, 6856.
- [84] Mahapatra, M.; Tysoe, W. T., *Surf Sci*, (2014) **629**, 132.
- [85] Dinger, A.; Lutterloh, C.; Biener, J.; Kuppers, J., *Surf Sci*, (2000) **449**, 1.
- [86] Minder, B.; Schurch, M.; Mallat, T.; Baiker, A.; Heinz, T.; Pfaltz, A., *J Catal*, (1996) **160**, 261.
- [87] Bonello, J. M.; Sykes, E. C. H.; Lindsay, R.; Williams, F. J.; Santra, A. K.; Lambert, R. M., *Surf Sci*, (2001) **482**, 207.
- [88] Bonello, J. M.; Williams, F. J.; Lambert, R. M., *J Am Chem Soc*, (2003) **125**, 2723.

- [89] Lavoie, S.; Laliberte, M. A.; McBreen, P. H., *J Am Chem Soc*, (2003) **125**, 15756.
- [90] Lavoie, S.; Laliberte, M. A.; McBreen, P., *Catal Lett*, (2004) **97**, 111.
- [91] Demers-Carpentier, V.; Goubert, G.; Masini, F.; Dong, Y.; Rasmussen, A. M. H.; Hammer, B.; McBreen, P. H., *J Phys Chem Lett*, (2012) **3**, 92.
- [92] Demers-Carpentier, V.; Rasmussen, A. M. H.; Goubert, G.; Ferrighi, L.; Dong, Y.; Lemay, J. C.; Masini, F.; Zeng, Y.; Hammer, B.; McBreen, P. H., *J Am Chem Soc*, (2013) **135**, 9999.
- [93] Goubert, G.; McBreen, P. H., *Acs Catal*, (2014) **4**, 847.
- [94] Svane, K.; Dong, Y.; Groves, M. N.; Demers-Carpentier, V.; Lemay, J. C.; Ouellet, M.; Hammer, B.; McBreen, P. H., *Catal Sci Technol*, (2015) **5**, 743.
- [95] Sales, J. L.; Gargiulo, V.; Lee, I.; Zaera, F.; Zgrablich, G., *Catal Today*, (2010) **158**, 186.
- [96] Boscoboinik, J. A.; Bai, Y.; Burkholder, L.; Tysoe, W. T., *J Phys Chem C*, (2011) **115**, 16488.
- [97] Burkholder, L.; Garvey, M.; Weinert, M.; Tysoe, W. T., *J Phys Chem C*, (2011) **115**, 8790.
- [98] Woodruff, D. P., *Chem Rev*, (2013) **113**, 3863.
- [99] Pang, C. L.; Lindsay, R.; Thornton, G., *Chem Rev*, (2013) **113**, 3887.
- [100] Diebold, U., *Surf Sci Rep*, (2003) **48**, 53.
- [101] Chambers, S. A., *Surf Sci Rep*, (2000) **39**, 105.
- [102] Jaeger, R. M.; Kuhlenbeck, H.; Freund, H. J.; Wuttig, M.; Hoffmann, W.; Franchy, R.; Ibach, H., *Surf Sci*, (1991) **259**, 235.
- [103] Kresse, G.; Schmid, M.; Napetschnig, E.; Shishkin, M.; Kohler, L.; Varga, P., *Science*, (2005) **308**, 1440.
- [104] Benedetti, S.; Benia, H. M.; Nilius, N.; Valeri, S.; Freund, H. J., *Chem Phys Lett*, (2006) **430**, 330.
- [105] Liu, B. H.; Boscoboinik, J. A.; Cui, Y.; Shaikhutdinov, S.; Freund, H. J., *J Phys Chem C*, (2015) **119**, 7842.
- [106] Huggins, C. P.; Nix, R. M., *Surf Sci*, (2005) **594**, 163.
- [107] Mullins, D. R.; Radulovic, P. V.; Overbury, S. H., *Surf Sci*, (1999) **429**, 186.
- [108] Kuhlenbeck, H.; Shaikhutdinov, S.; Freund, H. J., *Chem Rev*, (2013) **113**, 3986.
- [109] Ketteler, G.; Weiss, W.; Ranke, W.; Schlogl, R., *Phys Chem Chem Phys*, (2001) **3**, 1114.
- [110] Senn, M. S.; Wright, J. P.; Attfield, J. P., *Nature*, (2012) **481**, 173.
- [111] Seoighe, C.; Naumann, J.; Shvets, I. V., *Surf Sci*, (1999) **440**, 116.
- [112] Shimizu, T. K.; Jung, J.; Kato, H. S.; Kim, Y.; Kawai, M., *Phys Rev B*, (2010) **81**,
- [113] Ritter, M.; Weiss, W., *Surf Sci*, (1999) **432**, 81.
- [114] Lennie, A. R.; Condon, N. G.; Leibsle, F. M.; Murray, P. W.; Thornton, G.; Vaughan, D. J., *Phys Rev B*, (1996) **53**, 10244.
- [115] Condon, N. G.; Leibsle, F. M.; Parker, T.; Lennie, A. R.; Vaughan, D. J.; Thornton, G., *Phys Rev B*, (1997) **55**, 15885.
- [116] Berdunov, N.; Murphy, S.; Mariotto, G.; Shvets, I. V., *Phys Rev B*, (2004) **70**,

- [117] Cutting, R. S.; Muryn, C. A.; Thornton, G.; Vaughan, D. J., *Geochim Cosmochim Acta*, (2006) **70**, 3593.
- [118] Paul, M.; Sing, M.; Claessen, R.; Schrupp, D.; Brabers, V. A. M., *Phys Rev B*, (2007) **76**,
- [119] Shaikhutdinov, S. K.; Ritter, M.; Wang, X. G.; Over, H.; Weiss, W., *Phys Rev B*, (1999) **60**, 11062.
- [120] Lemire, C.; Meyer, R.; Henrich, V. E.; Shaikhutdinov, S.; Freund, H. J., *Surf Sci*, (2004) **572**, 103.
- [121] Sala, A.; Marchetto, H.; Qin, Z. H.; Shaikhutdinov, S.; Schmidt, T.; Freund, H. J., *Phys Rev B*, (2012) **86**,
- [122] Kaya, S.; Ogasawara, H.; Nilsson, A., *Catal Today*, (2015) **240**, 184.
- [123] Tarrach, G.; Burgler, D.; Schaub, T.; Wiesendanger, R.; Guntherodt, H. J., *Surf Sci*, (1993) **285**, 1.
- [124] Ceballos, S. F.; Mariotto, G.; Jordan, K.; Murphy, S.; Seoighe, C.; Shvets, I. V., *Surf Sci*, (2004) **548**, 106.
- [125] Chambers, S. A.; Thevuthasan, S.; Joyce, S. A., *Surf Sci*, (2000) **450**, L273.
- [126] Stanka, B.; Hebenstreit, W.; Diebold, U.; Chambers, S. A., *Surf Sci*, (2000) **448**, 49.
- [127] Pentcheva, R.; Wendler, F.; Meyerheim, H. L.; Moritz, W.; Jedrecy, N.; Scheffler, M., *Phys Rev Lett*, (2005) **94**,
- [128] Lodziana, Z., *Phys Rev Lett*, (2007) **99**,
- [129] Parkinson, G. S.; Novotny, Z.; Jacobson, P.; Schmid, M.; Diebold, U., *Surf Sci*, (2011) **605**, L42.
- [130] Yu, X. H.; Huo, C. F.; Li, Y. W.; Wang, J. G.; Jiao, H. J., *Surf Sci*, (2012) **606**, 872.
- [131] Bliem, R.; McDermott, E.; Ferstl, P.; Setvin, M.; Gamba, O.; Pavelec, J.; Schneider, M. A.; Schmid, M.; Diebold, U.; Blaha, P.; Hammer, L.; Parkinson, G. S., *Science*, (2014) **346**, 1215.
- [132] Parkinson, G. S.; Novotny, Z.; Argentero, G.; Schmid, M.; Pavelec, J.; Kosak, R.; Blaha, P.; Diebold, U., *Nat Mater*, (2013) **12**, 724.
- [133] Bliem, R.; Kosak, R.; Perneczky, L.; Novotny, Z.; Gamba, O.; Fobes, D.; Mao, Z. Q.; Schmid, M.; Blaha, P.; Diebold, U.; Parkinson, G. S., *Acs Nano*, (2014) **8**, 7531.
- [134] Kim, Y. J.; Gao, Y.; Chambers, S. A., *Surf Sci*, (1997) **371**, 358.
- [135] Gao, Y.; Chambers, S. A., *J Cryst Growth*, (1997) **174**, 446.
- [136] Spiridis, N.; Handke, B.; Slezak, T.; Barbasz, J.; Zajac, M.; Haber, J.; Korecki, J., *J Phys Chem B*, (2004) **108**, 14356.
- [137] Korecki, J.; Handke, B.; Spiridis, N.; Slezak, T.; Flis-Kabulska, I.; Haber, J., *Thin Solid Films*, (2002) **412**, 14.
- [138] Spiridis, N.; Barbasz, J.; Lodziana, Z.; Korecki, J., *Phys Rev B*, (2006) **74**,
- [139] Liu, S. M.; Wang, S.; Li, W. T.; Guo, J. D.; Guo, Q. L., *J Phys Chem C*, (2013) **117**, 14070.
- [140] Davis, E. M.; Zhang, K.; Cui, Y.; Kuhlenbeck, H.; Shaikhutdinov, S.; Freund, H. J., *Surf Sci*, (2015) **636**, 42.
- [141] Cutting, R. S.; Muryn, C. A.; Vaughan, D. J.; Thornton, G., *Surf Sci*, (2008) **602**, 1155.
- [142] Joseph, Y.; Kuhrs, C.; Ranke, W.; Weiss, W., *Surf Sci*, (1999) **433**, 114.

- [143] Joseph, Y.; Kuhrs, C.; Ranke, W.; Ritter, M.; Weiss, W., *Chem Phys Lett*, (1999) **314**, 195.
- [144] Herman, G. S.; McDaniel, E. P.; Joyce, S. A., *J Electron Spectrosc*, (1999) **101**, 433.
- [145] Adib, K.; Totir, G. G.; Fitts, J. P.; Rim, K. T.; Mueller, T.; Flynn, G. W.; Joyce, S. A.; Osgood, R. M., *Surf Sci*, (2003) **537**, 191.
- [146] Rim, K. T.; Eom, D.; Chan, S. W.; Flytzani-Stephanopoulos, M.; Flynn, G. W.; Wen, X. D.; Batista, E. R., *J Am Chem Soc*, (2012) **134**, 18979.
- [147] Peden, C. H. F.; Herman, G. S.; Ismagilov, I. Z.; Kay, B. D.; Henderson, M. A.; Kim, Y. J.; Chambers, S. A., *Catal Today*, (1999) **51**, 513.
- [148] Parkinson, G. S.; Novotny, Z.; Jacobson, P.; Schmid, M.; Diebold, U., *J Am Chem Soc*, (2011) **133**, 12650.
- [149] Flores-Camacho, J. M.; Fischer-Wolfarth, J. H.; Peter, M.; Campbell, C. T.; Schauermann, S.; Freund, H. J., *Phys Chem Chem Phys*, (2011) **13**, 16800.
- [150] Greenler, R. G.; Snider, D. R.; Witt, D.; Sorbello, R. S., *Surf Sci*, (1982) **118**, 415.
- [151] Libuda, J.; Meusel, I.; Hartmann, J.; Freund, H. J., *Rev Sci Instrum*, (2000) **71**, 4395.
- [152] Gordon, A. D.; Zaera, F., *Angew Chem Int Edit*, (2013) **52**, 3453.
- [153] Dementyev, P.; Peter, M.; Adamovsky, S.; Schauermann, S., *Phys Chem Chem Phys*, (2015) **17**, 22726.
- [154] Fisher, G. B.; Gland, J. L., *Surf Sci*, (1980) **94**, 446.
- [155] Ogasawara, H.; Yoshinobu, J.; Kawai, M., *Chem Phys Lett*, (1994) **231**, 188.
- [156] Blaser, H. U.; Studer, M., *Accounts Chem Res*, (2007) **40**, 1348.
- [157] Pachon, L. D.; Yosef, I.; Markus, T. Z.; Naaman, R.; Avnir, D.; Rothenberg, G., *Nat Chem*, (2009) **1**, 160.
- [158] Holland, M. C.; Meemken, F.; Baiker, A.; Gilmour, R., *J Mol Catal a-Chem*, (2015) **396**, 335.
- [159] Kyriakou, G.; Beaumont, S. K.; Lambert, R. M., *Langmuir*, (2011) **27**, 9687.
- [160] Meemken, F.; Baiker, A.; Dupre, J.; Hungerbuhler, K., *Acs Catal*, (2014) **4**, 344.
- [161] Zaera, F., *J Phys Chem C*, (2008) **112**, 16196.
- [162] Ernst, K. H., *Phys Status Solidi B*, (2012) **249**, 2057.
- [163] Raval, R., *J Phys-Condens Mat*, (2002) **14**, 4119.
- [164] Beaumont, S. K.; Kyriakou, G.; Watson, D. J.; Vaughan, O. P. H.; Papageorgiou, A. C.; Lambert, R. M., *J Phys Chem C*, (2010) **114**, 15075.
- [165] Baldanza, S.; Cornish, A.; Nicklin, R. E. J.; Zheleva, Z. V.; Held, G., *Surf Sci*, (2014) **629**, 114.
- [166] Garvey, M.; Bai, Y.; Boscoboinik, J. A.; Burkholder, L.; Sorensen, T. E.; Tysoe, W. T., *J Phys Chem C*, (2013) **117**, 4505.
- [167] Greenwood, J.; Fruchtl, H. A.; Baddeley, C. J., *J Phys Chem C*, (2013) **117**, 22874.
- [168] Goubert, G.; Groves, M. N.; Dong, Y.; Lemay, J.-C.; McBreen, P. H.; Hammer, B., *J Phys Chem C*, (2015),
- [169] Karakalos, S.; Lawton, T. J.; Lucci, F. R.; Sykes, E. C. H.; Zaera, F., *J Phys Chem C*, (2013) **117**, 18588.

- [170] Stacchiola, D.; Burkholder, L.; Tysoe, W. T., *J Mol Catal a-Chem*, (2004) **216**, 215.
- [171] Karp, E. M.; Silbaugh, T. L.; Campbell, C. T., *J Phys Chem C*, (2013) **117**, 6325.
- [172] Henderson, M. A., *Surf Sci Rep*, (2002) **46**, 1.
- [173] Chao, J.; Hall, K. R.; Marsh, K. N.; Wilhoit, R. C., *J Phys Chem Ref Data*, (1986) **15**, 1369.
- [174] Yeo, Y. Y.; Vattuone, L.; King, D. A., *J Chem Phys*, (1997) **106**, 392.
- [175] Cornell, R. M.; Schwertmann, U. Eds., *The Iron Oxides: Structure, Properties, Reactions, Occurences and Uses*, Wiley-VCH: Weinheim, (2004); Vol.
- [176] Brookes, I. M.; Muryn, C. A.; Thornton, G., *Phys Rev Lett*, (2001) **87**,
- [177] Di Valentin, C.; Tilocca, A.; Selloni, A.; Beck, T. J.; Klust, A.; Batzill, M.; Losovyj, Y.; Diebold, U., *J Am Chem Soc*, (2005) **127**, 9895.
- [178] Kimmel, G. A.; Baer, M.; Petrik, N. G.; VandeVondele, J.; Rousseau, R.; Mundy, C. J., *J. Phys. Chem. Lett.*, (2012) **3**, 778.
- [179] Meyer, B.; Marx, D.; Dulub, O.; Diebold, U.; Kunat, M.; Langenberg, D.; Woll, C., *Angew Chem Int Edit*, (2004) **43**, 6642.
- [180] Noei, H.; Qiu, H. S.; Wang, Y. M.; Loffler, E.; Woll, C.; Muhler, M., *Phys Chem Chem Phys*, (2008) **10**, 7092.
- [181] Yamamoto, S.; Kendelewicz, T.; Newberg, J. T.; Ketteler, G.; Starr, D. E.; Mysak, E. R.; Andersson, K. J.; Ogasawara, H.; Bluhm, H.; Salmeron, M.; Brown, G. E.; Nilsson, A., *J Phys Chem C*, (2010) **114**, 2256.
- [182] Mu, R. T.; Cantu, D. C.; Lin, X.; Glezakou, V. A.; Wang, Z. T.; Lyubinetsky, I.; Rousseau, R.; Dohnalek, Z., *J Phys Chem Lett*, (2014) **5**, 3445.
- [183] Henderson, M. A., *Surf Sci*, (1996) **355**, 151.
- [184] Ahdjoudj, J.; Martinsky, C.; Minot, C.; Van Hove, M. A.; Somorjai, G. A., *Surf Sci*, (1999) **443**, 133.
- [185] Grillo, M. E.; Finnis, M. W.; Ranke, W., *Phys Rev B*, (2008) **77**,
- [186] Zhou, C. G.; Zhang, Q. F.; Chen, L.; Han, B.; Ni, G.; Wu, J. P.; Garg, D.; Cheng, H. S., *J Phys Chem C*, (2010) **114**, 21405.
- [187] King, D. A.; Wells, M. G., *Proc R Soc Lon Ser-A*, (1974) **339**, 245.
- [188] Kiejna, A.; Ossowski, T.; Pabisiak, T., *Phys Rev B*, (2012) **85**,
- [189] Cornell, R. M.; Schwertmann, U., Introduction to the Iron Oxides, In *The Iron Oxides*, Wiley-VCH Verlag GmbH & Co. KGaA: (2004); pp 1.
- [190] Brookes, I. M.; Muryn, C. A.; Thornton, G., *Phys. Rev. Lett.*, (2001) **87**, 266103.
- [191] Meyer, B.; Marx, D.; Dulub, O.; Diebold, U.; Kunat, M.; Langenberg, D.; Wöll, C., *Angew. Chem. Int. Ed.*, (2004) **43**, 6641.
- [192] Noei, H.; Qiu, H.; Wang, Y.; Loffler, E.; Woll, C.; Muhler, M., *Phys. Chem. Chem. Phys.*, (2008) **10**, 7092.
- [193] Mu, R.; Cantu, D. C.; Lin, X.; Glezakou, V.-A.; Wang, Z.; Lyubinetsky, I.; Rousseau, R.; Dohnalek, Z., *J. Phys. Chem. Lett.*, (2014) **5**, 3445.
- [194] Dementyev, P.; Dostert, K.-H.; Ivars-Barceló, F.; O'Brien, C. P.; Mirabella, F.; Schauermaann, S.; Li, X.; Paier, J.; Sauer, J.; H.-J., F., *Angewandte Chemie International Edition*, (2015) **54**, 13942
- [195] Ajo, H. M.; Ihm, H.; Moilanen, D. E.; Campbell, C. T., *Rev. Sci. Instrum.*, (2004) **75**, 4471.

- [196] Fischer-Wolfarth, J.-H.; Hartmann, J.; Farmer, J. A.; Flores-Camacho, J. M.; Campbell, C. T.; Schauermann, S.; Freund, H.-J., *Rev. Sci. Instrum.*, (2011) **82**, 024102.
- [197] Lew, W. D.; Crowe, M. C.; Karp, E.; Campbell, C. T., *J Phys Chem C*, (2011) **115**, 9164.
- [198] Schalow, T.; Brandt, B.; Starr, D.; Laurin, M.; Schauermann, S.; Shaikhutdinov, S.; Libuda, J.; Freund, H. J., *Catalysis Letters*, (2006) **107**, 189.
- [199] Urbanova, V.; Magro, M.; Gedanken, A.; Baratella, D.; Vianello, F.; Zboril, R., *Chem Mater*, (2014) **26**, 6653.
- [200] Gawande, M. B.; Branco, P. S.; Varma, R. S., *Chem Soc Rev*, (2013) **42**, 3371.
- [201] Moussy, J. B., *J Phys D Appl Phys*, (2013) **46**,
- [202] Li, Z. S.; Potapenko, D. V.; Rim, K. T.; Flytzani-Stephanopoulos, M.; Flynn, G. W.; Osgood, R. M.; Wen, X. D.; Batista, E. R., *J Phys Chem C*, (2015) **119**, 1113.
- [203] Gamba, O.; Noei, H.; Pavelec, J.; Bliem, R.; Schmid, M.; Diebold, U.; Stierle, A.; Parkinson, G. S., *J Phys Chem C*, (2015) **119**, 20459.
- [204] Kuhrs, C.; Arita, Y.; Weiss, W.; Ranke, W.; Schlogl, R., *Top Catal*, (2001) **14**, 111.
- [205] Mendes, D.; Mendes, A.; Madeira, L. M.; Iulianelli, A.; Sousa, J. M.; Basile, A., *Asia-Pac J Chem Eng*, (2010) **5**, 111.
- [206] Rhodes, C.; Hutchings, G. J.; Ward, A. M., *Catal Today*, (1995) **23**, 43.
- [207] Brown, D. E.; George, S. M.; Huang, C.; Wong, E. K. L.; Rider, K. B.; Smith, R. S.; Kay, B. D., *J Phys Chem-U.S.*, (1996) **100**, 4988.
- [208] Santos-Carballal, D.; Roldan, A.; Grau-Crespo, R.; de Leeuw, N. H., *Phys Chem Chem Phys*, (2014) **16**, 21082.
- [209] Hunter, E. P. L.; Lias, S. G., *J Phys Chem Ref Data*, (1998) **27**, 413.
- [210] Rodriguez, J. A.; Hrbek, J., *Surf Sci*, (2010) **604**, 241.
- [211] Wang, W.; Zhang, H.; Wang, W. H.; Zhao, A. D.; Wang, B.; Hou, J. G., *Chem Phys Lett*, (2010) **500**, 76.
- [212] Xu, L. S.; Wu, Z. F.; Zhang, W. H.; Jin, Y. K.; Yuan, Q.; Ma, Y. S.; Huang, W. X., *J Phys Chem C*, (2012) **116**, 22921.
- [213] Xu, L. S.; Wu, Z. F.; Jin, Y. K.; Ma, Y. S.; Huang, W. X., *Phys Chem Chem Phys*, (2013) **15**, 12068.
- [214] Jin, Y. K.; Sun, G. H.; Xiong, F.; Ding, L. B.; Huang, W. X., *Chem-Eur J*, (2015) **21**, 4252.
- [215] Freund, H. J.; Roberts, M. W., *Surf Sci Rep*, (1996) **25**, 225.
- [216] Burghaus, U., *Prog Surf Sci*, (2014) **89**, 161.